

1995

Surface and sub-surface ablation cell design for remote (robotic) radioactive soil analysis using Laser Ablation-Inductively Coupled-Atomic Emission Spectrometry/Mass Spectrometry LA-ICP-AES/MS

Reza Bashirzadeh
Iowa State University

Follow this and additional works at: <https://lib.dr.iastate.edu/rtd>

 Part of the [Civil Engineering Commons](#), [Environmental Sciences Commons](#), and the [Mechanical Engineering Commons](#)

Recommended Citation

Bashirzadeh, Reza, "Surface and sub-surface ablation cell design for remote (robotic) radioactive soil analysis using Laser Ablation-Inductively Coupled-Atomic Emission Spectrometry/Mass Spectrometry LA-ICP-AES/MS " (1995). *Retrospective Theses and Dissertations*. 11038.

<https://lib.dr.iastate.edu/rtd/11038>

This Dissertation is brought to you for free and open access by the Iowa State University Capstones, Theses and Dissertations at Iowa State University Digital Repository. It has been accepted for inclusion in Retrospective Theses and Dissertations by an authorized administrator of Iowa State University Digital Repository. For more information, please contact digirep@iastate.edu.

INFORMATION TO USERS

This manuscript has been reproduced from the microfilm master. UMI films the text directly from the original or copy submitted. Thus, some thesis and dissertation copies are in typewriter face, while others may be from any type of computer printer.

The quality of this reproduction is dependent upon the quality of the copy submitted. Broken or indistinct print, colored or poor quality illustrations and photographs, print bleedthrough, substandard margins, and improper alignment can adversely affect reproduction.

In the unlikely event that the author did not send UMI a complete manuscript and there are missing pages, these will be noted. Also, if unauthorized copyright material had to be removed, a note will indicate the deletion.

Oversize materials (e.g., maps, drawings, charts) are reproduced by sectioning the original, beginning at the upper left-hand corner and continuing from left to right in equal sections with small overlaps. Each original is also photographed in one exposure and is included in reduced form at the back of the book.

Photographs included in the original manuscript have been reproduced xerographically in this copy. Higher quality 6" x 9" black and white photographic prints are available for any photographs or illustrations appearing in this copy for an additional charge. Contact UMI directly to order.

UMI

A Bell & Howell Information Company
300 North Zeeb Road, Ann Arbor, MI 48106-1346 USA
313/761-4700 800/521-0600

**Surface and sub-surface ablation cell design for remote (robotic)
radioactive soil analysis using Laser Ablation-Inductively Coupled-Atomic
Emission Spectrometry/Mass Spectrometry LA-ICP-AES/MS**

by

Reza Bashirzadeh

A Dissertation Submitted to the
Graduate Faculty in Partial Fulfillment of the
Requirements for the Degree of
DOCTOR OF PHILOSOPHY

Department: Mechanical Engineering
Major: Mechanical Engineering

Approved:

Signature was redacted for privacy.

Signature was redacted for privacy.

In Charge of Major Work

Signature was redacted for privacy.

For the Major Department

Signature was redacted for privacy.

For the Graduate College

Iowa State University
Ames, Iowa
1995

UMI Number: 9610939

UMI Microform 9610939

Copyright 1996, by UMI Company. All rights reserved.

**This microform edition is protected against unauthorized
copying under Title 17, United States Code.**

UMI

**300 North Zeeb Road
Ann Arbor, MI 48103**

TABLE OF CONTENTS

ACKNOWLEDGMENTS	x
CHAPTER 1. INTRODUCTION	1
CHAPTER 2. BACKGROUND	4
2.1 System and Components Description	4
2.1.1 Laser Ablation	4
2.1.2 Inductively Coupled Plasma	6
2.1.3 Atomic Emission Spectrometry	7
2.1.4 Mass Spectrometry	8
2.2 System Performance and Reliability	9
2.2.1 Laser	9
2.2.1.1 Laser Power Density	10
2.2.1.2 Laser Wavelength	10
2.2.1.3 Laser Pulse Duration	11
2.2.1.4 Laser Frequency	11
2.2.2 Ablation Cell	12
2.2.2.1 Cell Volume	12
2.2.2.2 Gas Flow Rate	12
2.2.2.3 Flow-Particle Interaction	12
2.2.3 Soil Sample	13
2.2.4 Inductively Coupled Plasma (ICP)	13
2.2.4.1 Amount of Ablated Materials	13
2.2.4.2 Gas Flow Rate	13

2.2.4.3 Radio Frequency (RF) Power	14
2.2.4.4 Observation Height	14
CHAPTER 3. OBJECTIVE	16
CHAPTER 4. LITERATURE REVIEW	18
4.1 Ablation Cell	18
4.2 Transfer Line	26
CHAPTER 5. THEORY AND MODELING	29
5.1 Theory	29
5.1.1 Forces Acting on the Particles	29
5.1.1.1 External (Body) Forces	29
5.1.1.2 Resistance of Medium (Drag Force)	31
5.1.1.3 Interaction Forces	32
5.1.2 Aerosol Dynamic	34
5.1.2.1 Particle Size Regions	34
5.1.2.2 Resistance of Medium in Different Regions	35
5.1.2.3 Non-Uniform Rectilinear Motion of Aerosol Particles	38
5.2 Mathematical Modeling	41
5.2.1 Assumptions	41
5.2.1.1 Ablated Particles	41
5.2.1.2 Gas Flow	42
5.2.2 Surface Ablation Cell	43
5.2.3 Transfer Line	47
CHAPTER 6. CELL DESIGN	51
6.1 Surface Ablation Cell	52
6.1.1 Design Criteria	53
6.1.2 Flow Pattern Study Inside the Cell Using Plexiglas Models	53
6.1.3 Optimum Cell Selection	61
6.1.4 Final Cell Design	62
6.1.5 Force Analysis	65
6.1.6 Material Selection	65

6.2 Sub-Surface Ablation Cell	66
6.2.1 Flow Pattern Study Inside the Cell Using Plexiglas Models	67
6.2.2 Final Cell Design	70
6.2.3 Material Selection	72
CHAPTER 7. EXPERIMENTAL SETUP	73
7.1 Instrumentation Layout in MDLEST	73
7.1.1 Laser	75
7.1.1.1 Laser Ablation Using Fiber Optics	75
7.1.1.2 Direct Laser Ablation	76
7.1.2 ICP-MS	76
7.1.3 ICP-AES	77
7.1.4 Robotic Surface Sampling Accessory (RSA)	79
7.1.5 Surface Sampling Probe	80
7.1.6 Sub-Surface Sampling Probe	81
7.2 Operational Configuration of the MDLEST	82
7.3 Soil Samples	83
7.4 Particle Size Distribution	84
7.4.1 Filters	84
7.4.2 Scanning Electronic Microscope (SEM)	85
7.4.3 Image Analysis	85
CHAPTER 8. RESULTS	86
8.1 Ablation Cells Performance Using the ICP-MS	86
8.1.1 Surface Ablation cell	87
8.1.1.1 Flow Deflector Ring Gap Effect	87
8.1.1.2 Cell Volume Effect	91
8.1.1.3 Flow Rate Effect	92
8.1.2 Sub-Surface Ablation Cell	94
8.1.2.1 Flow Deflector Channel Gap Effect	93
8.1.2.2 Flow Rate Effect	96
8.2 Ablation Cells Performance Using the ICP-AES	97

8.2.1 Flow Deflector Ring Gap Effect	98
8.2.2 Cell Volume Effect	100
8.2.3 Gas Flow Rate Effect	101
8.3 Particle Size Distribution Study	101
CHAPTER 9. CONCLUSION AND RECOMMENDATION	107
9.1 Conclusion	107
9.2 Recommendation	109
BIBLIOGRAPHY	111
APPENDIX A. THEORETICAL RESULTS OF PARTICLE MOTION IN THE ABLATION CELL	114
APPENDIX B. THEORETICAL RESULTS OF PARTICLE MOTION IN THE TRANSFER TUBE	118
APPENDIX C. DRAWINGS FOR SURFACE AND SUB-SURFACE ABLATION CELLS	122

LIST OF TABLES

Table 5.1: The regions of application of the equations for calculating F_D	38
Table 6.1: Ablation cell design evaluation	61
Table 8.1: The average signal intensity (counts/second)	88
Table 8.2: Particle size distribution of the entrained particles in the aerosol	103

LIST OF FIGURES

Figure 1.1: LA-ICP-AES/MS techniques	2
Figure 2.1: Inductively coupled plasma (ICP)	6
Figure 2.2: Atomic Emission Spectrometry using ICP as an ion source	7
Figure 2.3: Mass Spectrometry using ICP as an ion source	9
Figure 2.4: Effect of gas flow rate on signal intensity of ICP-AES	14
Figure 2.5: Effect of RF power on signal intensity of ICP	15
Figure 2.6: Effect of observation height on signal intensity of ICP	15
Figure 4.1: Ablation cell design by Thompson <i>et al</i>	19
Figure 4.2: Ablation cell design by Ishizuks and Uwamino	20
Figure 4.3: Ablation cell design by Gary	21
Figure 4.4: Ablation cell design by Mitchell <i>et al</i>	22
Figure 4.5: Cyclone chamber	23
Figure 4.6: Ablation cell design by Arrowsmith	23
Figure 4.7: Ablation cell design by Arrowsmith and Hughes	24
Figure 4.8: The three different cell designs for entrainment of the ablated material by Arrowsmith and Hughes	25
Figure 4.9: Emission signal profiles obtained for Mn (0.27%) in steel using: (a) 40 cm; (b) 70 cm; (c) 100 cm long PVC tubing	27
Figure 4.10: Effect of length of PVC tubing on the emission intensity of Mn(0.27%) in steel	27
Figure 4.11: Calculated transport efficiency of Mo particles	28
Figure 5.1: Particle size regions	34
Figure 5.2: Forces acting on a particle inside the ablation cell	39

Figure 5.3:	SEM photograph of ablated soil particles (NRM5)	42
Figure 5.4:	Aerosol flow regions inside the surface ablation cell	43
Figure 5.5:	Settling velocity of the ablated particles with $\rho = 2.65 \text{ g/cm}^3$	47
Figure 5.6:	Particle deposition in a 100-foot long tube due to the convective diffusion	49
Figure 5.7:	Particle deposition in a 100-foot long tube due to the gravity force	50
Figure 6.1:	Surface remote robotic soil sampling set up	52
Figure 6.2:	Ablation cell model no. 1	54
Figure 6.3:	Ablation cell model no. 2	55
Figure 6.4:	Ablation cell model no. 3	56
Figure 6.5:	Ablation cell model no. 4	57
Figure 6.6:	Ablation cell model no. 5	58
Figure 6.7:	Ablation cell model no. 6	59
Figure 6.8:	Ablation cell model no. 7	60
Figure 6.9:	Ablation cell design selection graph	62
Figure 6.10:	Surface Ablation Cell Design	63
Figure 6.11:	Flow Pattern inside the sub-surface ablation cell model	69
Figure 6.12:	Sub-surface ablation cell design	70
Figure 7.1:	A perspective view of the MDLEST showing the location of the instrumentation and utilities	74
Figure 7.2:	The Elan 5000 Inductively Coupled Plasma-Mass Spectrometer (ICP-MS)	77
Figure 7.3:	Assembled ICAP 61E spectrometer system (ICP-AES)	78
Figure 7.4:	Robotic Surface Sampling Accessory (RSA)	79
Figure 7.5:	The rastering patterns used for surface and sub-surface laser ablation	81
Figure 7.6:	The operational configuration of the MDLEST	82
Figure 8.1:	Signal intensity of the surface ablation cell without the flow deflector ring	87
Figure 8.2:	Signal intensity of the surface ablation cell with the flow deflector ring with 5.6 mm gap	88
Figure 8.3:	Signal intensity of the surface ablation cell with the flow deflector ring gap of 1.2 mm	89

Figure 8.4:	Signal intensities of the surface ablation cell; a- Si 29, b- U 238 and Th 232	90
Figure 8.5:	The output signal intensity oscillation of the ablation cell with one and two output ports	91
Figure 8.6:	The effect of cell volume on the output signal intensity of the ICP-MS	92
Figure 8.7:	Effect of the argon gas flow rates on the output signal intensity of the ICP-MS	93
Figure 8.8:	Effect of the deflector ring gap and gas flow rate on the output signal intensity of the ICP-MS with a different laser wavelength (1064 nm)	94
Figure 8.9:	Signal intensity of the sub-surface ablation cell with the flow deflector channel opening of 3.2 mm	95
Figure 8.10:	Signal intensity of the sub-surface ablation cell with the flow deflector channel opening heights of 3.2, 1.6, 0.8 mm	95
Figure 8.11:	Effect of the argon gas flow rates in sub-surface ablation cell on the output signal intensity of the ICP-MS	96
Figure 8.12:	Typical output signal of the surface ablation cell using the ICP-AES	97
Figure 8.13:	Signal intensity of the surface ablation cell with the flow deflector ring gap between 0.64 mm to 3.5 mm with 10^8 w/cm ²	98
Figure 8.14:	Signal intensity of the surface ablation cell with the flow deflector ring gap between 0.64 mm to 3.5 mm with 5×10^8 w/cm ²	99
Figure 8.15:	The effect of the deflector ring on the selectivity of the entrained ablated particles	99
Figure 8.16:	The effect of cell volume on the output signal intensity of the ICP-AES	98
Figure 8.17:	Effect of the cell volume on the selectivity of the entrained ablated particles	99
Figure 8.18:	The gas flow rate effect on the output signal intensity of the ICP-AES	101
Figure 8.19:	SEM photograph of aerosol sample on gold plated filter	102
Figure 8.20:	Particle size distribution of the generated aerosol inside the surface ablation with different gas flow deflector ring gap settings	103
Figure 8.21:	Percentage of the particle size distribution	104
Figure 8.22:	Percentage of the particle mass distribution	104
Figure 8.23:	Particle entrainment inside the ablation cell	105

ACKNOWLEDGEMENTS

I wish to express my appreciation to Dr. Jerry L. Hall and Dr. Edward J. Jaselskis, my major professors, for providing guidance, continual encouragement, and friendship during my doctoral program which made my graduate education not only a fruitful experience but also a pleasant one.

Sincere thanks are extended to professors Leo C. Peters, Loren W. Zachary, Palaniappa A. Molian, and David L. Carlson for their advice and service as committee members.

Also I would like to extend my appreciation to Dr. Donald T. Nobel, Marvin S. Anderson, Steve Braymen and other members of the Technology Integration Program for their support and help during my research.

I am grateful to Dr. Arthur P. D'Silva and Daniel S. Zamzow from Ames Laboratory for their advice and technical supports during running my experiment.

I would like to thank my mother for her patience and my brothers and sister for their endless and continuous support.

I would like to thank all of my family particularly, my wife, Sima Salehi and my children Milad and Saeid for their patience, understanding, and support during my graduate study.

My sincere gratitude is expressed in the memory of my father, whose constant moral support and dedication to education made this academic journey possible. My God bless his soul.

I wish to dedicate this dissertation to my late father, Bashir Bashirzadeh.

CHAPTER 1. INTRODUCTION

There are approximately 28,000 hazardous waste sites across the United States and nearly 1,800 of them are categorized as uncontrollable hazardous waste sites [1]. The Department of Energy (DOE) is responsible for cleaning up several sites that were contaminated as a result of producing weapons-grade nuclear fuels in different states since the 1940s. This remediation program is estimated to cost approximately 200 billion dollars and is projected to take about 30 years to complete [2].

In order to develop suitable remedial strategies, a knowledge of the location and composition of each waste site is essential. Today, this characterization process, requires that a sample of soil be sent to a fixed off-site laboratory for analysis. This process is not only time consuming and expensive but exposes a number of people to potential contamination. A better approach would be to use field-deployable analytical instruments to detect contaminants. Today, a number of field-deployable analytical instruments are available to detect organic and volatile organic contaminants. But such field-deployable analytical instruments which have appropriate detection limit and can provide real-time in-situ data for heavy metals (inorganic materials) are not yet commercially available.

The Technology Integration Program (TIP) at Ames Laboratory, a DOE laboratory, has adopted *Laser Ablation-Inductively Coupled Plasma-Atomic Emission Spectrometry/Mass Spectrometry* (LA-ICP-AES/MS) techniques for soil sampling and analysis. They have integrated the necessary equipment into a mobile laboratory to have a real-time field screening unit that can fulfill the Department of Energy's need for a rapid and safe field-deployable analytical instrument. This analytical unit, Mobile Demonstration Laboratory for Environmental Screening Technology (MDLEST), was designed and built between 1991 and 1992. The MDLEST was successfully tested at Fernald, Ohio in the summer of 1992.

The LA-ICP-AES/MS as shown in Figure 1.1, are two-stage techniques to determine the radioactive waste contamination of soil in a very short period of time. In the first stage (sample collection and preparation stage), a high-power Q-Switched pulsed laser beam is focused on the surface of a soil sample isolated from the atmosphere by an ablation cell. Then, the laser ablates the soil and produces very fine particles by vaporization, atomization, spallation, and/or ejection of material from the soil surface inside the ablation cell. These ablated particles are entrained into an inert gas (argon) flowing inside the ablation cell and are then transferred to the analyzing instruments via a transfer line (tygon tubing). In the second stage (sample ionization and analyzing stage) the ablated particles are injected into an ICP, which is a high temperature (8000 K) plasma torch, for ionization. The sample is vaporized, atomized, ionized, and electronically excited in a very short period of time (ms) when it is introduced into the ICP torch. Relaxation of this electronic-excitation produces atomic and ionic emission spectra which is characteristic of the sample introduced into the ICP. Then, an *Atomic Emission Spectrometer* (AES) is used to detect the ICP emission signals for multi-elemental analysis.

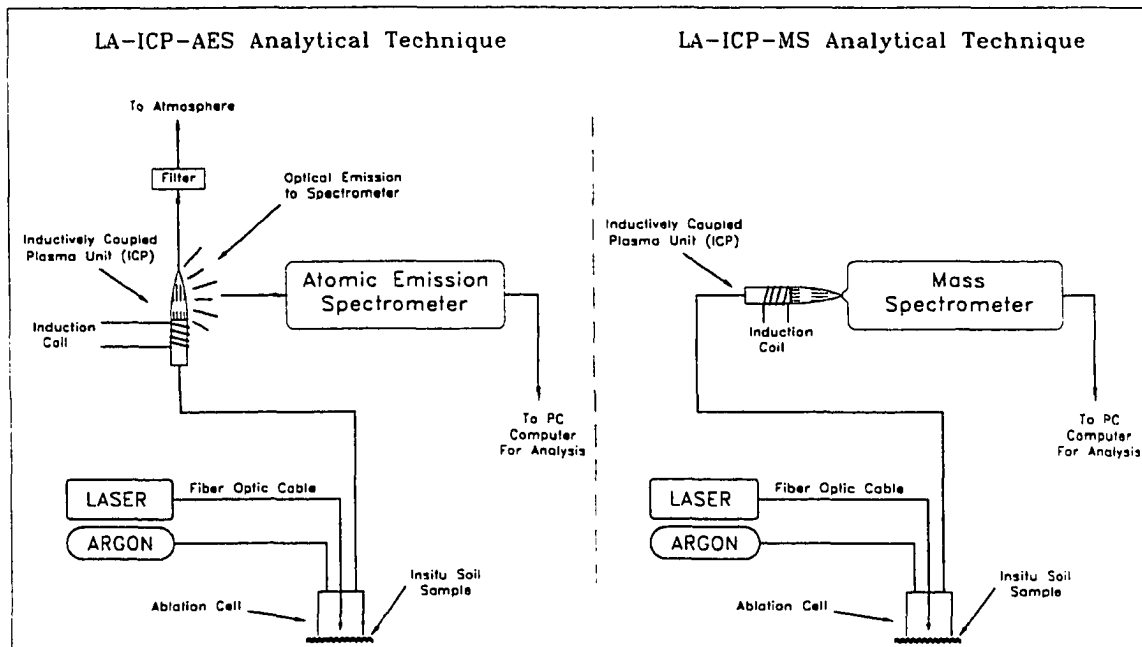


Figure 1.1: LA-ICP-AES/MS techniques.

In *Mass Spectrometry* (MS), the ions produced in the plasma are passed through a set of ion lenses and mass analyzer, which are mounted inside a vacuum chamber, to detect ions and hence the elements in the sample.

The precision and accuracy of LA-ICP-AES/MS mainly depend on the physical and chemical properties of the soil sample and on the characteristics of the components of the instruments used for testing. These components include the laser, the ablation cell, the transfer line, the ICP, the AES, and the MS. Each of these components can significantly affect the quality and quantity of the out put signal.

The ablation cell is where the laser interaction with the soil occurs and where particle entrainment takes place. This is the heart of the sample collection and preparation stage (first stage) and has a very important effect on the signal characteristics of the AES and MS. This study is mainly focused on the study of the ablated particles entrainment in gas flow inside the cell and design of two ablation cells (surface and sub-surface) to improve the signal response of the system by maximizing the number of desired size particles entrained in the gas flow.

CHAPTER 2. BACKGROUND

In this chapter the *Laser Ablation-Inductively Coupled Plasma-Atomic Emission Spectrometry/Mass Spectrometry* (LA-ICP-AES/MS) analytical methods used by Ames Laboratory to satisfy the Department of Energy's need for a real-time, in-situ, safe, and inexpensive site screening technique for remediation of its nuclear energy complexes are briefly explained.

2.1 System and Components Description

The LA-ICP-AES/MS systems are two-stage techniques that have been deployed by the Ames Laboratory for elemental soil analysis. These two-stage techniques have several advantages compared to direct spectrometry of the primary source and are very suitable alternatives for in-situ real-time elemental analysis. In the first stage, sample collection, preparation, and transportation are performed at atmospheric pressure using a laser, an ablation cell, and a transfer line. In the second stage, ion and atom formation and the measurement of their intensities are accomplished by ICP-AES/MS. These methods allow optimization of either of the two stages in order to enhance the output signal intensity.

2.1.1 Laser Ablation

Laser ablation (LA) is a new and versatile sampling technique capable of sampling a wide range of diverse materials ranging from conducting and nonconducting, inorganic and organic, to solid and powdered materials. Lasers have been widely used for cutting and drilling

materials in industry for several years, recently, there is increased interest in using laser ablation as a particle generating device for direct elemental analysis without extensive sample preparation in analytical chemistry. The use of a laser to vaporize, dissociate, excite, or ionize species on solid surfaces has the potential of becoming a powerful analytical tool [3].

Laser ablation is a complex process and is not fully understood. But it may be roughly described as absorption of the laser radiation by a solid sample which leads to material removal from the surface by electronic excitation, bond breaking, heating, desorption or evaporation. Absorption of laser beam energy by a sample increases the surface temperature up to 3000 K in a very short period of time. The rapid temperature change will melt and evaporate the sample very quickly. This process generates a very high vapor pressure which is the main driving force in the laser ablation. In brittle solids, the evaporation recoil may approach or exceed the elastic limit. The formation and the propagation of this type of shock wave in solids can produce spalling, which is a form of ablation. Brittle fracture can also occur just due to thermal stresses. Ablation products are atoms, molecules, clusters or large particles excited from the irradiated surface. These products could be entrained in argon gas flow and transferred to the analytical unit (ICP-AES or ICP-MS) by appropriate transfer line.

In general, samples are introduced into an *Inductively Coupled Plasma* (ICP) torch as a solution. In the case of solid samples, the conventional method of sample introduction to the ICP is to prepare a 1% solution (weight/volume) of the sample in an appropriate acid mixture and then transfer it to the ICP. This method has several limitations in the analysis of materials and is time consuming and inconvenient for rapid field analysis [4].

The advantages of using a laser for analysis of solids are: 1- little or no sample preparation, 2- high sample output, 3- application to almost all materials, and 4- high spatial resolution, allowing analysis of small selected areas [5]. The particle size distribution of the laser ablated particles is unknown and depends upon the laser power density, pulse duration, wavelength and physical properties of the ablated materials [6].

2.1.2 Inductively Coupled Plasma

The *Inductively Coupled Plasma* (ICP) is an extremely versatile high-temperature source for nearly all the elements in a sample for *Atomic Emission Spectrometry* (AES) and *Mass Spectrometry* (MS). Generally, there are three types of plasmas used in analytical emission spectroscopy for the analysis of solid, liquid, and gaseous samples. These are the *Inductively-Coupled-Plasma* (ICP), *Direct-current-Plasma* (DCP), and *Microwave-Induced-Plasma* (MIP) respectively. The ICP is the standard ion source for AES and MS because it gives high excitation temperature, is relatively immune to chemical interferences, and has a large linear dynamic range [7]. In the ICP, the energy for creating the high-temperature plasma is generated by a high-frequency magnetic field.

The ICP torch consists of two concentric quartz tubes (Figure 2.1) with argon gas passing between these tubes to provide cooling for torch. The argon gas carrying the sample of particles (aerosol) enters the torch from the bottom of the inner capillary tube. An oscillatory current

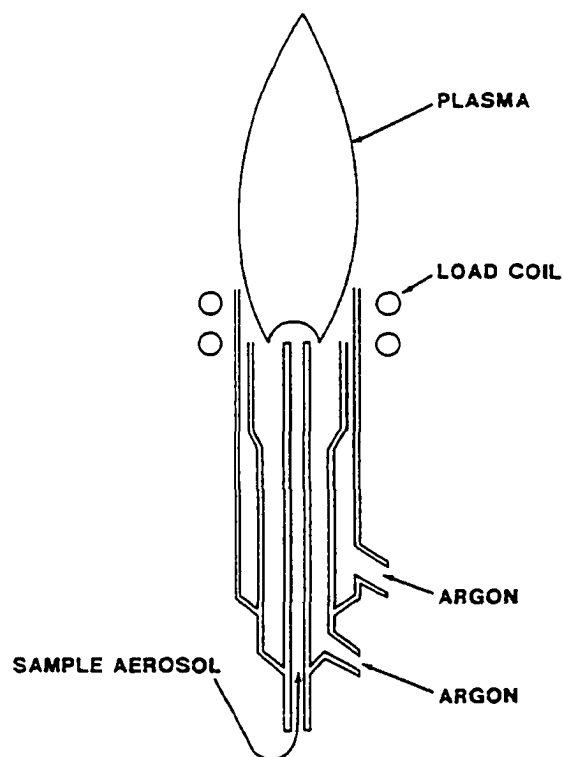


Figure 2.1: Inductively Coupled Plasma (ICP).

generated by a radio frequency (RF) generator passes through an induction coil mounted around the open end of the torch. This coil acts as a primary winding of a transformer. The argon gas carrying the particles acts as a secondary winding which is coupled inductively to the radio frequency energy source. The magnetic field created by the induction interacts with the aerosol when an initial ionization is provided by a Tesla discharge. The high-temperature plasma torch (5000-10,000 K) is capable of ionizing many elements with more than 90% efficiency [8].

2.1.3 Atomic Emission Spectrometry

Atomic Emission Spectrometry (AES) is an excellent method for the analysis of trace elements in various samples when it is coupled with the ICP torch. The AES is a high resolution spectrometer and depending on the spectroscopic detection arrangement, it can perform simultaneous multi-element quantitative and qualitative analysis. This instrument can analyze soil samples to determine radioactive (U, Th, etc) or other elemental contaminants (Pb, Cr, etc) with different degrees of accuracy depending on the concentration.

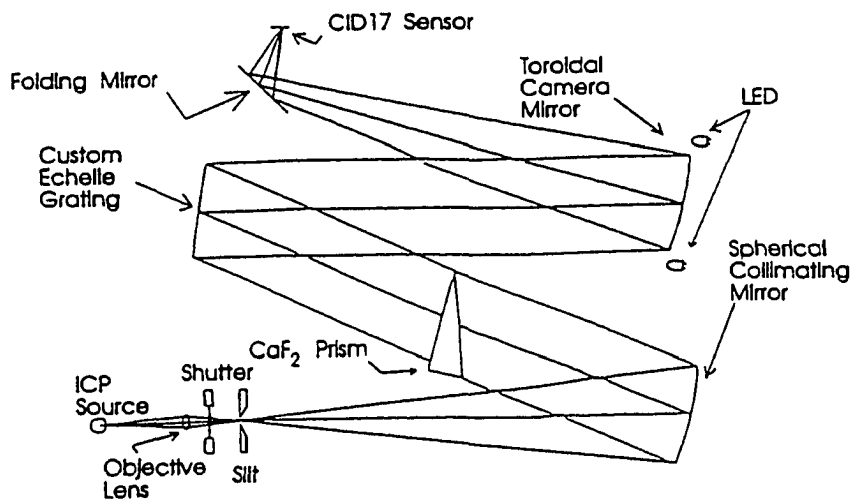


Figure 2.2: Atomic Emission Spectrometry using ICP as an ion source.

When an atom is exposed to a high-temperature energy source, such as an electrical discharge (ICP), energy is transferred to the excited atoms by collisions with energetic particles and by interaction with electromagnetic radiation. Then the excited atoms decay to a lower energy level with emission of their own characteristic electromagnetic radiation. Electromagnetic radiation emitted is focused onto the entrance slit of a spectrometer directly or by using a fiber optic cable (refer to Figure 2.2). The incident radiation is resolved into discrete energy components by the spectrometer and is measured with a photomultiplier tube (PMT) detector that converts the radiation energy to an electrical current. The magnitude of the current, which is proportional to light intensity, is then measured with a very high speed data acquisition system. By separating the electromagnetic radiation into its components and measuring the wavelength, the element and some times the specific isotope can be identified.

2.1.4 Mass Spectrometry

Mass Spectrometry (MS) is a powerful technique used for rapid analysis of trace elements in analytical chemistry. It can measure the presence of more than 75 elements, all within a single scan. The MS has proven to be extremely sensitive, with solution detection limits in the range 10^{-9} - 10^{-15} g/mL (1-1000 ppt), typically 10-100 times lower than for the ICP-AES [8].

In the sample analysis by the ICP-MS, the aerosol sample is excited by the high temperature plasma source (ICP) in the same manner as in ICP-AES. Because of the very low pressure in the vacuum chamber (10^{-6} torr), the plasma flows through a circular orifice (with a 0.5-1 mm diameter) into a vacuum chamber (refer to Figure 2.3). After entering inside the vacuum chamber of the MS, the plasma which contains the excited atoms and ions is focused by a set of ion lenses and then transferred to a quadrupole mass analyzer. Ions of selected mass to charge ratio (m/z value) leave the mass analyzer and are deflected into an electron multiplier for detection. The intensity of the detected signal is proportional to the number of ions arriving from the ICP.

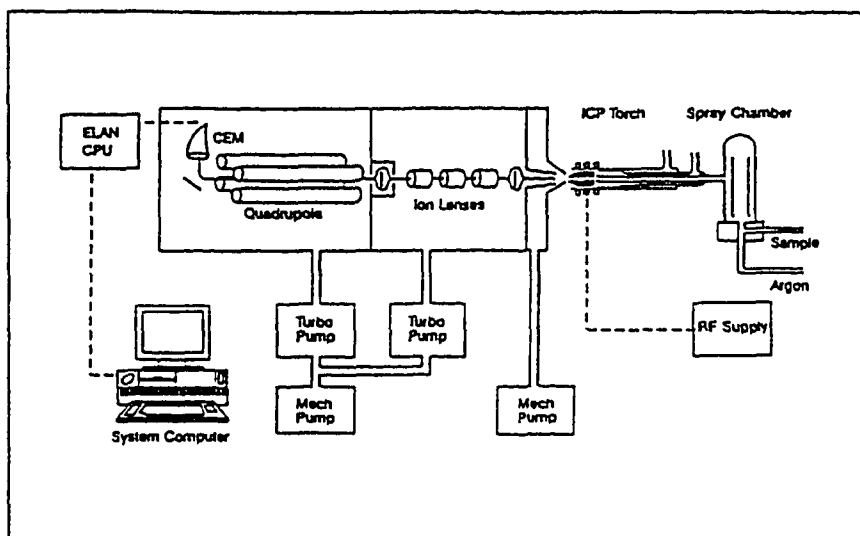


Figure 2.3: Mass Spectrometry using ICP as an ion source.

2.2 System Performance and Reliability

The overall performance and reliability of these two (ICP-AES/MS) different analytical techniques and the precision and accuracy of the results mainly depends on the characteristics and the performance of their individual components and sample characteristics. The laser, sample, ablation cell, transfer line, ICP, AES, and MS are the main components of these two techniques that will be discussed in more detail in the sections that follow.

2.2.1 Laser

Different types of lasers have been successfully deployed for laser ablation (Nd-YAG, Excimer, Ruby, and Carbon-dioxide lasers). A sufficiently high power density (typically more

than 10^7 W/cm^2) is the main requirement for a laser in order to effectively ablate and evaporate diverse sample materials [9].

Understanding laser-material interactions and the nature of the ablated particles is an important prerequisite to the application of laser sampling for chemical analysis. The amount and size of the sample particles generated during the ablation process have a significant effect on the signal response of the instruments used in this study (ICP-AES/MS). The laser power density, wavelength, pulse duration, and pulse repetition rate (frequency) affect the number and nature of the ablated particles.

2.2.1.1 Laser Power Density

The amount of laser energy incident on the sample is critical because this controls the ablation yield and therefore the resultant signal intensity. The amount of the ablated materials from the soil sample increases proportionally with the increasing power density of the laser beam. Below a laser radiation threshold of 10^7 watts/cm^2 there will be no macroscopic removal of material. At higher power densities there is at first a strong increase in the ablated rate followed by a saturation effect [10].

The laser power density is also a critical factor in generating a non-selective, uniform ablated particle aerosol flow into the ICP. The amount of evaporation of all constituents of the soil sample mainly depends on the amount of the energy absorbed by each element, the boiling point, and the thermal conductivity of the element. In a high power range ($>1 \times 10^9 \text{ watts/cm}^2$), both metals and insulators behave similarly, i.e. a free electron plasma ($100 \mu\text{m}$) above the surface controls the ablation[11]. Therefore by using a high power density pulsed laser beam, the selectivity of the ablated elements could be minimized.

2.2.1.2 Laser Wavelength

The coefficient of the reflectivity of different materials varies with the wave length of the laser beam used during the ablation process. The shorter the wave length, the smaller the reflectivity and therefore, the more energy will be absorbed by the different elements. The optimum wavelength for an effective laser ablation is in the ultra violet and visible range (250-650 nm).

It was found by Eloy [12] that laser wavelength influences the plasma formation and ionization process. The degree of ionization of all elements inside the laser plasma can be increased with use of a shorter wavelength. These findings are in good agreement with experiments performed by Bringham and Salter [13]. In the analysis of a steel standard using a laser as an ion source for mass spectrometry, they found the highest sensitivity for elements P, S, Ti, V, Cr, Mn, Ni, Co, Cu, As, Zr, Mo, Nb, Ta, W with ruby laser (694.3 nm) evaporation. The intensities obtained with a Nd-YAG laser (1.06 μm) were similar but lower in all cases to those for ruby laser vaporization.

2.2.1.3 Laser Pulse Duration

The amount of material removed by each laser pulse during the ablation process depends on the physical properties of the sample and (for a given wavelength and energy) the pulse duration of the laser. A Q-Switched pulsed laser removes significantly smaller amounts of ablated materials compared to relatively long duration free-running pulsed lasers [6]

Short duration laser pulses ($< \mu\text{s}$) tend to generate smaller particles than longer laser pulses [5]. From a study of the interaction of Nd glass laser with Ni, Mo, Cu, and Al, Chun and Rose [14] calculated that 80 to 90 percent of the materials were removed as liquid when the pulse duration was longer than 100 μs .

2.2.1.4 Laser Frequency

A high repetition-rate (100-Hz) laser ablation system with moderate laser energy (50 mJ) was used by Ho-ming Pang *et al.* [15] in an attempt to improve the measurement precision and sensitivity. The precision for the major and trace elements was improved with the use of high repetition rate even when the surface was damaged toward the end of experiments.

For a fixed time, a lower frequency gives a smaller emission intensity because less sample is ablated and reaches the plasma. By using a high pulse repetition rate, the sample concentration build up in the plasma would be steady, which should lead to a much more uniform response and possibly to higher precision [16]. Also, the high reproducibility and repetition rate of the laser results in a continuous signal and improved precision and duty cycle.

2.2.2 Ablation Cell

The ablation cell, the chamber in which the interaction of laser with the sample and entrainment of the ablated materials in the gas flow takes place, is the heart of the sample preparation portion (first stage) of the LA-ICP-AES/MS system. A proper cell with optimized cell volume, flow rate, and flow velocity interacting with particles can generate a constant aerosol density resulting in increased signal intensities and improved signal quality.

2.2.2.1 Cell Volume

Cell volume could affect the signal response time and aerosol density. A large volume cell tends to excessively dilute the aerosol and results in poor reproducibility. Small cells result in sputtering of the ablated plume onto the cell wall and quartz window, with a resultant loss in sensitivity.

2.2.2.2 Gas Flow Rate

The gas flow rate into the ablation cell determines the gas velocity inside the cell. The higher the gas velocity, the more ablated particles will be entrained in the aerosol leaving the ablation cell. On the other hand, very high gas flow rate decreases the residence time of particles in the ICP and lowers the signal intensity. The optimum argon gas flow rate for the ICP-AES/MS is between 0.8-1.2 l/min [17].

2.2.2.3 Flow-Particle Interaction

Flow interaction with ablated particles is very important during the particle entrainment process inside the ablation cell. The flow pattern and velocity affect the size and number of the particles entrained in the gas flow inside the ablation cell. The size and number of particles transferred to the ICP has a very pronounced effect on the output signal characteristics of the ICP-AES/MS.

2.2.3 Soil Sample

The amount of the material evaporated by the laser radiation is influenced by the physical properties and chemical compositions of the sample. Soil grain size and compaction are two factors that could have some effect on the amount of the ablated material. The amount of moisture in soil is another factor that affects the particle generation rate by the laser beam. The high moisture content in soil will decrease output signal significantly, because, the major part of laser beam energy is absorbed by water during the evaporation process and less sample material is ablated.

2.2.4 Inductively Coupled Plasma (ICP)

The ICP is an universal ion source for nearly all the elements in a sample. The excitation and ionization level of the aerosol sample introduced into the ICP could be affected by the following parameters:

2.2.4.1 Amount of Ablated Material

The signal intensity of the ICP is directly correlated with amount of the ablated material transported into the ICP. An excessive introduction rate of material (greater than 1 mg/s) could extinguish the plasma[18]. On the other hand, a low concentration aerosol (less ablated particles) will decrease the ion generation rate in the plasma resulting in poor signal intensity. Ishizuku and Uwomino [19] suggest that to maintain a stable plasma, the amount of ablated material must be controlled within several tens of $\mu\text{g/s}$. Therefore, there must be enough fine particles transferred into the ICP to maintain an uniform and high intensity ion source for AES or MS.

2.2.4.2 Gas Flow Rate

Gas flow rate is a critical factor in the operation of the ICP in the both ICP-AES and ICP-MS units. The residence time of the particles and consequently the atomization and ionization efficiencies are depend on the aerosol flow rates entering to the ICP at equal temperature [20]. High flow rate decreases the residence time of the particles in the ICP and results in a lower signal intensity. As shown in Figure 2.4, depending on the instrument and sample, there is always an optimum flow rate for the aerosol sample introduced in to the ICP.

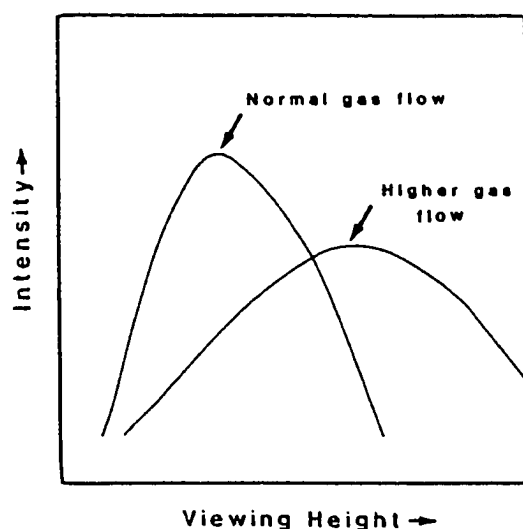


Figure 2.4: Effect of gas flow rate on the signal intensity of ICP-AES.

2.2.4.3 Radio Frequency (RF) Power

The radio frequency power variation can also effect the line intensities in an ICP-AES system used for elemental analysis [21]. Figure 2.5 depicts the RF power effect on the soft and hard lines intensities of an ICP-AES. Curves I to III show the effect of increasing RF power on a soft line (A) and a hard line (B). Soft lines are atomic lines of elements with a low medium ionization potential (<8 eV). Hard lines are both atomic and ionic lines with greater excitation potentials.

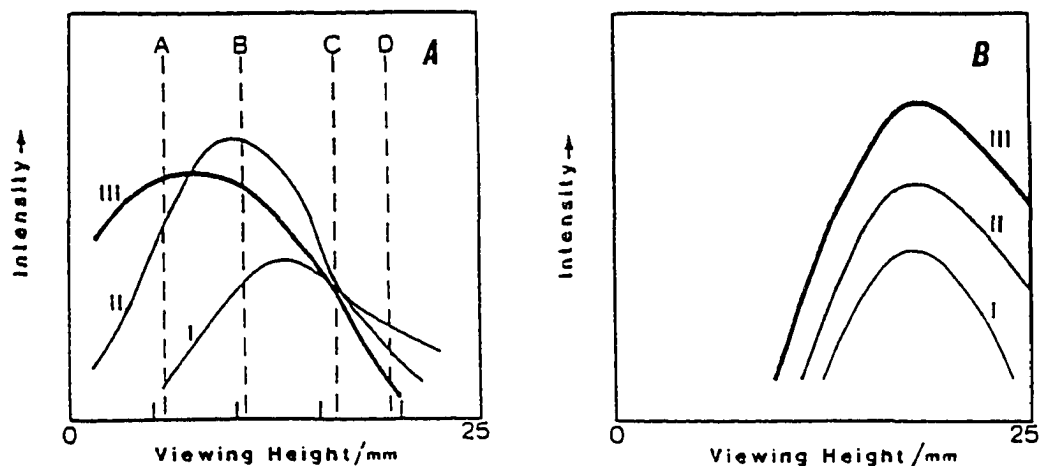


Figure 2.5: Effect of RF power on the signal intensity of ICP.

2.2.4.4 Observation Height

In the ICP-AES, the choice of the optimum observation height for measuring the emitted electromagnetic radiation in the plasma is very critical. In multielement ICP analysis, the plasma region is selected by compromise. As shown in Figure 2.6, there is an optimum observation height for each of the soft and hard lines in which the signal intensity is maximum.

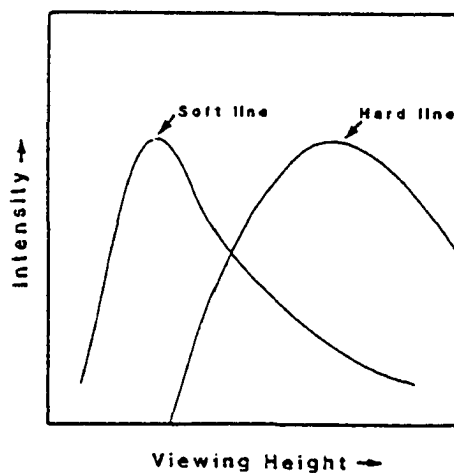


Figure 2.6: Effect of observation height on the signal intensity of ICP.

CHAPTER 3. OBJECTIVE

The objective of this study was to design, fabricate, and test two in situ ablation cells (surface and sub-surface) for LA-ICP-AES/MS for first the time in the field-deployed analytical instrumentation. A well designed ablation cell can improve the quality of the output signal significantly by generating a continuous and homogenous aerosol for the ICP.

The interaction of the laser beam with the soil sample, generation of ablated particles, entrainment of the ablated particles in the argon gas stream, and deposition of the very large ablated particles all are accomplished inside the ablation cell. Therefore, the ablation cell design is crucial in providing a homogenous and continuous mixture of particles in sufficient quantities for accurate analysis, especially if the mass spectrometer analysis is used. The ablation cell can also modify and decrease the effects of the change in the laser parameters and soil characteristics on the output signal.

The number of the very fine particles in the argon gas stream (aerosol density) is also a critical factor affecting the output signal intensity of both atomic emission and mass spectrometers. By increasing the number of the very small ablated soil particles in the aerosol transferred into the ICP, the signal intensity could be increased significantly. In general, because of their small mass, very fine soil particles (less than 2-3 μm in diameter) have a higher chance of complete dissociation, atomization, ionization, and excitation in the ICP than the large particles. Therefore, by entraining very fine particles in the argon gas flow (aerosol) and depositing large particles inside the cell, the signal fluctuation and instability due to the presence of the large particles could be decreased significantly. The rise time of the output signal, with a fixed gas flow rate, is a function of the effective ablation cell volume. Thus, the response time of the output signal can be improved by optimizing the cell volume.

The design criteria for the both ablation cell designs are as the following :

- 1- Maximize the number of transferred ablated particles with diameter of less than 2-3 μm ;
- 2- Minimize the signal fluctuation due to presence of the large particles and/or change in the aerosol density;
- 3- Minimize the effective cell volume for better signal;
- 4- Cover at least one square inch of the soil sample;
- 5- Minimize the argon gas leak into the soil;
- 6- Keep quartz window clean from deposition of the ablated materials to minimize the laser power loss;
- 7- Minimize the laser power loss due to the scattering of the laser beam by the presence of the ablated particles; and
- 8- Minimize the assembling and disassembling time during testing in the field.

CHAPTER 4. LITERATURE REVIEW

Laser ablation is a new technique used in analytical chemistry to collect samples for elemental spectrometry. This technique has several advantages over complex and time consuming conventional method of solid sample preparation which dissolves the solid using acid dissolution. Minimum sample preparation is required for laser ablation and can be applied to almost all materials. Because of high spatial resolution, little material is removed and analysis of very small selected areas is possible. Since the generation and transfer of the ablated particles is done in a very short period of time, this technique of sample collection could be used for real-time elemental analysis using ICP-AES/MS. The ablation cell and transfer line are the key elements of the first stage (sample collection and preparation stage) and control the overall efficiency of the solid sample introduction to the ICP-AES/MS during laser ablation.

4.1 Ablation Cell

The primary function of the ablation cell is to effectively transfer the different size of ablated particles from the surface of the sample to a second ionization source (ICP). The dependence of the ablated particle size distribution on different parameters of laser and soil properties was explained in more detail in chapter 3. The ablation cell is another important component of the laser ablation process which has very distinct effect on the size distribution of the entrained particle. An optimum cell design can significantly improve and enhance the signal characteristics of the system by efficiently entraining and transferring very fine ablated particles to the ICP. According to Cameron *et al.* [22] sample cell design is a key element in the laser ablation process.

Recent work done by Chenry *et al.* [23] shows that a substantial part of materials mobilized from a metallic target is in the form of particles in the size range 0.1–10 μm . They also conclude that particles of 2 μm in diameter or smaller account for about 90% of the particle population and only a few percent of the total mass, for a wide selection of materials with diverse physical characteristics.

Thompson *et al.* [24] used one of the first ablation cell designs in their study of the LA-ICP-AES. This cell enclosed the sample and had 35 mm inside diameter and 17 mm height (Figure 4.1). A 92-cm long flexible PVC tubing with 6 mm inside diameter was used to transfer the ablated particles to the plasma torch. They also used cells with various diameters from 20–50 mm (5–30 cm^3 volume) to accommodate samples of different size. There was a decrease in the output signal intensity but the decay time of the signal did not depend on the volume of the cell. Although it was slightly affected by the position of the sample in the cell, they suggested that there was little mixing between the plume of vaporized material and surrounding gas in the chamber. They also recommended that further work on cell design be accomplished.

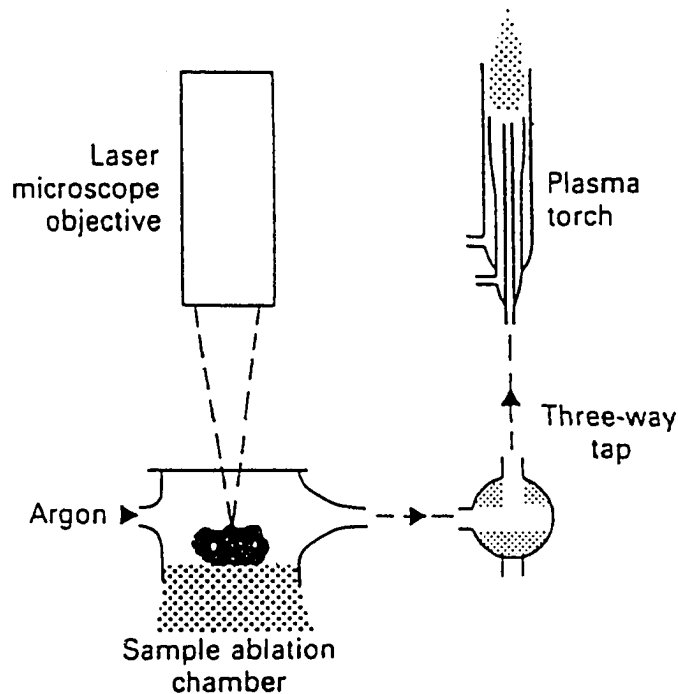


Figure 4.1: Ablation cell design used by Thompson *et al.*

Ishizuka and Uwamino [25] first used a stainless-steel wall cell with an inside diameter of 40 mm and height of 30 mm with a Pyrex glass window (Figure 4.2). They used a 4 mm inside diameter flexible PVC tubing to transfer particles from cell to the ICP. The emission profiles they obtained with this cell did not show clear and reproducible signal peaks. According to them, this must be due to diffusion of the laser plume in the cell. Then, they used a smaller size cell (13 mm inside diameter and 35 mm height) to get better signal peaks. They suggested that a cell with as low volume as possible was preferable for obtaining clear and reproducible emission profiles. However, in the case of a very small cell, the laser plume produced by the laser shot collided with the cell wall and the window resulting in a decrease in signal intensity. In conclusion, they suggested that an optimum ablation cell design of for ICP torch system is required.

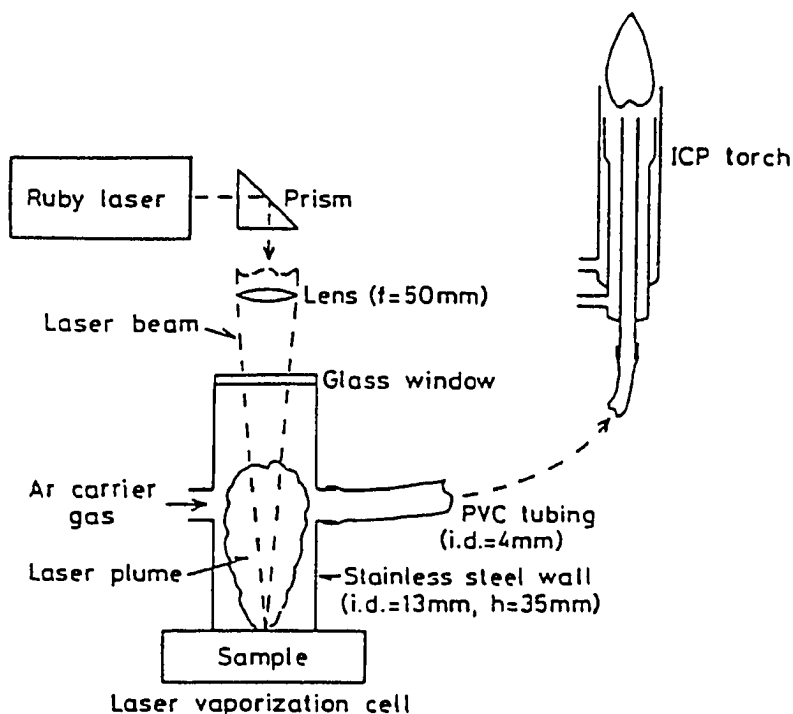


Figure 4.2: The ablation cell used by Ishizuka and Uwamino.

In another cell design, Gray [16] used a 50 mm diameter borosilicate glass cylinder ablation cell (Figure 4.3) for ICP-MS. The sample gas flow was introduced tangentially to the cell, at the level of the sample, so that a swirling motion across the surface was produced. A 150-cm long and 4 mm inside diameter PVC tube connected the cell to the torch.

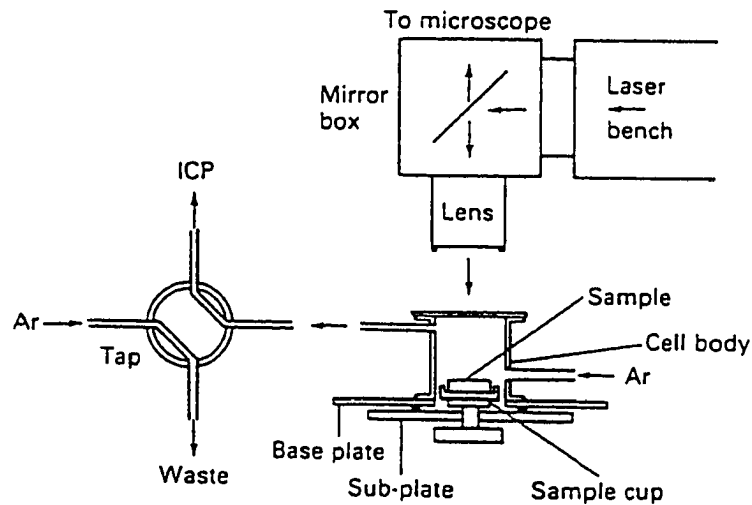


Figure 4.3: Ablation cell design by Gary.

In a study done by Mitchell *et al.* [26], the effect of cell design on the precision of the output signal is explained. They used an ablation cell with 1.0 cm inside diameter and 5.0 cm height for ablation of pelletized copper powder in potassium bromide matrix (see Figure 4.4). A flow of Argon gas (1–1.5 l/min) passes across the top of the sample carries ablated particles into a *Direct Current Plasma* (DCP) excitation source. The initial percent of Relative Standard Deviation (%RSD) of the signal was 11–20%, but it was decreased to 2–6% when they modified the ablation cell. They reported that the ablation process produced relatively large fragments, micron-sized particles, and vaporized material. Because of their transient residence time in the plasma, large particles were not completely vaporized. Thus, they caused an erratic flow of partially dissociated particles and created instability in the plasma.

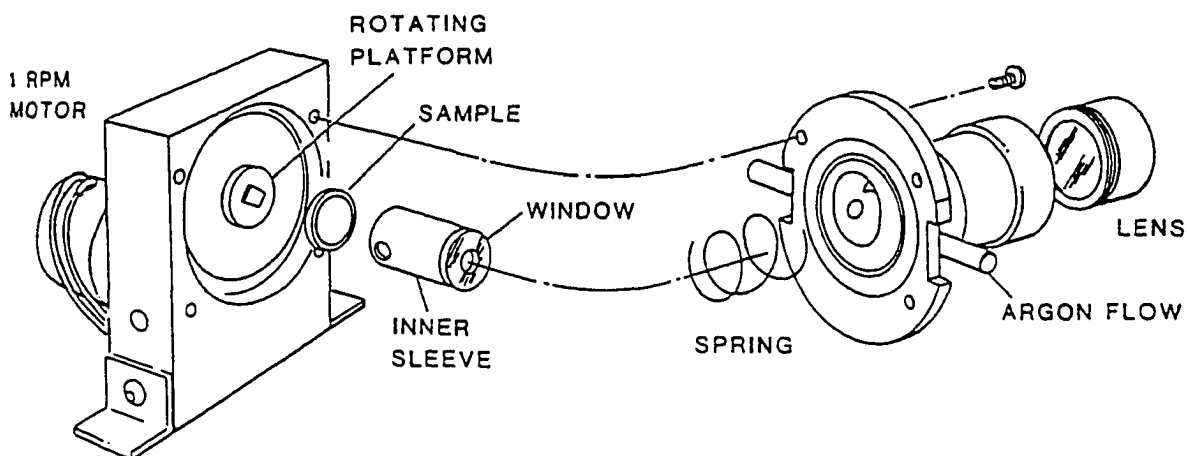


Figure 4.4: Ablation cell design by Mitchell *et al.*

Mitchell *et al* also used a cyclone chamber, as shown in Figure 4.5, in testing powder samples to prevent the plasma instability and flickering of the signal by separating and depositing large particles inside the chamber. They claimed that if the cyclone chamber was not used, flickering, plasma instability, and spikes in the signal could increase the %RSD to over 30% and over a long period of time (several hours) gave a drift in the base-line signal.

Arrowsmith [5] used a demountable Pyrex glass cell clamped to an aluminum base with an o-ring seal (Figure 4.6) to study the direct elemental analysis of solids. The aerosol transport gas at atmospheric pressure was introduced into the base tangentially to produce a swirl flow around the sample. The inner volume of the cell was small (approximately 30 cm³) to minimize dilution of the ablated particles. A 50-cm long and 6.4 mm inside diameter Tygon tube was used to transfer ablated particles (aerosol) to the ICP torch. This design has the disadvantage that translation in the vertical direction causes the laser beam to move across the sample surface.

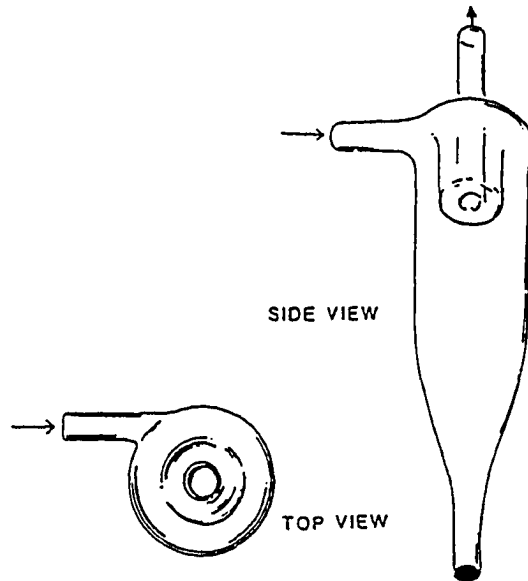


Figure 4.5: Cyclone chamber.

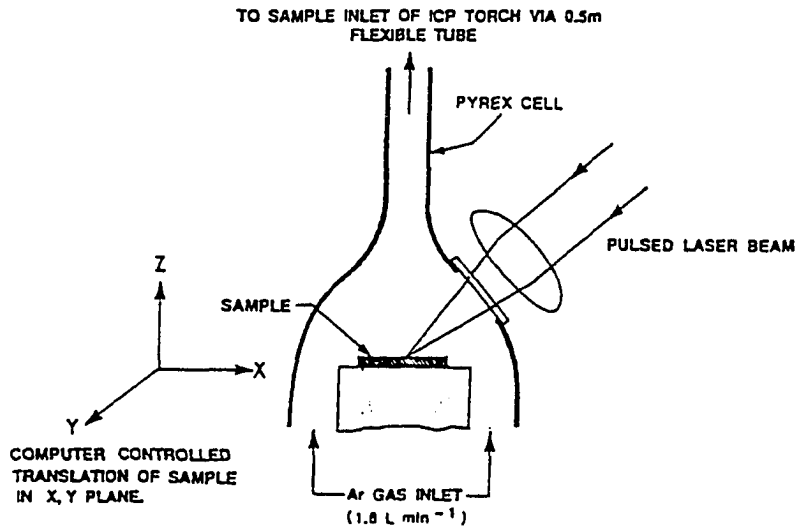


Figure 4.6: Ablation cell design by Arrowsmith.

Arrowsmith and Hughes [6] studied the response and efficiency of three different cell designs. As shown in Figure 4.7, the ablation system consists of two main parts: an outer box and a small ablation cell that encloses the plume of material but does not form a seal to the sample surface. The XYZ sample rastering unit and ablation cell are placed inside this box. The first cell design was a windowless cell (see Figure 4.8.a) with gas flowing into the cell from the top and around an opening at the base of the cell. There was an initial rise in signal when the laser was turned on and a fast decline followed by a slow decline when the laser was turned off. The slow signal decay of this cell was undesirable, since it prevents rapid independent

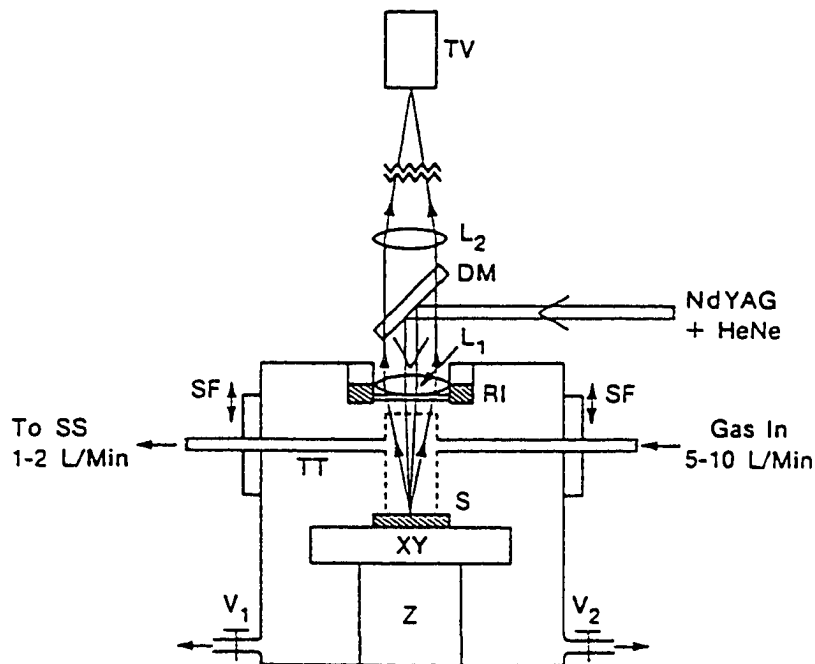


Figure 4.7: Laser ablation system used by Arrowsmith and Hughes. TT is the transfer tube; SS secondary source; SF sliding flange; L_1 and L_2 are lenses; DM is a dichroic mirror; RI is ring illuminator; V_1 and V_2 are flow control valves; and S is the sample sits on the XYZ translation stage.

analysis of different samples and could give rise to memory effects. The top of the second cell design, which was exactly like the first cell design, was sealed with a quartz window in order to prevent the loss of ablated material from the top of the cell (Figure 4.8.b). The gas flow was introduced from a one millimeter opening between the bottom of the cell and sample surface. A slow signal decay similar to the first cell design was obtained indicating that material is ejected sideways with sufficient velocity to escape through the incoming gas flow at base of the cell. In the third cell design, they used two concentric tubes with the inner tube inside diameter of 10 mm. The inlet gas flowing between these two tubes was symmetrical to create a gas sheath around the base of the cell. The signal and transient response were observed to be insensitive to changes in the inlet gas flow over the large range 5–10 l/min and to gap distance of 0.3–3 mm between the base of the wall and the sample surface. This cell was the most effective cell design and gave signals comparable to those obtained with an enclosed cell.

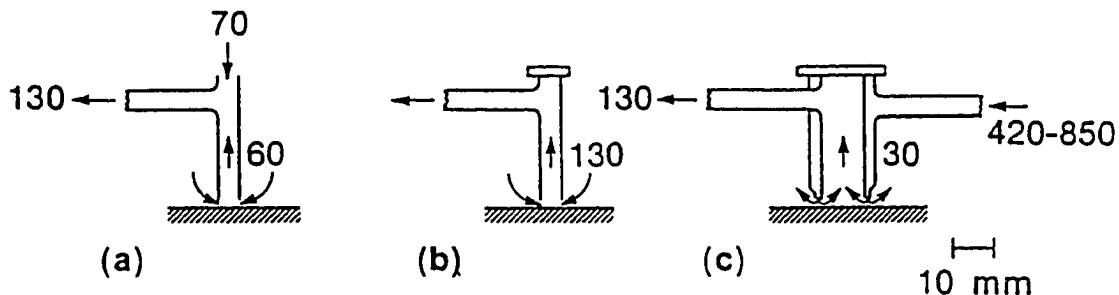


Figure 4.8: The three different cell designs for entrainment of the ablated material by Arrowsmith and Hughes. Cells are to scale and approximate average flow velocities are in cm/sec.

4.2 Transfer Line

In most of the elemental analysis performed in laboratories, using LA-ICP-AES/MS, the transfer line length was kept at minimum in order to increase the particle transfer efficiency. In this study, since the distance between the sample site (laser ablation process) and analytical unit (ICP-AES/MS) is relatively long (30 meters), the transfer line effect on the efficiency of aerosol transportation is very important. Tube length, tube diameter, and tube material influence the number and size of particles transferred from the ablation cell to the ICP. Gravitational deposition of large particles ($> 1\ \mu\text{m}$) and diffusion loss of very small particles ($0.001\ \mu\text{m}$) inside the tube are two major factors that determines the transfer efficiency of the transfer line.

Ishizuka and Uwamino [19] studied the effect of the transfer line length on the signal intensity. The peak-height decreased gradually with increasing tube length (Figure 4.9). The increase in the transfer line length also resulted in peak broadening. They also used a Q-Switched laser and a normal laser to study the transfer line effect on signal intensity. They reported that the degree of the decrease in the intensity with increasing tube length was larger

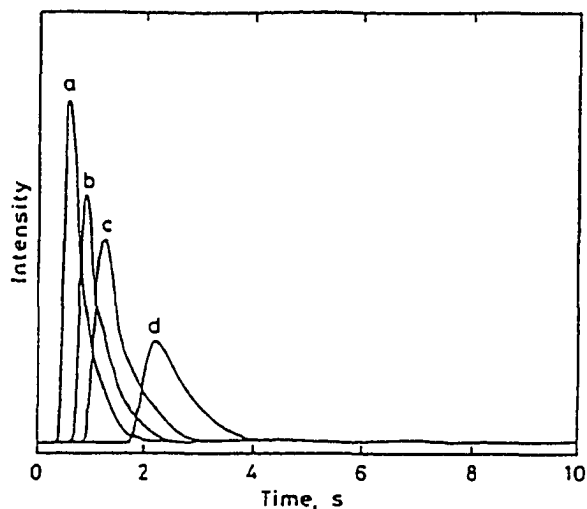


Figure 4.9: Emission signals profiles obtained for Mn (0.27%) in steel using: (a) 40 cm; (b) 70 cm; (c) 100 cm; (d) 200 cm long PVC tubing. Reference [19].

in the Q-Switched mode than in the normal mode; therefore, the effect of tube length variation on the signal intensity was not appreciable with the normal laser (see Figure 4.10). According to them, the difference between the amount of the ablated material in Q-Switched laser ($\sim 1 \mu\text{g}$) and normal laser ($\sim 30 \mu\text{g}$) was the main reason for the signal intensity variation.

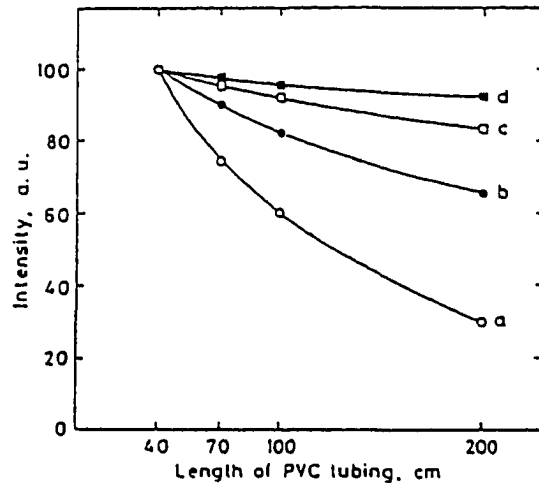


Figure 4.10: Effect of length of PVC tubing on the emission intensity of Mn (0.27%) in steel. (a) peak height and (b) peak area obtained by the Q-Switch laser; (c) peak height and (d) peak area obtained by the normal laser. Reference [19].

Arrowsmith and Hughes [6] used Mo particles ($\rho=10.2 \text{ g/cm}^3$) to predict the effect of particle size and tube length on the efficiency the transfer tube. They reported a more than 80% transport efficiency for particles in the range of $0.005\text{--}2 \mu\text{m}$ diameter (Figure 4.11). They suggested using the shortest, narrowest tube possible in order to increase the transfer efficiency of the transfer line.

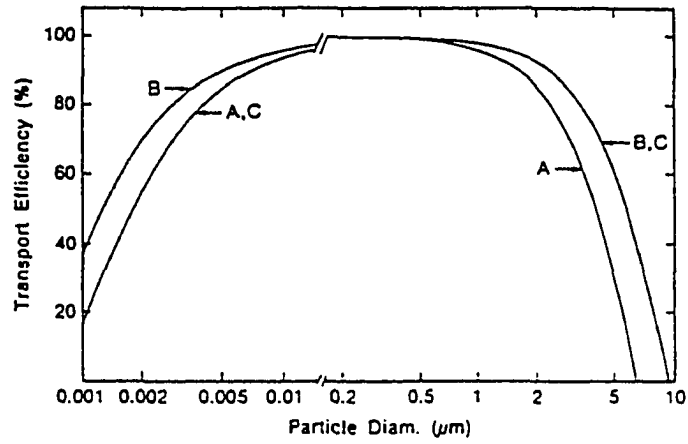


Figure 4.11: Calculated transport efficiency of Mo particles. (A) 1.5 l/min, 4.5 mm i.d, 80 cm; (B) 1.5 l/min, 4.5 mm, 40 cm and 3.0 l/min, 4.5 mm, 80 cm; (C) 1.5 l/min, 2.25 mm, 80 cm. Reference [6].

CHAPTER 5. THEORY AND MODELING

The basic theories relevant to the movement of particles of different sizes in gaseous media are briefly discussed. Different forces acting on the ablated particles due to their motion in the ablation cell and transfer line are calculated. Based on the experimental results and basic theories, the movement of entrained ablated particles inside the ablation cell and transfer line is mathematically modeled.

5.1 Theory

In this section, the theory of the particle's motion in a medium and the different forces acting on a moving particle at various particle size regions are briefly explained.

5.1.1 Forces Acting on the Particles

There are three types of forces that can act in any and all combinations on small particles moving inside a medium: (1) external (body) forces, (2) resistance (drag) forces of medium, and (3) interaction (collision) forces between particles in a medium. These forces are briefly explained in the following sections:

5.1.1.1 External (Body) Force

These forces act on a particle due to the existence of external forces and affect the overall particle mass and its movement in the medium. The basic external forces are:

Gravitational Force: The force acting on the particles due to the gravity is called the gravitational force and its magnitude is given by the following equation:

$$F_g = mg \quad (5.1)$$

For a spherical particle with diameter of d and density of ρ_p , this becomes

$$F_g = \frac{1}{6} \pi d^3 \rho_p g \quad (5.2)$$

Electrical Force: The external electric field acts as field of force on the charged particles and exerts a force on each individual particle which is proportional to the charge of the particle (q) and the electric field strength vector (E)[27]:

$$\vec{F}_e = q \vec{E} \quad (5.3)$$

where

F_e = Electrical force

E = Electric field strength

q = Particle charge

Magnetic Force: A charged particle with no intrinsic magnetic properties moving in a gas with constant velocity (V) through a magnetic field (H), will be acted on by a magnetic force (F_L). The magnitude of this magnetic force is calculated by the following equation [28]:

$$\vec{F}_L = q_p \vec{V} \frac{\vec{H}}{C} \quad (5.4)$$

where

q_p = Particle charge

$C = 3 \times 10^{10}$ cm/sec

Thermal Force: Thermal gradients in a gaseous or liquid medium creates a convective motion. The motion of the medium applies a force on the suspended particles in that medium and moves the particles.

Acoustic Force: In a confined system, acoustic resonance and reflection can result in standing waves. Stagnant gas molecules trapped in a standing wave will develop a circulatory pattern of motion from node to antinode. The moving molecules impact on the particles suspended in the gas and the net resultant force on each particle is called the acoustic force.

Electrostatic force: The electrostatic forces are the result of inducing positive or negative charges on a neutral particle. Particles can receive an electrostatic charge by one or more of these basic procedures: (a) during particle generation, (b) subsequent contact and release of particles from charged surface, and (c) gaseous ion diffusion.

5.1.1.2 Resistance of Medium (Drag Force)

Forces acting on a moving particle due to the medium surrounding it is called drag resistance forces. They have a significant effect on the particle movement in the medium. There are two basic types of resistance forces :

Drag Force: Drag force is the resistance force of the medium to the motion of the particle. The drag force is sum of three different forces which are as the following:

1- Deformation or Viscosity Drag: This is the force necessary to deform the medium so that the particle can pass through. At low particle Reynolds numbers ($Re_p < 0.5$), the viscosity drag force is the predominate force and it is calculated by the following equation:

$$F_{D1} = \pi \mu_g d (V_g - V_p) \quad (5.5)$$

2- Friction Resistance: This force occurs at the surface of the body and it is given by:

$$F_{D2} = 2 \pi \mu_g d (V_g - V_p) \quad (5.6)$$

The total drag force at low particle Reynolds number (Re_p) is the sum of these two forces, therefore

$$F_D = 3 \pi \mu_g d (V_g - V_p) \quad (5.7)$$

3- Pressure Drag: This force represents compression of the medium by moving particle. The friction resistance and pressure drag forces are called skin friction forces and are predominate at high Reynolds numbers.

Buoyant Force: This is the force exerted by a medium on the body suspended in that medium. It is equal to the displaced mass of fluid times gravitational acceleration. For a spherical particle with diameter d , this force is given as

$$F_g = \frac{1}{6} \pi d^3 \rho_g g \quad (5.8)$$

5.1.1.3 Interaction Forces

These forces are significant in high density flow with very small size particles. When the particle diameter in the medium approaches the gas molecule diameter ($0.0005 \mu\text{m}$), the interaction forces become dominant forces and have a significant effect on the particle behavior in the aerosol. For example, the diffusional velocity of a $0.001 \mu\text{m}$ diameter particle in air at standard conditions is nearly 4000 times greater than the terminal free-fall velocity of the same particle due to the gravity forces. The interaction forces are grouped and explained in the following sections.

Phoretic forces: Phoretic or radiometric forces act on particles by an indirect mechanism such as gas molecules interaction with particles. These molecules transfer the energy of the heat, light and molecular concentration to the particles adjacent to them. These forces are very weak and are only significant for very fine particles. There are three different phoretic forces [28]:

1- Diffusiophoresis Force: These forces are the result of non-uniformities in the suspending gas composition. The concentration gradients cause the molecules to attempt and maintain a uniform distribution in the gaseous medium. The impaction of these molecules on the particles, creates a force on each particle. The net result of these forces due to the difference in molecular impact on the opposite sides of the particles are called diffusiophoresis force.

2- Thermophoresis Force: A temperature gradient can create forces on the individual particles resulting in motion of these particles from a hot region toward a colder region. Due to the temperature gradient, gas molecules impinge on each particle from opposite sides with different mean velocities. The net force according to Waldmann [29] is given by

$$F_T \cong -\frac{P\lambda d^2}{T} \nabla T \quad (5.9)$$

where

F_T = Thermophoresis force

P = pressure

λ = mean free path of gas molecule

d = particle diameter

T = temperature

∇T = temperature gradient

3- Photophoresis Force: The motion of aerosol particles illuminated by a light source from one side, photophoresis, is a special case of thermophoresis. The uneven absorption of the light energy by the particle results in uneven heating of the adjacent gas molecules. The velocity gradient of these molecules creates a force on the particle and moves it in different directions.

Diffusion Force: Particles which are not under the influence of external forces, diffuse in a random fashion called Brownian motion. When the particles are uniformly dispersed in a gas, brownian motion will change the position of the individual particles but will not change the overall particle distribution. But, when the particles are not uniformly dispersed, brownian motion tends to produce a uniform concentration throughout the gas. During particle diffusion, the particles move away from high concentration to regions of low concentration. Diffusion forces can result from: velocity, concentration, pressure, and temperature gradients in a medium.

Adsorption Force: The tendency of attraction of gas molecules by the surface of a solid or liquid particle is called adsorption. Adsorption forces are the resulting forces from impaction of gas molecule movement on the particle due to the attraction of gas molecules by the particle surface.

5.1.2 Aerosol Dynamic

In aerosol science, different sets of mathematical relationships are developed to study the particle's dynamics for all sizes of particles and under all conditions. Thus, a knowledge of the particle size regions is prerequisite for correctly applying these equations when investigating the particle motion. In the following sections the particle size regions are defined and proper equations for calculating the resistance (drag) forces, settling velocities, and stop distance of the ablated particles are given.

5.1.2.1 Particle Size Regions

According to Hesketh [28], there are four separate size regions for fine particles in gaseous media near standard conditions. These regions as shown in Figure 5.1, ranging from small to large particles are: (a) Free Molecule (Kinetic), (b) Transition, (c) Slip Flow (Cunningham), and (d) Continuum (Stokes).

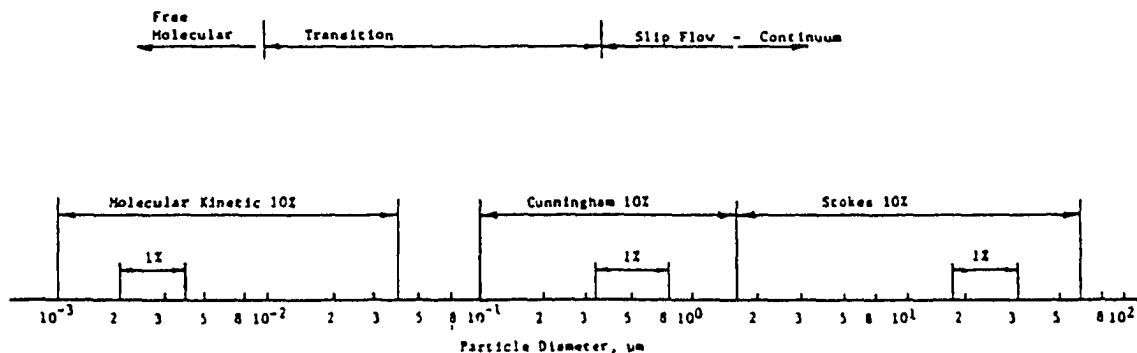


Figure 5.1: Particle size regions.

Free Molecular: In this region, particles are small compared to the gas mean free molecular path ($d \leq \lambda$) and there are few intermolecular particle-gas collisions. This region includes the particles with diameter of less than 0.01 μm . The diffusional velocity of the particles in this region is significantly higher than the gravitational settling velocity.

Transition: The particle diameters range in the transition region is between 0.01 and 0.1 μm . There is no generally acceptable procedure to analytically describe the particle transport process in this region.

Slip Flow: In this region, the resistance force of the gaseous medium is less than the continuum region and due to their small size, particles appear to slip through the gas molecules. The particle diameter in the slip flow region is between 0.1 and 0.8 μm .

Continuum: Because of relatively large particle diameters, the gaseous medium acts more as a continuum to the particles. Particles with diameters between 0.8 and 35 μm are included in this region.

5.1.2.2 Resistance of the Medium in Different Regions

In this section, the rectilinear steady state motion (constant velocity) of aerosol particles are discussed. The nature of the resistance (friction) forces of the medium on the moving particles, in different particle size regions, are explained and the proper equations for calculating them are given.

Molecular Kinetics In this region, the motion of the particles is molecular and it does not disturb the Maxwellian-Boltzmann velocity distribution of the gas molecules. This means that the particle motion in the medium creates no currents in gas. The gas resistance force in this region is given by [30]

$$F_D = -\frac{3\pi\mu_k d^2 V_p}{2(A+Q)\lambda} \quad (5.10)$$

where

F_D = resistance force of the medium

λ = mean free path of gas molecules

μ_g = viscosity of gas

d = particle diameter

V_p = particle velocity

$(A + Q) = 1.175$ for specular reflection

$(A + Q) = 1.091$ for diffuse reflection (conservation of absolute incident velocity)

$(A + Q) = 1.131$ for diffuse reflection (velocity distribution)

Cunningham (Slip Flow) In the kinetic theory of gases, it is assumed that there is no discontinuity. Cunningham [31], proposed the following equation for calculating the resistance force when there is a discontinuity in the tangential velocity at the surface of a particle (slip).

$$F_D = -\frac{3\pi\mu_g d V_p}{C_c} \quad (5.11)$$

The Cunningham correction factor (C_c) is given as:

$$C_c = 1 + \frac{2\lambda}{d} \left[A + Q \exp\left(-\frac{bd}{2\lambda}\right) \right] \quad (5.12)$$

where

$$A = 1.252$$

$$Q = 0.399$$

$$b = 1.100$$

Stokes (Continuum) In this region, the resistance is proportional to the diameter and the motion of the particles is of a hydrodynamic nature. The isotropic character of the velocity distribution of the molecule is destroyed and a bulk flow is created. The resistance forces of a medium are given by the Stokes and Oseen equations. In the Stokes equation (5.13), the inertia terms are omitted from the equations of motion; therefore, the resistance forces are expected to be less than the actual force [27].

I- Stokes ($0.01 < Re < 0.1$)

$$F_D = -3 \pi \mu_g d V_p \quad (5.13)$$

At high Reynolds numbers, the increasing effect of inertia forces results in a higher resistance of medium. At $Re = 0.5$ the resistance forces calculated by the Stoke's law is 5 percent less than the actual value. Oseen's equation (5.14) gives better estimate of the resistance of the medium by partial consideration of inertia forces [32].

II- Oseen ($0.1 < Re < 0.5$)

$$F_D = -3 \pi \mu_g d V_p \left(1 + \frac{3}{16} Re \right) \quad (5.14)$$

Beyond Stokes Region ($3 < Re_p < 400$) In contrast to viscous motion, where the resistance is proportional to the velocity of the particle, in the region of large Reynold's number, the resistance forces are a function of V^n . In this region the inertia forces cannot be neglected and steadily increases with Reynold's number [27].

$$F_D = -\frac{1}{8} C_D \pi \rho_g d^2 V_p^2 \quad (5.15)$$

Equations for calculating the drag coefficient (C_D) at different particle Reynolds numbers are:

for $Re_p < 1$

$$C_D = 24/Re_p$$

for $1 < Re_p < 1000$

$$C_D = 24/Re_p (1 + 0.15 Re_p^{0.687})$$

$$C_D = 24/Re_p + 4 / Re_p^{0.33} \quad (5.16)$$

for $1000 < Re_p < 2 \times 10^5$

$$C_D = 0.44$$

for $Re_p > 2 \times 10^5$

$$C_D = 0.10$$

Table 5.1: The regions of application of the equations for calculating F_D

Formula	Permissible Error	
	1%	10%
Molecular Kinetic	0.002 < r < 0.004 μm	0.001 < r < 0.04 μm
Cunningham (Slip Flow)	0.36 < r < 0.8 μm	0.1 < r < 1.3 μm
Stokes (Continuum)	16 < r < 30 μm	1.3 < r < 60 μm

The regions of applicability of various formulae for the resistance of a medium is calculated by Fuchs [32] and is given in Table 5.1.

5.1.2.3 Non-Uniform Rectilinear Motion of Aerosol Particles

The major forces acting on a spherical particle moving with an initial upward velocity (V) in a straight line through a resisting medium is shown in Figure 5.2. There are two opposite resistance forces acting on this particle: (a) Drag force F_D , and (b) Buoyant force F_B . Also, there is a gravity force acting on this particle F_g in the same direction of the drag force. Newton's second law of motion states that sum of the forces acting on a body is equal to the rate of change of momentum. Thus:

$$m \frac{dV}{dt} = \vec{F}_1 + \vec{F}_2 + \vec{F}_3 + \vec{F}_4 + \dots \quad (5.17)$$

in this case it is expressed as

$$m \frac{dV}{dt} = \vec{F}_g - \vec{F}_B + \vec{F}_D \quad (5.18)$$

for rectilinear motion of a spherical particle this becomes:

$$m \frac{dV}{dt} = m g - \frac{1}{16} \pi d^3 \rho_g g + 3 \pi \mu_g d_p (V_g - V_p) \quad (5.19)$$

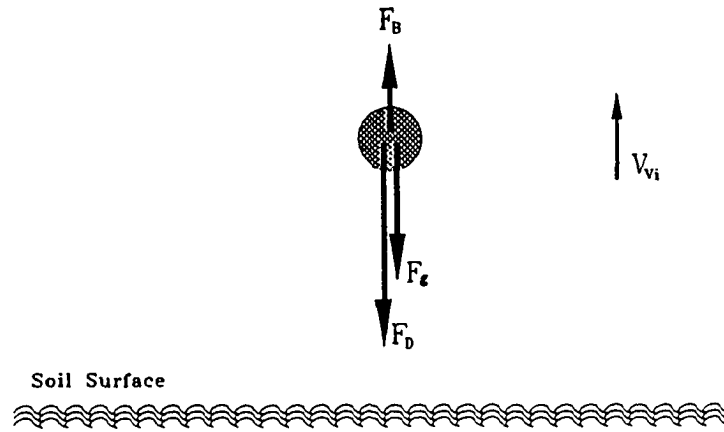


Figure 5.2: Forces acting on a particle inside the ablation cell.

Where

V_p = particle velocity

V_g = gas velocity

μ_g = gas viscosity

ρ_g = gas density

d_p = particle diameter

m = particle mass

ρ_p = Particle density

By neglecting the gas velocity, which is very small compared to the initial velocity of the particle, and the buoyant force which is negligible in the gaseous medium, the equation 5.19 can be simplified as:

$$\frac{dV}{dt} + \frac{V}{\tau} - g = 0 \quad (5.20)$$

where (τ), the relaxation time (time constant) of the particle, which is a very important parameter in mechanics of aerosols, is given as:

$$\tau = \frac{d^2 \rho_p}{18 \mu_g} \quad (5.21)$$

Solving the above first-order linear differential equation gives the velocity of particles in Stokes region. The distance traveled by the particle is obtained by integrating the velocity equation.

$$\begin{aligned} V &= V_i e^{-t/\tau} \\ X &= V_i \tau (1 - e^{-t/\tau}) \end{aligned} \quad (5.22)$$

The velocity and stop distance for particles at Cunningham region ($3 \times 10^{-7} < Re_p < 0.01$) are calculated by the following sets of equations:

$$\begin{aligned} V &= V_i e^{-t/\tau C_c} \\ X &= V_i \tau (1 - e^{-t/\tau C_c}) \end{aligned} \quad (5.23)$$

In the absence of an external force, the stop distance of the particle with high Reynolds number ($1 < Re_p < 1000$) can be calculated by using equation 5.24 when $Re_f = 0$ [32].

$$X_s = \frac{4 \rho_p d}{3 \rho_g} \int_{Re_i}^{Re_f} \frac{dRe}{C_D Re} \quad (5.24)$$

The equation for finding the stop distance when the gravity force is not neglected is

$$X_s = \frac{4 \rho_p d}{3 \rho_g} \int_{Re_i}^{Re_f} \frac{dRe}{C_1 - C_D Re^2} \quad (5.25)$$

where

$$Re_f = 0$$

$$C_1 = \frac{4}{3} g \rho_p \rho_g d^3 / \mu_g^2$$

5.2 Mathematical Modeling

In this section, the particle entrainment inside the ablation cell and aerosol motion in the transfer line are mathematically modeled. Then, these models are used to theoretically predict the ablation cell entrainment and transfer line transportation efficiency at different argon gas flow rates.

5.2.1 Assumptions

In order to simplify the study of the ablated particle's behavior inside the ablation cell and through the transfer line, certain assumptions regarding the gas flow behavior and particle characteristics in the aerosol are made. All these assumption are based on the results of the preliminary flow study inside the Plexiglass cell models and the Scanning Electronic Microscope (SEM) photographs obtained during the particle size analysis study.

5.2.1.1 Ablated Particles

Based on the results from the SEM photographs of the ablated particles, the following assumptions are made regarding the characteristics of the ablated particles.

- 1- The shape of the ablated particles as shown in the SEM photographs (Figure 5.3), are irregular with the aspect ratio (the ratio of minimum diameter to maximum diameter) ranging from 0.5 to 1.0. For very small particles ($<1 \mu\text{m}$), this ratio is very close to 1. Therefore, all particles are assumed to have a radius equal to the radius of the projected circle.
- 2- The ablated particles have different diameters and shapes, therefore they are polydisperse and non-isometric.
- 3- The results from the Energy Dispersive X-ray (EDX) analysis, which was performed during the SEM analysis, shows that the main constituent of most particles is silicon. Thus, the density of ablated particles are assumed to be 2.65 g/cm^3 which is equal to the density of the silicon oxide.
- 4- It is assumed that particles are rigid.

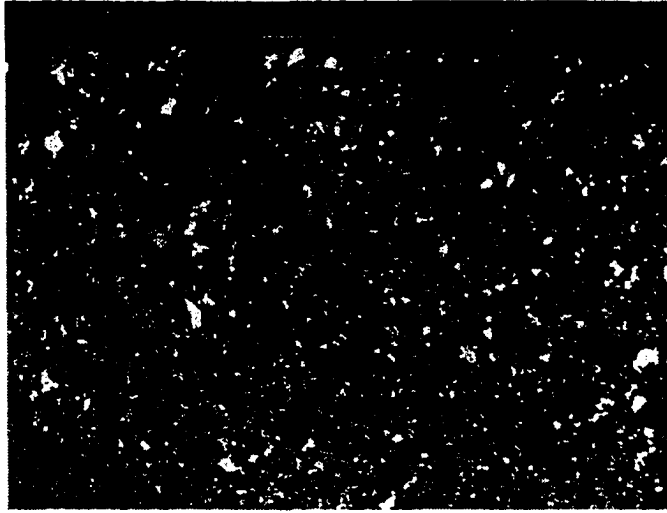


Figure 5.3: SEM photograph of ablated soil particles (NRM5).

5- Since the particle concentration in the aerosol is relatively low, the interaction between the particles inside the ablation cell and transfer line are not significant and the coalescence of the particles is negligible .

5.2.1.2 Gas Flow

The following assumptions are made regarding the characteristics of the argon gas inside the cell and transfer line (tube):

- 1- Argon gas is a compressible gas, but in this study since the gas velocity is well below the acoustic velocities (i.e., $Ma \ll 1$) and it is assumed that this gas is incompressible.
- 2- The argon density is constant.
- 3- For particle diameter larger than $0.01 \mu\text{m}$, argon gas is a continuous medium.
- 4- To neglect the ablation cell wall effect on the particle motion, it is assumed that there is infinite medium inside the cell.
- 5- For the inlet gas flow rate between 0.8 to 1.2 l/min, the Reynolds number of the aerosol in the transfer tube with 4.7 mm inside diameter is between 236 to 354. Thus, the aerosol behavior in the transfer tube was assumed to be laminar flow.

5.2.2 Surface Ablation Cell

Due to the high initial velocity, the ablated particles inside the surface ablation cell have high Reynolds numbers and their motion is turbulent. After a very short period of time (fraction of second) they lose their initial velocities and they become laminar. Therefore, in order to properly model the particle entrainment inside the cell, its volume is divided into two distinct regions (see Figure 5.4): 1- region A with a turbulent particle motion, and 2- region B with a laminar aerosol flow.

Region A: In this region, which is in the immediate vicinity of the soil surface, the motion of the ablated particles is turbulent in nature. In order to estimate the height of this region, a knowledge of the initial velocity (V_i) and stopping distance of particles (X_s) is required. Stopping distance of a particle is the distance a particle projected into still air, with an initial velocity V_i in Y direction, travels until it stops.

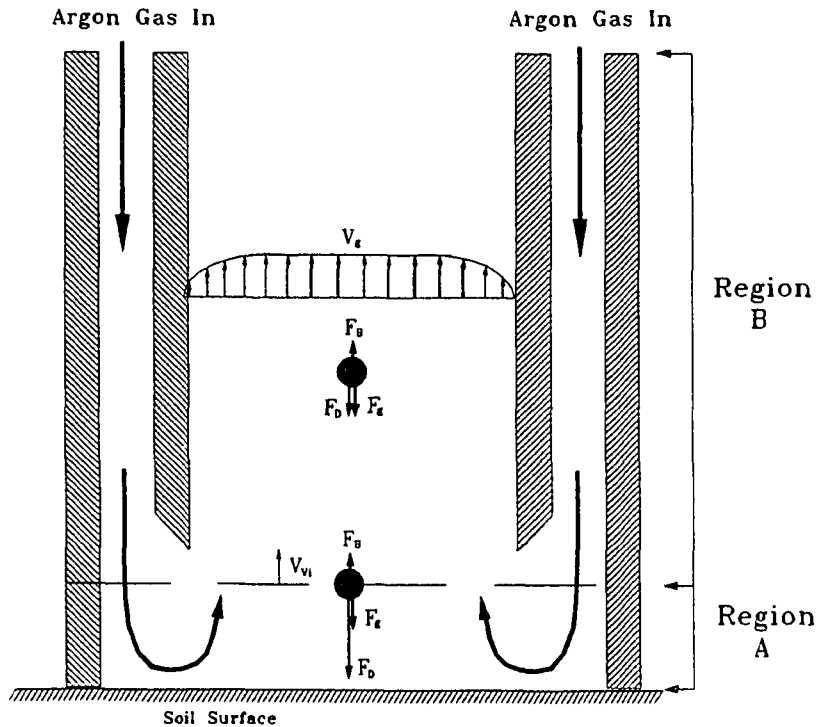


Figure 5.4: Aerosol flow regions inside the surface ablation cell.

Due to the ablation process (which involves melting, vaporization, and spallation), ablated particles have very high initial velocities with different directions when they are ejected into the argon gas stream inside the cell. The particle initial velocity is a function of different parameters such as: laser power density, laser beam wavelength, laser pulse duration, atomic mass number of the ablated element, and characteristics of the sample being ablated. The initial velocity of the generated ions during an ablation process from a solid sample is given by the following equation [11].

$$C_s = 1.37 \times 10^6 \left(\frac{A^{\frac{1}{3}}}{\Psi^{\frac{1}{16}}} \right) (P \lambda \sqrt{\tau})^{\frac{1}{4}} \quad (5.26)$$

where

A = atomic mass number

$\Psi \approx 1$

P = laser power density

λ = laser wavelength

τ = laser pulse duration

During this study, a Q-switched Nd-YAG laser beam with the following specification was used to ablate the soil samples:

$P = 1.5 \times 10^8$ watts/cm²

$\lambda = 532$ nm

$\tau = 7$ ns

The initial ejection velocities of ions of U, Th, Si, Fe, and Al generated during ablation process inside the cell are calculated by using the above equation and laser specification.

$C_U = 2.46 \times 10^6$ cm/sec

$C_{Th} = 2.45 \times 10^6$ cm/sec

$C_{Si} = 1.88 \times 10^6$ cm/sec

$C_{Fe} = 2.05 \times 10^6$ cm/sec

$C_{Al} = 1.88 \times 10^6$ cm/sec

Because of the high mass, the initial velocities of the ablated particles (depending on their sizes) are expected to be significantly less than these calculated values. Also, the air pockets trapped between the soil particles could result in a lower initial velocity of a particle generated from soil sample compared to the same size particles generated from solid sample. By considering the above factors and the results from the high speed photography of the ablation process, the range of the initial velocities of the ablated particles is estimated to be between 1,000 - 10,000 cm/sec. The Reynold's number of particles with diameter between 0.01 to 30 μm with initial velocities between 1,000 - 10,000 are between 0.01- 241 (see Appendix A).

In order to calculate the stopping distance of the different sized particles, a proper set of equations for each particle size region must be used. Using equations 5.22-25, the stopping distance of the selected range of particles in the vertical direction are calculated and tabulated in Appendix C. The minimum stopping distance (0.22 μm) belongs to a particle with 0.01 μm diameter and 1,000 cm/sec initial velocity. The maximum stopping distance is about 13 cm for a particle with 20 μm diameter and 10,000 cm/sec initial velocity. According to Carmen and Yeung [4], the height of this region for different elements (Al, Cu, Mo) vary between 5 to 10 mm. Therefore, by considering the fact that most of the particles are not projected in the vertical (Y) direction, it could be assumed that the majority of the particles will dissipate their initial velocity by the time they reach a height of 10 mm above the soil surface. Thus, the particle motion can be assumed to be laminar from 10 mm above the soil surface until it exits the cell.

Region B: The argon gas flow inside the cell in this region is very uniform and has an upward constant velocity. Most of the ablated particles have dissipated their initial velocity by the time they reach this region. The Reynolds number for the argon gas flow in this region is given by the following equation:

$$Re_g = \frac{V_g d}{\nu_g} \quad (5.27)$$

where

Re_g = Reynold's number of gas

V_g = gas velocity

d = cell diameter

ν_g = kinematic viscosity of gas

The Reynolds number of the argon gas with inlet flow rate of 1 l/min is calculated as:

$$V_g = (1000 \text{ cm}^3/\text{min} \times 1 \text{ min}/60 \text{ sec}) / (\pi \times 2.54^2 \text{ cm}^2) = 0.82 \text{ cm/sec}$$

$$\text{Re}_g = (0.82 \times 5.0) / (0.151) = 27.7$$

which is very low and therefore the flow is laminar in this region.

In order for a particle to be entrained in this laminar gas flow with an upward velocity of V_g , the settling velocity of this particle (V_s) must be less than the gas flow velocity ($V_s < V_g$). Otherwise, the particle will deposit inside the cell due to the gravity force. Thus, by calculating the settling velocities of the particles with different diameters and comparing them with the argon gas flow inside the cell, it is possible to predict the upper limit size of the particles which could be entrained in the gas flow. Also, the efficiency of the cell entrainment could be calculated if enough information about the rate of ablated particles and their size distribution were available.

The settling velocities of different size particles (0.01 - 30 μm) are calculated by using equations 5.22-25 (see Appendix A). The maximum particle size, with a density of 2.65 g/cm^3 , that can be entrained inside the ablation cell with an inlet gas flow of 1 l/min is about 11 μm in diameter. Therefore, it is possible to control the amount and size of the entrained particles simply by varying the gas flow speed inside the cell. This could be accomplished either by adjusting the inlet gas flow rate or changing the ablation cell diameter. The argon gas flow speed could be lowered by a factor of 4, simply by doubling the cell diameter. This will lower the size of the maximum particle diameter entrained in the aerosol to about 5 μm . The maximum diameter of the entrained particles, (d_p), can be calculated by

$$d_p \leq \frac{8.5}{D_c} \sqrt{\frac{Q \mu_g}{\pi g \rho_p}} \quad (5.28)$$

where

D_c = cell diameter

Q = inlet gas flow rate

μ_g = gas viscosity

ρ_p = particle density

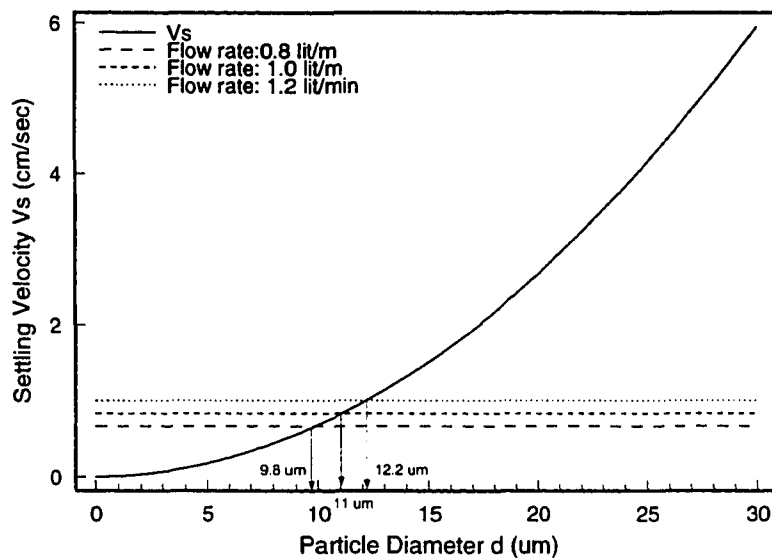


Figure 5.5: Settling velocity of the ablated particles with $\rho = 2.65 \text{ g/cm}^3$.

The settling velocities of particles between 0.01 - 30 μm and the upper limit size of the entrained particle are shown in Figure 5.5.

5.2.3 Transfer Line

The transfer tube is another important component of solid-sample collection system used during the ICP-AES/MS analysis. The length and diameter of transfer tube are two important parameters that have a significant effect on the amount of particles transferred to the ICP. In a laminar flow, the particle deposition inside tube is mainly governed by convective diffusion and settling due to the gravity.

Convective diffusion is a very important mechanism of small particle deposition inside the transfer tube. By assuming laminar flow and steady state conditions inside the tube, it is possible to calculate the convective diffusion settling rate of the particles in aerosol on the tube wall. Since the velocity of the aerosol inside tube near the wall is very close to the zero, there is a velocity gradient inside the transfer tube. This velocity gradient results in fine particle settling on the tube walls due to the convective diffusion. The final to original concentration

ratio (C_{out}/C_{in}), of particles in a long tube with laminar gas flow can be calculated by [27]

$$\frac{C_{out}}{C_{in}} = 1 - \frac{4}{\sqrt{\pi}} \sqrt{\frac{DL}{Ur^2}} \quad (5.29)$$

and

$$D = kT \frac{C_c}{3\pi\mu d} \quad (5.30)$$

where

D = diffusion coefficient

k = Boltzmann constant (1.38×10^{-16} erg/K)

T = absolute temperature (K)

C_c = Cunningham correction factor

L = tube length

U = aerosol velocity inside the tube

r = tube radius

Settling of the large particle due to gravity, during the aerosol transfer in a long tube, is another important deposition mechanism. The fraction of any specific size particle, (C_{out}/C_{in}), that will settle out of the gas during the particle transportation in a tube due to the gravity is given as [33]

$$\frac{C_{out}}{C_{in}} = \frac{2}{\pi} \left(2C_2 \sqrt{1 - C_2^{2/3}} + \sin^{-1} C_2^{1/3} - C_2 \sqrt[3]{1 - C_2^{2/3}} \right) \quad (5.31)$$

where

$$C_2 = \frac{3V_S L}{8RU}$$

V_S = settling velocity

L = tube length

U = aerosol velocity inside the tube

R = tube radius

The critical length to allow all the particles of a given size to settle by gravity from the tube is

$$L_{cr} = \frac{8R\bar{U}}{3V_S} \quad (5.32)$$

Thus, it is possible to mathematically predict the lower and upper limits of the particle sizes that can migrate through a specific tube length and diameter during the aerosol transportation process. By using equations 5.29 and 5.32, the transportation efficiency of a 100-foot long Tygon tube with inside diameter of 4.2 mm can be calculated (see appendix B). As shown in Figure 5.6, the particles with diameter of less than 0.02 μm will settle inside the tube due to the convective diffusion. On the other hand, particles with diameter larger than 2 μm will deposit in the tube due to the gravity force (see Figure 5.7). Therefore, the range of transferred particles for the 100-foot tube is between 0.02 - 2 μm for 0.8 - 1.2 lit/min aerosol flow rates. By knowing the range of the particle sizes in the aerosol entering the tube after the ablation cell, the transportation efficiency of the tube could be calculated.

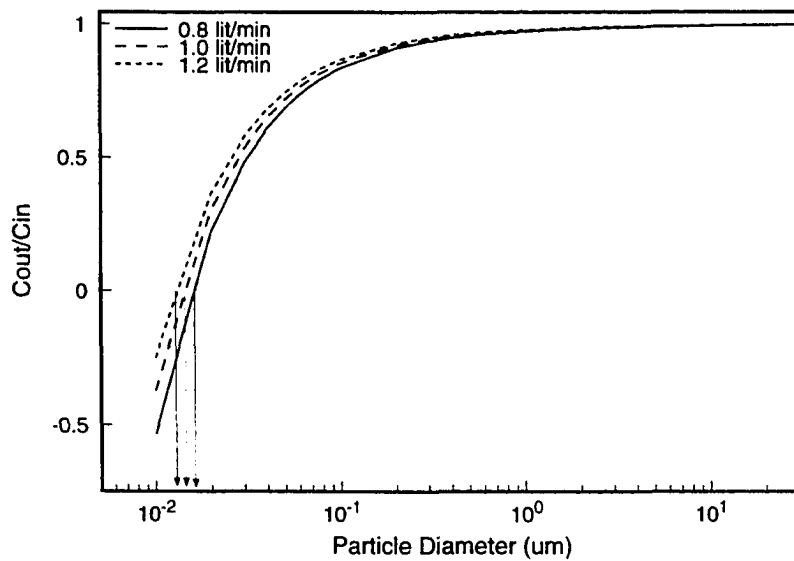


Figure 5.6: Particle deposition in a 100-foot long tube due to the convective diffusion.

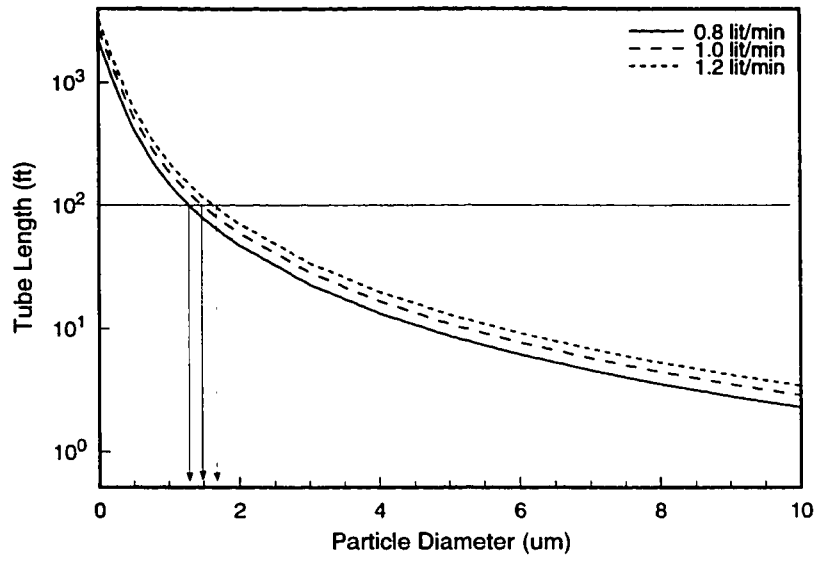


Figure 5.7: Particle deposition in a 100-foot long tube due to the gravity force.

CHAPTER 6. CELL DESIGN

For solid sample introduction to the ICP-AES/MS using laser ablation, several different types of ablation cell designs were suggested by different groups of the researchers using these techniques. These cells were generally small and designed to handle a small amount of sample in either solid or powder form in a highly controlled laboratory environment. Most of the cells were made from glass or aluminum. This makes the cells virtually unusable for field application of soil sampling since field sampling requires a relatively large and sturdy ablation cell capable of handling multidirectional loads and harsh environmental conditions.

Flow interaction with ablated sample particles has a very significant effect on the particle entrainment efficiency of the ablation cell. The researchers in analytical chemistry who used ablation cells for solid sample collection utilizing laser ablation, have paid little or no attention to this important aspect. Therefore, no published study was available regarding flow interaction with ablated particles prior to this work.

In this study two different ablation cells were designed and tested for in situ and real-time surface and sub-surface (up to 100 feet below the surface level) soil sampling. These cells would be part of the field deployable analytical instrument set up (MDLEST) which was designed and built by the TIP group for characterization of the contaminated soil at the DOE sites. In this chapter the basic steps taken for surface and sub-surface ablation cell design process for field application are explained.

6.1 Surface Ablation Cell

The surface ablation cell is a part of the soil sampling probe used in the field to collect very fine particles of contaminated soil for chemical analysis. A laser beam provides the necessary energy to ablate the soil. This cell is attached to the bottom of a robotic end effector (sampling probe) that contains a rastering unit, optics for focusing the laser beam, and sensors for laser power reading and laser beam focusing (Figure 6.1). The end effector is attached to the end of a robot arm used for remote robotic surface sampling. During the sampling process, the robot lowers its arm until the knife edge of the ablation cell touches the soil. By pushing the knife edge of the ablation cell into the soil and spraying water on the soil, a good seal between the ablation cell and soil for argon gas flow during the laser ablation process is achieved.

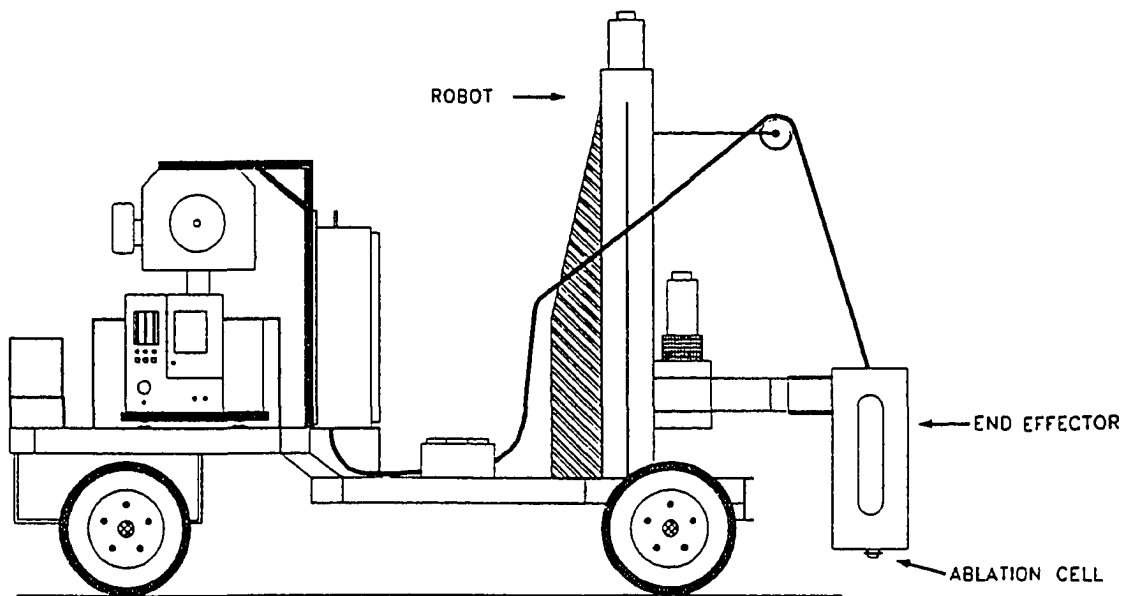


Figure 6.1: Surface remote robotic soil sampling set up.

6.1.1 Design Criteria

The design criteria for the surface ablation cell were selected by considering the factors that affect the overall signal quality and quantity of the analytical methods (LA-ICP-AES/MS) used for soil sampling. The most important criteria in the ablation cell design and enhancing the performance of the analytical unit are:

- 1- High transport efficiency.
- 2- Maximizing the amount of transferred ablated particles with diameters of less than 2-3 μm .
- 3- Flushing time (the time required for the ablated particles to exit the ablation cell).
- 4- Minimum signal fluctuation due to the change in the aerosol density in the cell.
- 5- Minimum argon gas leak in the ablation cell during the ablation process.
- 6- Minimum laser power loss due to the scattering of the laser beam by ablated particles inside the cell and particles deposited on the quartz window.
- 7- Resistance to corrosion and other environmental effects.
- 8- Easy assembling and service during field use.

6.1.2 Flow Pattern Study Inside the Cell Using Plexiglas Models

For speeding up the final design selection process and cutting down the design cost, a set of plexiglas (Acrylic) models of ablation cells were used in this study to simulate the argon gas flow pattern inside the cell during the ablation process. Based on the previous work done by Arrowsmith and Hughes [6], seven different closed double wall cylindrical cell models were designed and built using transparent plexiglas materials. These models were used to do a preliminary visual study of flow behavior inside the ablation cell using liquid dye and water as a flow medium. The flow motion of water inside these cells was studied by injecting a liquid dye into the water stream in the inlet line. The ablated particles entrained inside the cell were simulated by injecting a red liquid dye from a very fine hole (0.5 mm diameter) at the center of the cell base into the cell. The flow pattern and the particle entrainment simulation inside the ablation cell was recorded by a high speed camcorder. Transport efficiency, flushing time, and homogeneity of the mixture of dye and flow medium at output ports were three main criteria for

selecting the best cell design.

Cell model no. 1 This cell as shown in Figure 6.2, is a closed cylindrical double wall cell (3 in. inside diameter and 2 in. height) with two input and two output ports. The inner wall was tapered to decrease the effective cell volume and also increase the flow velocity inside the cell. A circular ring orifice with a one inch diameter hole was mounted under the input ports to create a venturi effect and increase the input flow velocity inside the cell such that it diverts the upward motion of the particles and prevents them from reaching to the window. The effective volume of this cell is 100 cm³.

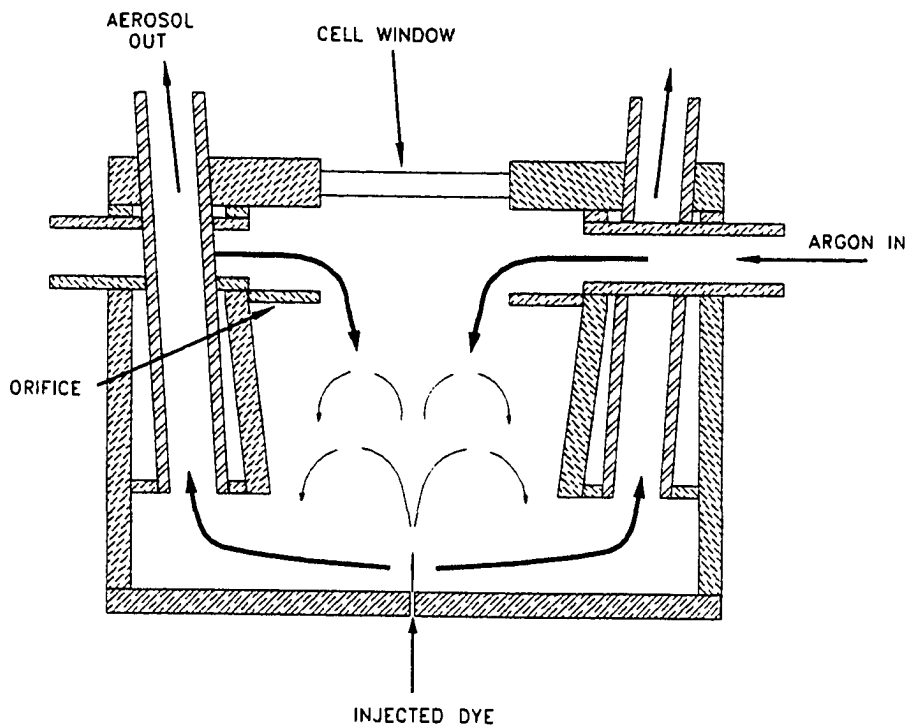


Figure 6.2: Ablation cell model no.1.

In this cell, in order to eliminate possible problems such as attenuation of the laser beam due to deposition of ablated particles on the cell window, flow was introduced into the cell from two side ports. Because of the venturi effect (increased flow velocity), there was little or no contact between the window and the injected dye from the bottom of the cell. Therefore, the probability of particle deposition on the window of this cell design was very low. Due to the turbulence and eddy effects of the flow inside the cell, adequate mixing characteristics were achieved. The flushing time (time required for the red dye to exit the cell completely after one injection) for this cell was between 12-13 seconds. The main disadvantage of this cell model was the high rate of deposition of the ablated particles on the bottom of the cell (low entrainment efficiency) due to the downward motion of the input flow which tends to deposit the particles by impacting them on the bottom of the cell.

Cell model no. 2 This cell, as shown in Figure 6.3, is very similar to the cell no. 1. But, the flow was directed to the base of the cell from two top input ports, and two side ports

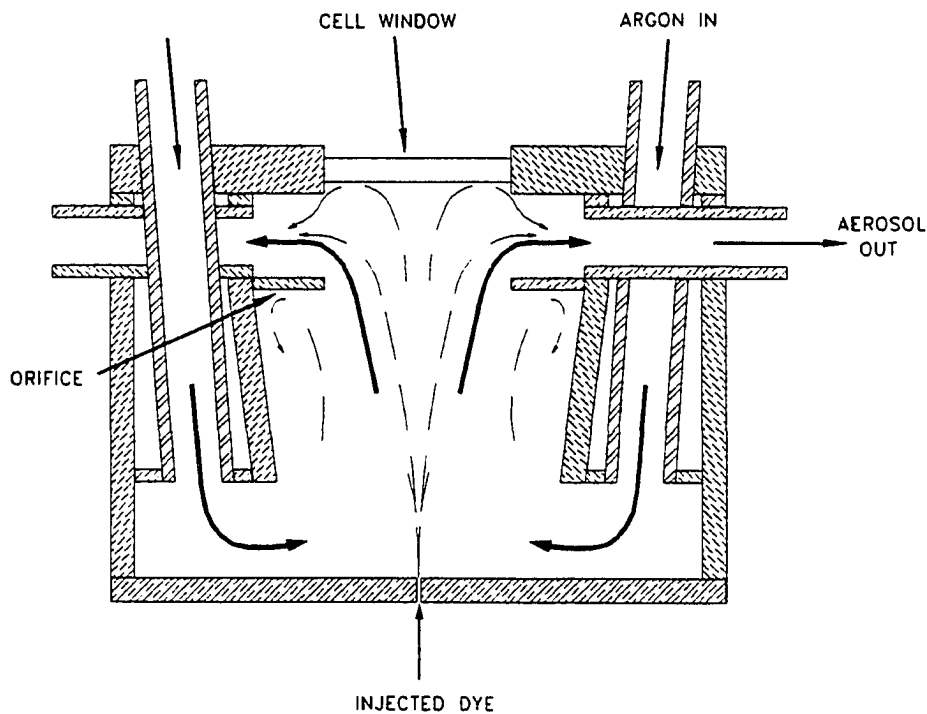


Figure 6.3: Ablation cell model no. 2.

were used to transfer the fluid out of the cell. The upward motion of the inlet fluid inside the cell was very helpful in entrainment of the injected red dye in the cell. The particle deposition on the bottom of the cell was very low due to the same reason. However, there was a significant amount of dye deposition on the top surface of the orifice plate and the window. Because the effective volume of this cell (130 cm³) was larger than the cell no. 1, the flushing time for this cell was increased to 15-17 seconds. The poor mixing characteristics and high deposition rate of particles on the window were two main disadvantages of this cell design.

Cell model no. 3 In this cell, similar to cell model no. 1, the inlet flow was directed into the cell from two side ports (Figure 6.4). But, in order to decrease the particle deposition on the sample surface due to the impaction, the orifice was removed and the height of the cell was also increased by 0.5 inch. The position of the two side ports were also lowered by 0.75 inches in

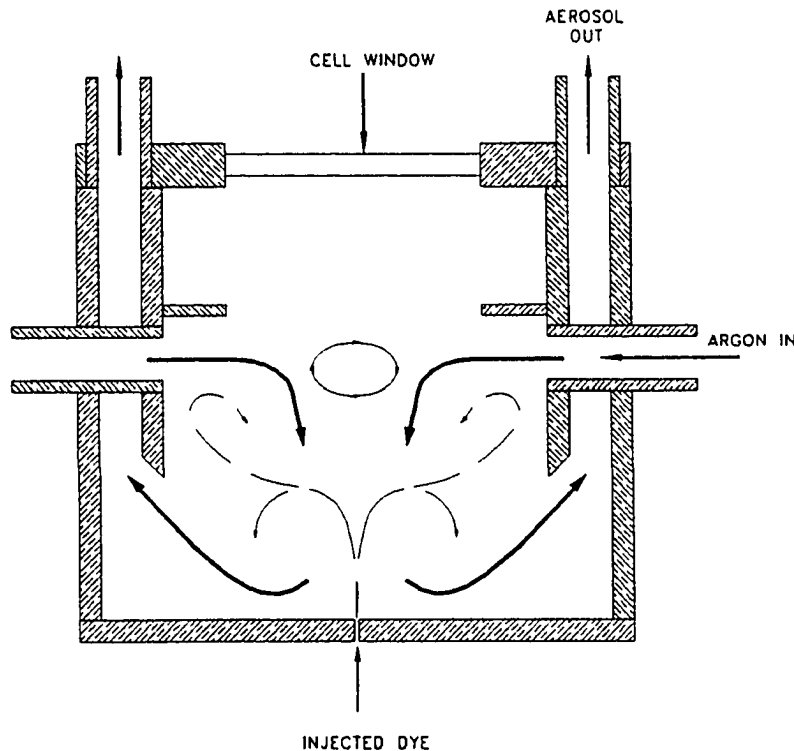


Figure 6.4: Ablation cell model no. 3.

order to be closer to the plume of ablated particles and to decrease the particle deposition rate on the window. The effective volume of this cell was increased to 245 cm³ and the flow rate was 1 liter/min.

The downward motion of the flow inside the cell was very helpful in keeping the cell window clean. But, the mixing characteristics of the cell was very poor and the particle deposition on the bottom of the cell was still high due to the impact action of the incoming flow. Because of the overall increase in the volume of the cell, the flushing time increased to 30-35 seconds.

Cell model no. 4 In order to generate a more homogeneous mixture of fluid and particles inside the cell and also to decrease its effective volume, a flow deflector ring was added to the lower section of the cell model no. 3. The effective volume of this cell was 245 cm³ and the flow rate was 1 l/min (Figure 6.5).

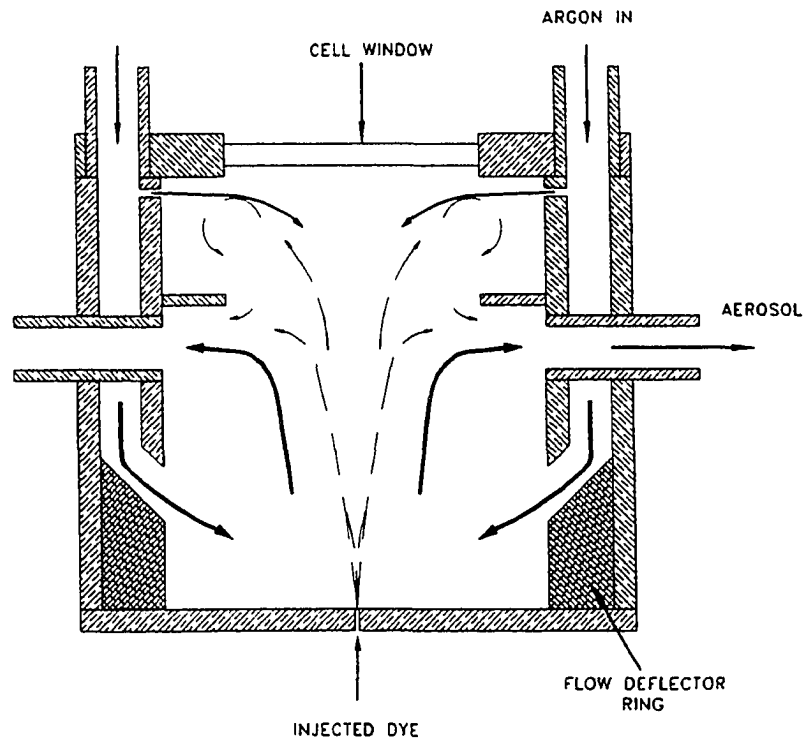


Figure 6.5: Ablation cell model no. 4.

In this model, to prevent particle deposition on the window, four small openings (2x5 mm) were machined on the upper edge of the inner wall of the ablation cell. The inlet flow was introduced from the two upper ports such that a portion of it could flow through these openings and thereby continuously wash the cell window. This flow could decrease the particle deposition on the window. The deflector ring improved the mixing and entrainment characteristics of the cell significantly. The particle deposition on the bottom of the cell was very low but, in spite of decreasing the cell volume, the flushing time of the cell increased to 50-55 sec. The main reason for this time increase was existence of a dead volume above the output ports that had a tendency to retain the red dye in suspension above the outlet ports.

Cell model no. 5 This cell model (Figure 6.6) is the modified version of cell model no. 4. To improve the flushing time, the inside diameter of the cell was decreased from 3.5 to

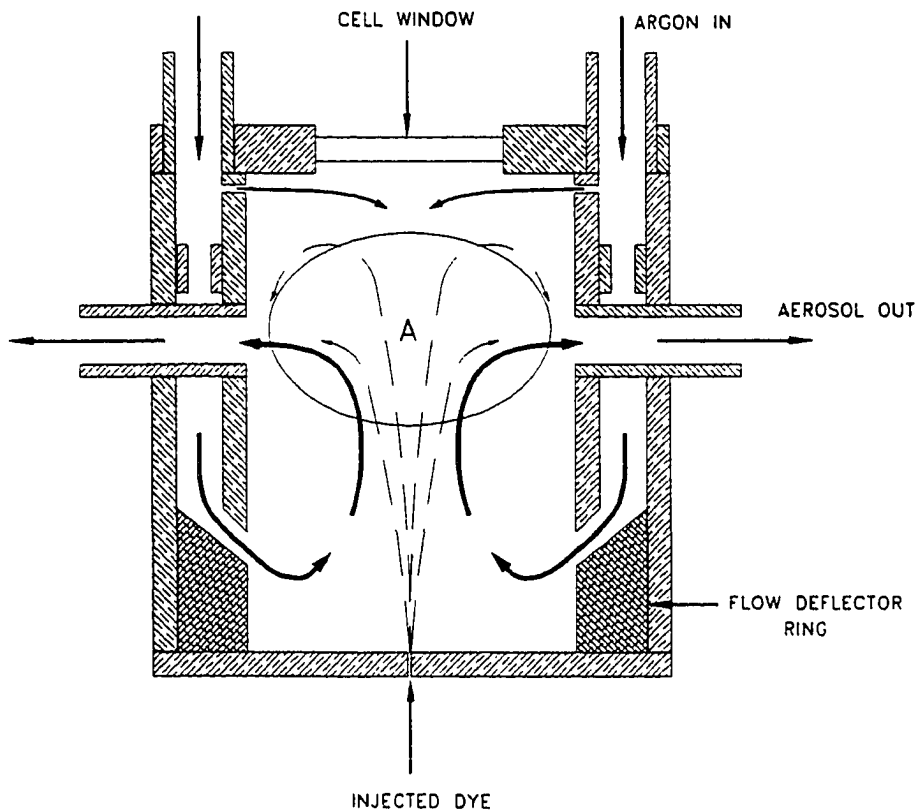


Figure 6.6: Ablation cell model no. 5.

2.5 inches to eliminate the dead volume above the output ports. This modification decreased the effective volume of the cell to 100 cm³. In order to have a more uniform flow to wash the cell window, eight equally spaced small holes (1 mm. diameter) were drilled on the upper edge of the inner wall. This flow pattern tends to keep the window clean and adds more downward flow to the dead volume. A flow restricting ring with four holes (3 mm. diameter) was mounted between the cell walls (about 10 mm below the top of the cell) to increase the inlet flow velocity and also to create back pressure for the flow which cleans the window. Because of turbulent flow and mixing created by the deflector ring, this cell had very reasonable particle entrainment and mixing characteristics. The particle deposition on the bottom of the ablation cell was very low. Due to the continuous flow under the cell window, the contact between the injected dye and this window was minimum. The flushing time of this cell was improved and was between 20 to 22 seconds. Because of the flow pattern inside the cell and flow from eight small holes at the top of the cell, there was a cloud of suspended dye above and between two output ports

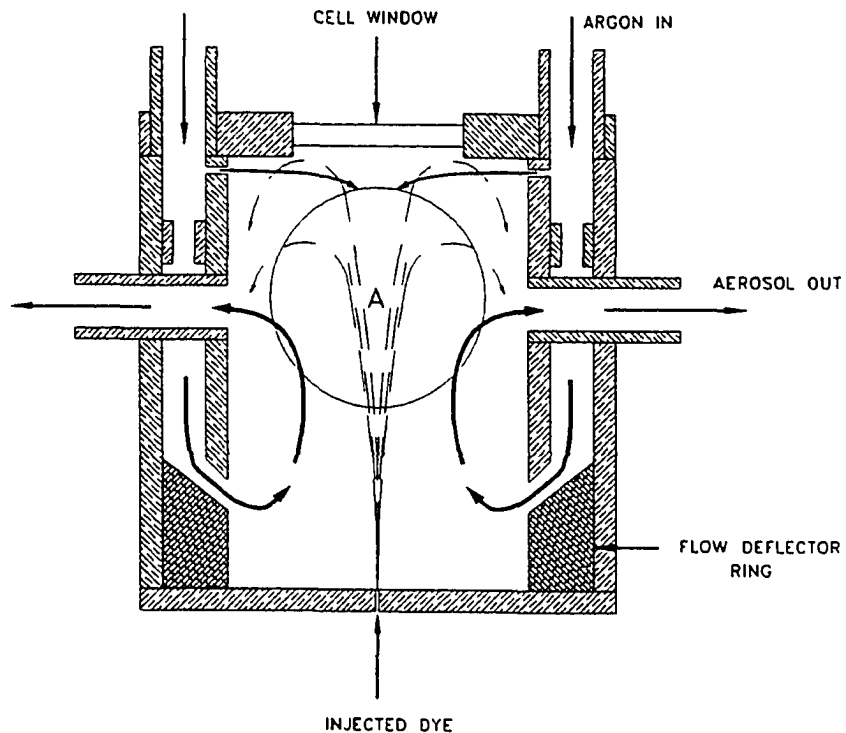


Figure 6.7: Ablation cell model no. 6.

(region A) which is shown as an ellipse in Figure 6.7. This region is very helpful in maintaining a continuous supply of aerosol to the ICP torch.

Cell model no. 6 This model as shown in Figure 6.7, was almost identical to cell design no. 5, except that the outlet ports were enlarged and had rectangular shape. Because of this change, the suction effect at the center of the ablation cell was less than the previous design. Therefore, the ablated particles could travel further upward without being deflected by the suction force from the output ports. The mixing and entrainment characteristics were very good and there was very little particle deposition on the bottom of the cell. The main disadvantage of this cell was the increased likelihood of particle deposition on the window. The flushing time of this cell increased to 22-24 sec. The suspended particle cloud had a round shape (shown as circle in Figure 6.7) and it had a relatively stationary center.

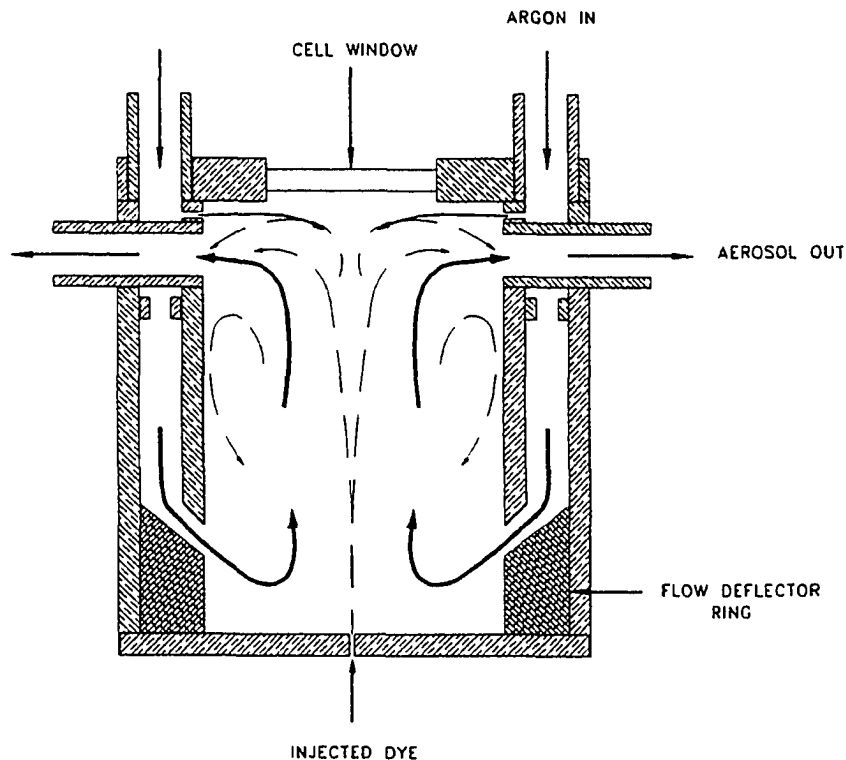


Figure 6.8: Ablation cell model no. 7.

Cell model no. 7 In this design, in order to study the positioning (height) effect of the outlet ports on the cell characteristics, the outlet ports were mounted very close to the top of the ablation cell (Figure 6.8). By putting the outlet ports at this location, the flushing time was decreased to 18-20 seconds but the chance of deposition on the window was considerably increased.

6.1.3 Optimum Cell Design Selection

A set of characteristics was established to compare and evaluate the performance of the above ablation cell designs. A matrix of these characteristics was used to determine the best design based on the results from the visual flow pattern study. The selection matrix incorporated a multiplicative weight between one and ten for each characteristics, and a number between one and ten as how each cell model performs in relation to these characteristics. These two numbers were multiplied together and summed to produce a total score for each cell model. After careful examination of: 1- particle entrainment, 2- mixing, 3- flushing time, 4- particle deposition on the window, 5- memory effect, 6- volume, and 7- particle concentration at the center of each individual cell design and determining their weight, a spread sheet was used to calculate the total scores for each ablation cell model (see Table 6.1). As shown in Figure 6.9, based on this evaluation, cell design no. 5 was chosen for next step related to building a prototype model.

6.1.4 Final Cell Design

Based on the results from the study of flow pattern inside the Plexiglas model cells, a cell design similar to the cell no. 5 was selected for the field application design. This cell, as shown in Figure 6.10, has five different components: ablation chamber, window, water reservoir ring, knife edge ring, flow deflector ring, and cell mounting plate. All the drawings for the individual parts of the surface ablation cell used for manufacturing are listed in Appendix C.

Table 6.1: Ablation cell design evaluation

	Weight	Cell 1	Cell 2	Cell 3	Cell 4	Cell 5	Cell 6	Cell 7
Particle entrainment efficiency	10	10	4	8	3	8	10	10
Mixing efficiency	8	5	7	4	7	10	10	9
Flushing time	6.5	10	8	4	2	8	8	9
Particle deposition on window	5	10	6	8	5	9	7	6
Memory effect	3	6	4	5	2	8	7	6
Volume	2.5	9	6	8	5	4	4	4
Particle concentration at center	2	5	6	5	6	6	5	5
Total		245.5	257	173	204.5	323	308	298.5

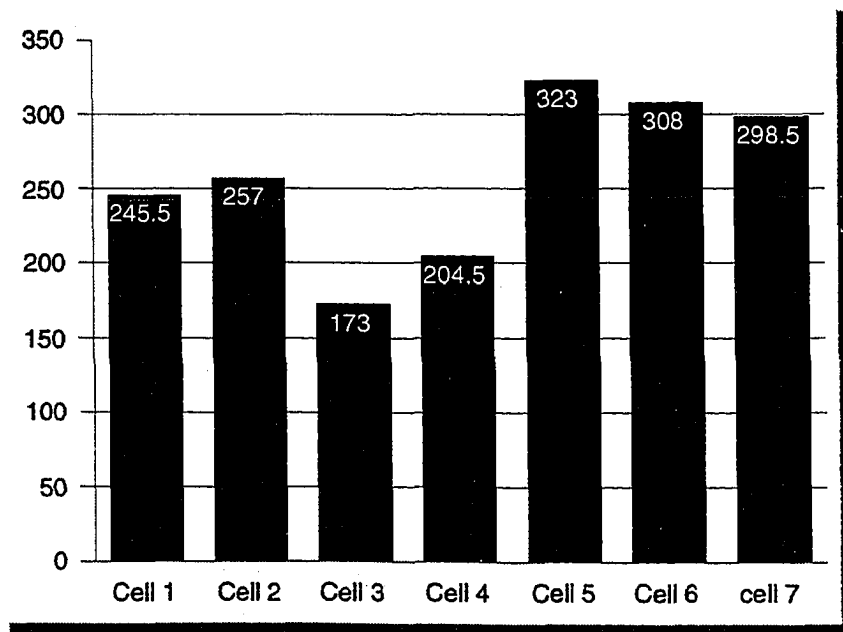


Figure 6.9: Ablation cell design selection graph.

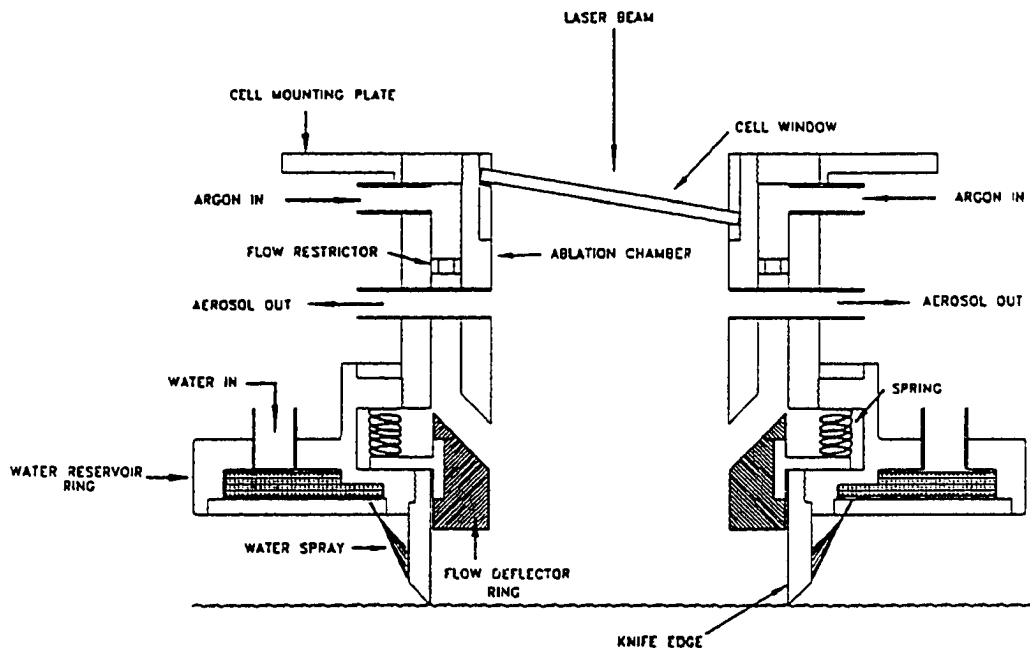


Figure 6.10: Surface Ablation Cell Design.

Ablation Chamber: The ablation chamber consists of two annular concentric tubes with 2 and 2.5 inch inside diameters and a window which seals the upper end of the chamber. There are two opposite input ports connected to the upper portion of the outer tube which supply argon gas to the ablation chamber. Two opposite output ports are also connected to the middle of the inner tube to carry out the generated aerosol via the transfer line to the ICP torch. The space between these concentric tubes provides a uniform passage for the inlet argon gas to flow downward and cover the sample surface. A flow restricting ring with four holes (1/8 inch diameter) was mounted between the concentric tubes to provide a back pressure for the flow to clean the window and also to increase the inlet flow velocity around the sample surface.

Cell Window: A window mounted on the top of the ablation chamber, seals one end of the chamber and provides a path for the laser beam to interact with the sample inside the cell. The window is mounted at an 10° angle with respect to the horizontal line to offset the reflection

of the laser beam from the soil surface on a photo-diode located above the cell. This photo-diode is used to measure the laser beam energy before it is focused. Two supporting rings hold this window in its place and seals the upper end of the chamber. By removing the upper ring the window could be cleaned or replaced in a very short period of time during field operations. Seven small holes with diameter of 0.01 inch are drilled on one side of the upper portion of the inner tube to direct a continuous flow of argon gas to the lower surface of the window in order to prevent particle deposition on the window.

Water Reservoir Ring: Argon gas penetration through soil depends on several factors such as: soil type, soil compaction, and moisture content of the soil. By adding water to the soil and increasing its moisture level the permeability of the soil decreases significantly. In a series of tests performed at the Ames Laboratory, the argon gas leak through the soil was decreased from 60-70% in a low moisture content soil to 30-40% by adding water to the soil.

In order to lower the argon gas leak through the soil during the testing, a water reservoir ring with a 7 inch outside diameter was designed and attached to the lower end of the outer tube of the ablation chamber. There are 36 small holes on the lower face of this ring to spray water on the soil to decrease the argon gas leakage through the soil. This ring also provides a base to attach the knife edge ring and a guide for the flow deflector ring.

Knife Edge Ring: To minimize the argon gas leak from the ablation chamber through the soil, a knife edge ring is attached to the lower portion of the water reservoir. In the above mentioned tests, by using a knife edge ring and pushing it into the soil and spraying water on the soil outside of the ring during the testing, the argon gas leak through soil was decreased from 60-70% to 15-20%.

Flow Deflector Ring: A spring loaded flow deflector ring was mounted inside the ablation chamber to increasing the particle entrainment and mixing efficiency of the cell. The upper face of this ring makes a 45° angle with the soil surface and deflects the incoming argon gas on this surface. This is a multipurpose device with the following functions:

1. To increase the turbulence of the flow on the surface of the soil and enhance the particle entrainment efficiency.
2. To improve the homogeneity of the aerosol due to the turbulent flow.
3. To decrease the flushing time of the cell by decreasing the cell volume.
4. To push out or eject the trapped soil inside of the knife edge ring after each test.
5. To improve the argon gas leak by deflecting the gas flow.

Cell Mounting Plate: A 4x4 inch steel plate with a 2 inch diameter hole at its center is attached to the top of the ablation cell. This plate is used as a quick mounting device to attach the ablation cell to the robotic end effector (sampling probe) by sliding the plate into a set of rails mounted on the bottom of the optic housing.

6.1.5 Force Analysis

The maximum applied vertical load on the outer cell wall was about 300 lbs. This load includes the weight of the sampling probe, and force applied by the robot arm to push the cell's knife edge into the soil.

6.1.6 Material Selection

By considering the performance required from each cell component during testing, different materials were selected to fabricate these parts.

Outer Wall: The outer cell wall carries all the external loads on the cell and is also exposed to the environmental conditions such as: corrosion, erosion, and chemical reactions during the decontamination process. Therefore, a 304 stainless tube which has good corrosion resistant and high strength was used to build the outer cell wall of the ablation cell.

Inner Wall: The inner cell wall was threaded to the upper part of the outer cell wall. In order to prevent thread lock problem associated with fastening two similar materials together a brass tube was used to build this wall.

Window: The operational wavelength of the Nd-YAG laser used for soil ablation was between 1064-532 nm. In order to minimize the laser beam power attenuation due to absorption, a quartz glass window with a 2.5% absorption coefficient was selected.

Water Reservoir: This component is the largest and the most complicated part in the ablation cell and it is attached between the outer cell wall and the knife edge. To prevent the thread lock problem and to provide better machining properties, brass was selected to for this ring.

Knife Edge Ring: This ring has direct contact with the soil and moisture. It should be strong enough to carry the applied force and to penetrate in soils with different degree of compaction. For these reasons, a 304 stainless steel tube was used to manufacture the knife edge ring.

Cell Mounting Plate: A 304 stainless steel plate was also used to build this plate.

Flow Deflector Ring: This rubber ring is mounted on a spring loaded mounting ring and is used to guide the argon gas flow to the surface of soil sample.

6.2 Sub-Surface Ablation Cell

The sub-surface ablation cell is designed for collection and entrainment of the laser ablated soil sample from below ground up to 100 feet deep. For this application, holes are made in the ground by pushing a series of steel tubes with a 9-inch outside diameter and 1.5-inch wall thickness into the soil using a diesel-powered hammer. A hardened steel cutting edge is welded to the one end of the first tube and the other end of this tube is threaded to connect to an additional tube as the drilling process continues. There is a 1.5-inch diameter hole on the side wall of this tube (near the tip) in order to have access to the soil during the sampling process. This hole is blocked by a removable blocking mechanism that prevents soil from entering the tube during the drilling process. After establishing the desired hole depth, the blocking mechanism is removed from inside of the tube, and the sampling probe is lowered into the tubing which remains in the hole until the testing is completed.

The sub-surface ablation cell has a completely different configuration than the surface ablation cell design, however the design criteria and basic principals of flow interaction with ablated particles are the same.

6.2.1 Flow Pattern Study Inside the Cell Using a Plexiglas Model

Based on the results from the surface ablation cell design, and considering the space restriction inside the tube as well as the accessibility of the sampling area, a Plexiglas model of the sub-surface ablation cell design and drilling tube mockup were build. This model was used to perform a preliminary visual flow study inside the ablation cell. By using water as the flow medium and dye to represent the ablated soil particles, the patterns of the flow inside the cell were recorded and studied by a high-speed camcorder.

This sub-surface model, as shown in Figure 6.11, is a round cell (with a 2-inch inside diameter) which is attached to the sampling probe wall. There is only one input and one outlet port in this cell. The incoming gas after being deflected by a 120° arc shaped channel (located above the input port) is directed to the sampling soil surface to entrain the ablated particles. There is a small opening between this channel and the cell window to allow the argon flow to

wash off the inside surface of the window. The opening on the tube wall has a hemispherical shape on the inside and a square shape on the outside. By introducing the inlet gas flow through the arc shape channel and utilizing the contours of the wall opening, three distinct flow regions were created inside the cell:

Region A: The lower curved contour of the wall opening was used to guide the input flow parallel and tangent to the surface of the sampling soil such that it will lift and carry the sub-micron size ablated particles. Because of their low mass, these particles have a tendency to fall due to the gravity force after being made airborne during the ablation process. The flow at this region also changes the direction of the larger ejected particles by applying upward drag forces on them.

Region B: The flow of gas inside the lower and upper contours of the wall opening creates a rotating mixing region at the center of the opening next to the region A. This region also changes the direction of the ejected particles further to the upper section of the cell. This rotating flow improves the mixing characteristics of the cell and meanwhile prevents the ablated particles from reaching the cell window.

Region C: In this region which occupies most of the upper half volume of the cell, the generated aerosol is very homogenous and is carried out through the output port.

By reducing the opening of the arc shaped channel, the flow velocity leaving the channel could be increased. The increase in the inlet velocity shifts the location of the rotating turbulent region to above the center line of the wall opening.

6.2.2 Final Cell Design

After careful study of the flow pattern inside the plexiglas model, a cell design similar to this model with some dimensional modification was selected to build a prototype model for field application. The final cell (Figure 6.12) has five different components: ablation chamber, window, flow deflector channel, cell mounting plate, and inflation ring for sealing. All the drawings for individual parts of the sub-surface ablation cell used for manufacturing are listed in Appendix C.

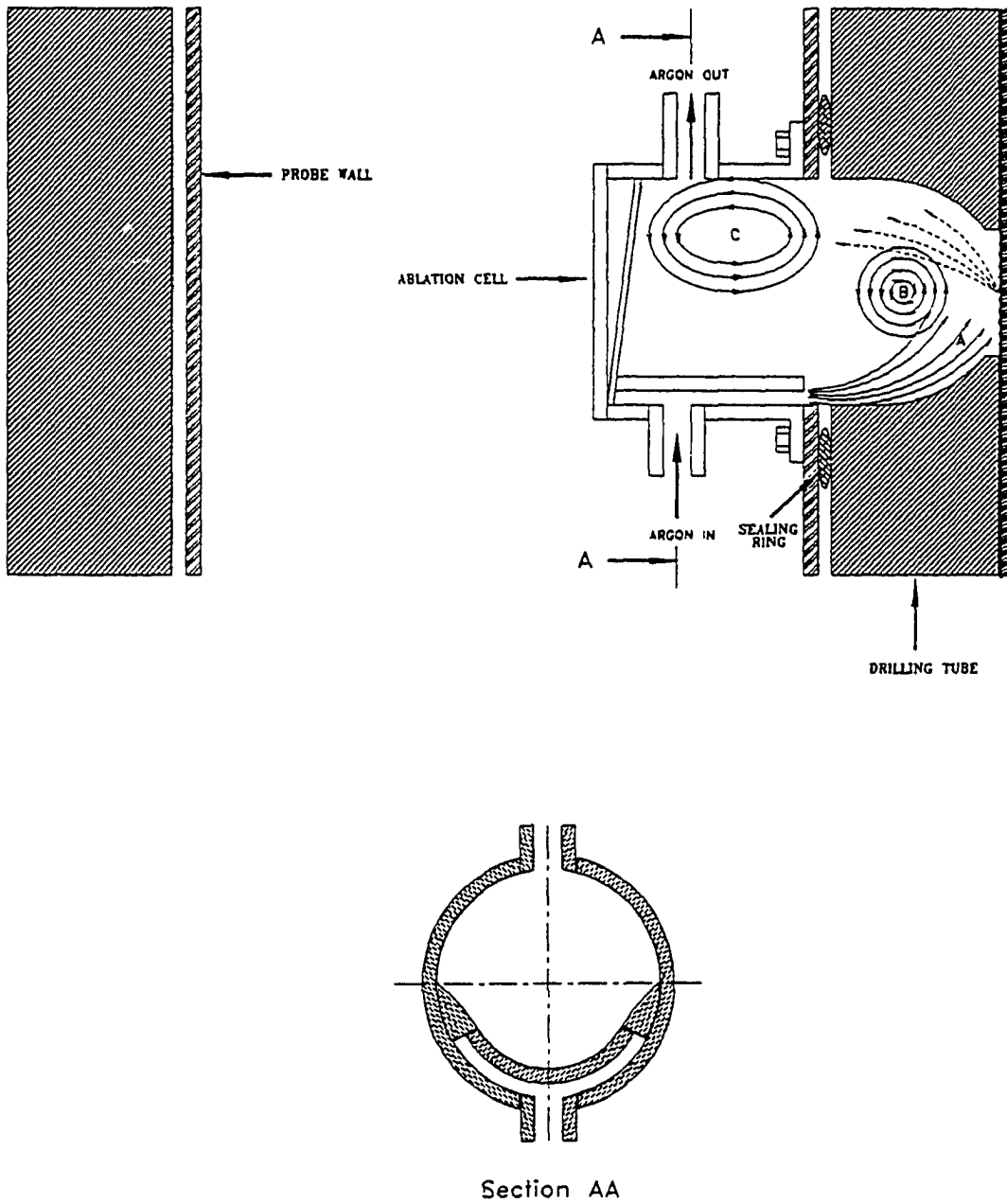


Figure 6.11: Flow Pattern inside the sub-surface ablation cell model.

Ablation Chamber: The ablation chamber consists of an annular tube with a 2-inch inside diameter, and an arc shaped flow deflector channel attached to the lower wall of the tube. This cell has one input port connected to the lower wall of the tube where the flow deflector channel is located and one output port connected to the upper wall of the tube. The argon gas is introduced into the cell through the input port from the surface by a 100-foot Tygon tubing. The aerosol inside the cell is then carried out to the ICP torch located at the surface via another section of Tygon tubing. One end of this cell is soft soldered to a supporting plate and the other end is closed by a window.

Cell Window: A window mounted at an 10° angle with respect to the vertical line on one end of the chamber, provides a path for the laser beam to interact with the sample inside the cell. Two supporting rings hold this window in place and seal one end of the chamber. By removing the outer ring, the window can be cleaned or replaced. There is a small gap between the window and the flow deflector channel which directs a continuous flow of argon gas to the inner surface of the window in order to prevent particle deposition on the window.

Supporting Plate: The ablation chamber is soft soldered to the center of a curved plate, with a 2-inch diameter hole at the center, which is attached to the sampling probe's supporting rods by two brackets. This plate is also used to mount the inflatable sealing ring on the sampling probe.

Inflatable Sealing Ring: An inflatable sealing ring mounted on the outer surface of the supporting plate is used to seal the gap between the outer wall of the sampling probe and the inner wall of the drilling tube. When the probe is lowered into the drilling tube, this ring is inflated by high pressure argon gas in order to prevent the leakage of the argon gas from the ablation chamber through that opening.

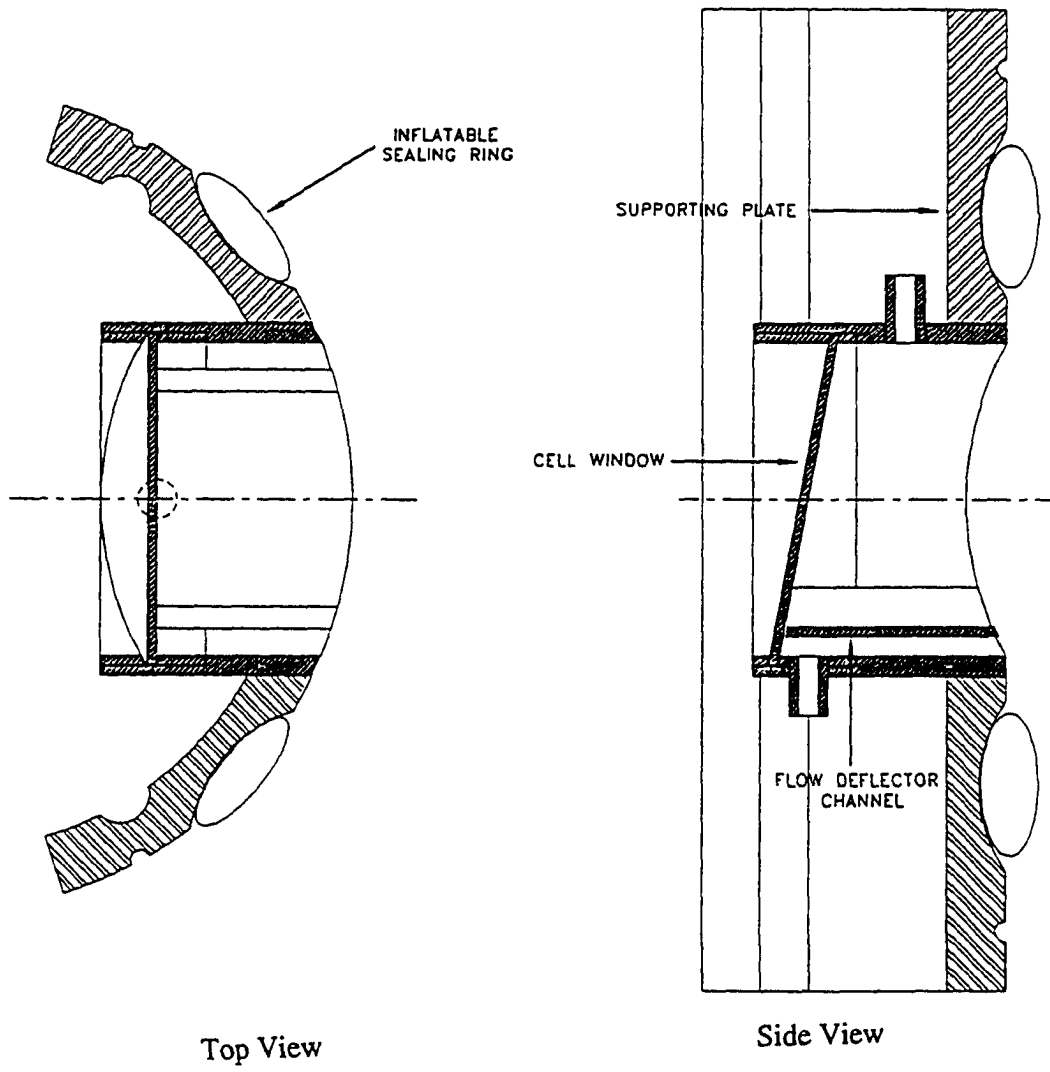


Figure 6.12: Sub-surface ablation cell design.

6.2.3 Material Selection

The material selections for the manufacturing of different parts of the sub-surface ablation cell are as the following:

Ablation Chamber: A 304 stainless tube, which has good corrosion resistant properties, was used to build the ablation chamber and the flow deflector.

Window: The operational wavelength of the Nd-YAG laser used for soil ablation was between 1064-532 nm. In order to minimize the laser beam power attenuation, a quartz glass window with 2.5% absorption coefficient was selected.

Cell Mounting Plate: A brass tube was used to build this plate and its two brackets.

Inflatable Sealing Ring: This ring could be exposed to moisture, dust, and oil during the testing period; therefore, a durable vinyl material with high chemical resistance property was selected for manufacturing this ring.

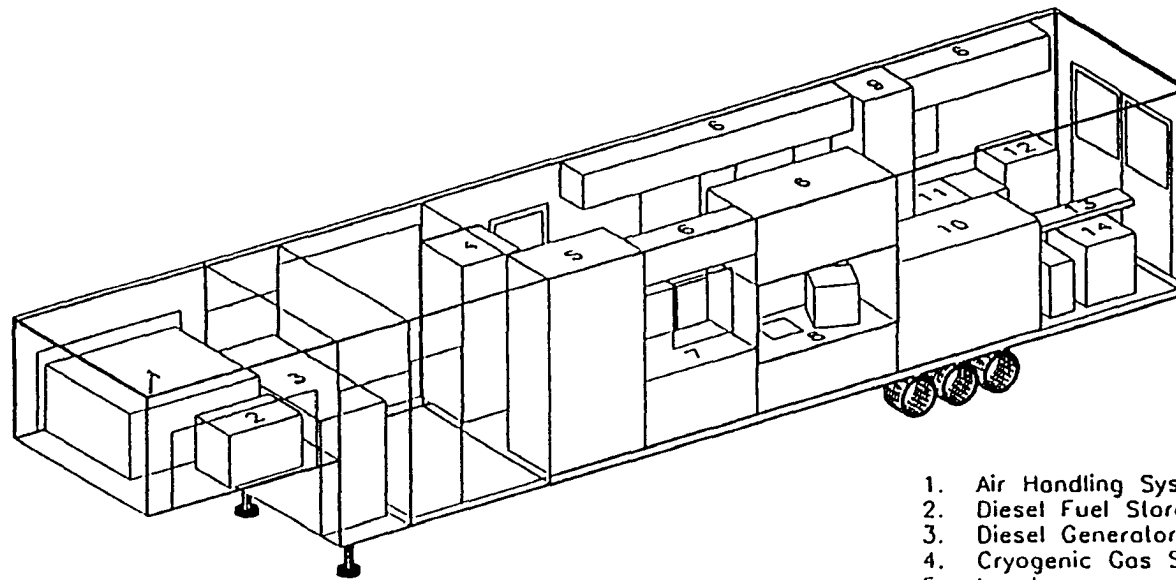
CHAPTER 7. EXPERIMENTAL SETUP

In this chapter, the experimental setup used for testing the performance of both the surface and sub-surface ablation cells are described. The characteristics of the output signals for both cells were studied by utilizing the instruments mounted in the Mobile Demonstration Laboratory for Environmental Screening Technology (MDLEST). The ICP-MS and ICP-AES techniques were implemented for each cell design. The particle size distribution analysis of the ablated materials was performed by using the MDLEST, Scanning Electronic Microscope (SEM), and Image Analyzer.

The MDLEST is a 36-foot long trailer with utilities and instrumentation, designed and built by Technology Integration Program (TIP) team, to support screening and monitoring of soil at the various DOE facilities. This unit contains different instruments such as a laser, inductively coupled plasma-atomic emission spectrometer (ICP-AES), inductively coupled plasma-mass spectrometer (ICP-MS), Diesel powered generator, robotic surface sampling accessory (RSA), computers, and electronics to control the entire operation of the system. In the following sections, the over all layout of the instrumentation in the MDLEST and specifications of the individual instruments used to run this experiment are briefly described.

7.1. Instruments layout in the MDLEST

The layout and the list of different instruments in the MDLEST used for performing the elemental analytical analysis is shown in Figure 7.1.



1. Air Handling System
2. Diesel Fuel Storage Tank
3. Diesel Generator
4. Cryogenic Gas Storage
5. Lavatory
6. Overhead Storage
7. Workspace
8. Sample Preparation Area
9. Electronics Equipment Rack
10. Spectrometer
11. System Control Center
12. Neslab Chiller
13. Laser Mount
14. Laser Power Supply

Figure 7.1: A perspective view of the MDLEST showing the location of the instrumentation and utilities.

7.1.1 Laser

In this study, two different sets of Q-switched Nd-YAG laser were used to ablate soil samples. In the first setup, the laser beam from the laser unit mounted in the MDLEST, was delivered to the test sites using fiber optics. The second laser was built in the end effector sampling probe for direct laser ablation of soil samples thus eliminating the need for the fiber optics.

7.1.1.1 Laser Ablation Using Fiber Optic

In this set up, the laser beam was transferred from the laser unit located in the MDLEST to the test site via a 100-foot long fiber optic. This fiber is a part of 100-foot long umbilical cord which was used to connect the sampling probe to the MEDLEST. The specification of this laser unit is as the following:

Specifications:

Laser:	Continuum NY 81-20 Nd- YAG
Wavelength	1064 & 532 nm
Repetition rate	30 Hz
Mode of operation	Q- switched
Pulse duration	7 nsec.
Fiber optic length	100 feet
Fiber optic core diameter	600 μm

Due to the difficulties encountered in coupling the high power laser beam with the fiber optics such as: laser beam power losses at the coupling with the fiber optics, and the laser beam reflection by the focusing optics, the maximum power delivered to the soil at 532 nm was about 3 mj. With the minimum spot size of 600 μm and the laser pulse duration of 7 nsec, the maximum laser power density delivered to the soil was about 10^8 watts/cm².

7.1.1.2 Direct Laser Ablation

In order to increase the amount of laser energy delivered to the sampling soil, a compact Nd-YAG laser was built inside the end effector sampling probe for direct laser ablation. This laser unit has the following specification:

Specifications:

Laser:	Big Sky Laser model 255A NY 81-20Nd:YAG
Wavelength	1064 & 532 nm
Repetition rate	30 Hz
Mode of operation	Q- switched
Pulse duration	8 nsec.

This laser was able to deliver about 9 mj energy to the soil surface and by focusing the laser beam to a smaller diameter (100 μ m), the delivered laser power density to the soil was about 10¹⁰ watts/cm².

7.1.2 ICP-MS

For a rapid multi-element quantitative determination of trace elements, a Perkin-Elmer ICP-MS with the following specifications was mounted in the MDLEST (Figure 7.2). This instrument was used for studying the performance of the surface and sub-surface ablation cell design.

Model:	SCIEX ELAN 5000 ICP-MS
Torch gas flow:	15 liter/min
Auxiliary gas flow:	0.8 liter/min
Nebulizer gas:	0.9 liter/min
RF power:	1050 w
RF frequency:	35-MHz free-running
No. of elements:	75
Vacuum pump pressure:	8 x 10 ⁻⁴ torr

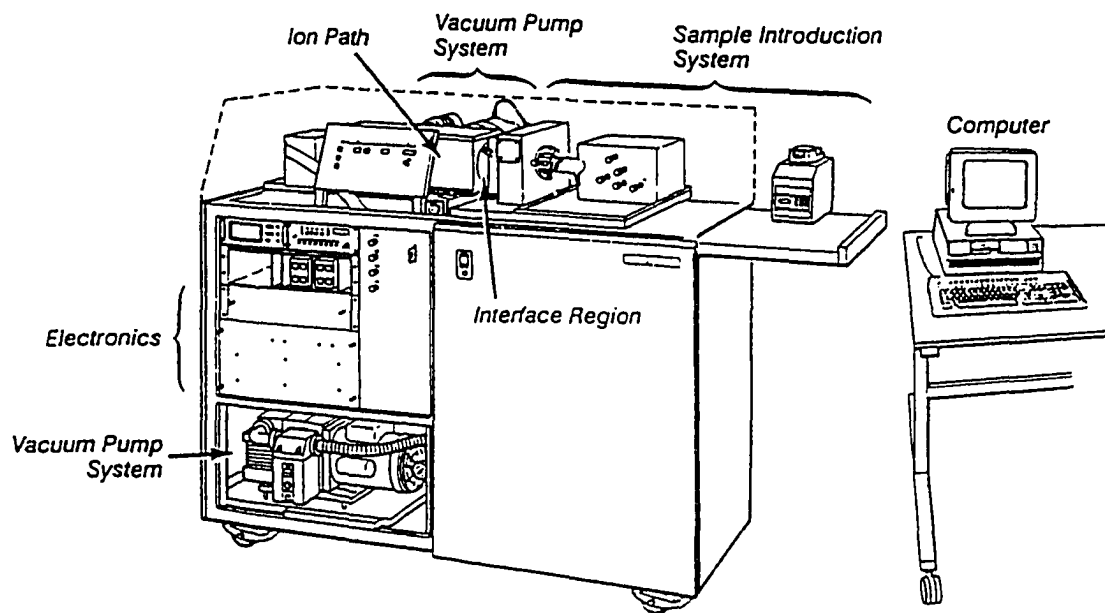


Figure 7.2: The Elan 5000 Inductively Coupled Plasma-Mass Spectrometer (ICP-MS).

Einzel lens voltage: -130 volts

CEM voltage: -3000 to -5500 VDC

The effect of the flow deflector ring gap, argon gas flow rate in the cell, and cell volume on the output signal intensity of the ICP-MS were studied by utilizing this instrument.

7.1.3 ICP-AES

For elemental analysis of soil samples, a Thermo Jarrell Ash ICP-AES (Figure 7.3) with the following specifications was mounted in the MDLEST. This unit was used to study the performance of the surface ablation cell.

Model:	ICAP 61E
Torch gas flow:	High 15 liter/min
Auxiliary gas flow	Low 0.5 liter/min
RF power:	950 w
Plate current:	520 mA
Pump rate:	110 rpm
Height of Yttrium tongue above torch:	1 mm
Height of torch above entrance slit:	15 mm
Purge pressure:	6 in/w.c.
Purge flow :	2 liter/min
purge exhaust:	2 liter/min
P.O.P. tube flow:	2 liter/min
P.O.P. tube nozzle flow:	2 liter/min

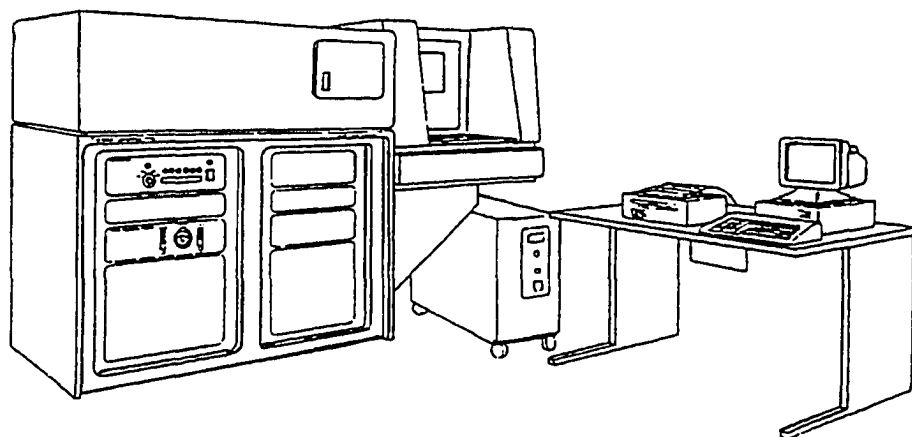


Figure 7.3: Assembled ICAP 61E spectrometer system (ICP-AES).

The effects of the flow deflector ring gap, cell volume, and the argon gas flow rate of the surface ablation cell on the characteristics of the output signals from the ICP-AES were studied by using this setup.

7.1.4 Robotic Surface Sampling Accessory (RSA)

For remote soil sampling, a three degree of freedom SCARA (selective compliance assembly robot arm) robot as shown in Figure 7.4, was used in conjunction with the MDLEST. This robot is mounted on a small trailer and is pulled by the MDLEST during site characterization. The robot is capable of performing the solid sampling process by carrying the end effector, which is mounted on the end of the robot arm, to a predetermined location. The RSA decreases the sampling time and lowers the risk of exposing operators to the radioactive wastes and other dangerous chemicals at the contaminated sites. The movement of this robot is controlled by a computer from the MDLEST.

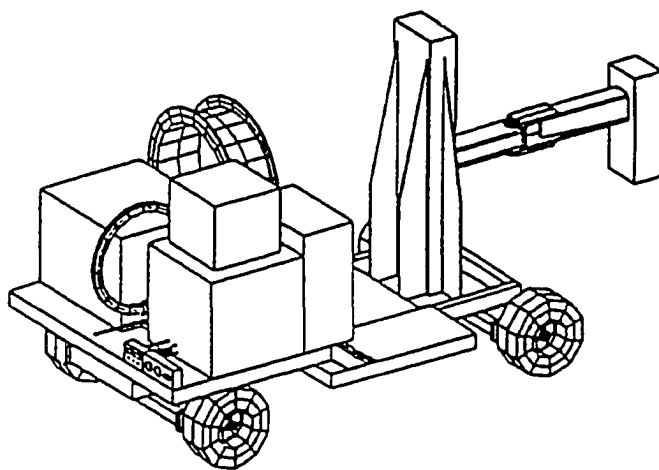


Figure 7.4: Robotic Surface Sampling Accessory (RSA).

7.1.5 Surface Sampling Probe

The surface sampling probe (end effector) is connected to the MEDLEST by a 100-foot long umbilical cord. This cord includes: the power and controlling lines for the rastering unit, inlet and outlet argon gas tubes, and signal lines for laser beam focusing. The sampling probe contains the following components which are essential for laser ablation sampling:

Optics: A set of lenses was used to focus the laser beam, transferred by the fiber optic, to its minimum diameter on the surface of the soil. One of these lenses was mounted next to the fiber optic end in a fixed position. The second lens was attached to the end of a Z axis positioning table. Focusing of the laser beam was accomplished by controlling the Z axis position and adjusting the distance between these two lenses.

Focusing System: Focusing of the laser beam on the soil surface is done automatically before the rastering motion starts. A photo-diode sensor is used to measure the intensity of the laser beam reflected from the soil surface. This intensity is proportional to the laser spot diameter on soil. The output of the photo-diode sensor is sent to a control computer mounted in the MDLEST. By using a special program developed for focusing, this computer is capable to adjust the Z axis position until the laser beam is focused to its minimum diameter.

Rastering Unit: In order to accurately characterize a site, a representative sample of each sampling location is required. To obtain a representative ablated sample, the laser beam is rastered over the soil surface by a rastering unit. A precision x-y positioning table was selected to performed the rastering motion. This table positioning could move the focused laser beam on the soil surface with different rastering patterns. For surface sampling, a spiral rastering pattern (Figure 7.5.a) was selected in order to keep the rastering table in a smooth curvilinear motion. This will minimize the vibration of the moving components of focusing system due to the change in the direction of the motion. A minimum spiral rastering diameter of 1.13" is required to cover the specified one square inch of ablated sample area. Because of different focusing setup, a linear rastering pattern (Figure 7.5.b) was selected to move the laser beam on the soil surface for the sub-surface sampling,. The rastering speed and separation

distance between two consecutive laser shots could be adjusted by using the rastering system program. Specifications of the rastering pattern follow:

Maximum rastering diameter:	32 mm
Rastering speed:	1 - 20 mm/s
Separation distance:	0.1 - 1.25 mm

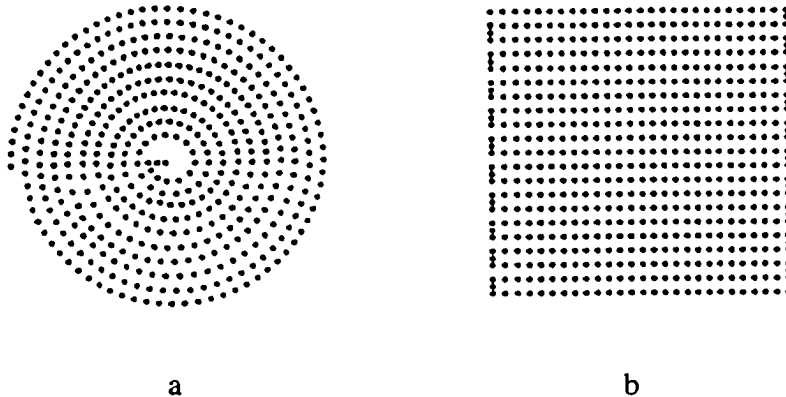


Figure 7.5: The rastering patterns used for (a) surface and (b) sub-surface laser ablation.

Ablation Cell: The surface ablation cell, as described in the Chapter 6, is attached to the bottom of the robotic end effector. This cell is used to collect solid soil samples for the ICP-MS, ICP-AES, and particle size analysis.

7.1.6 Sub-Surface Sampling Probe

This probe, like the surface sampling probe, has different components for ablation of the soil, such as: optics for focusing the laser beam, rastering unit for moving the laser beam on the soil surface, and ablation cell for entraining the ablated particles. This probe is used for studying the sub-surface ablation cell performance using ICP-MS.

7.2. Operational Configuration of the MDLEST

For synchronizing, controlling, and monitoring the operation of the different instruments in the MEDLEST, five different computers were used in this mobile lab (Figure 7.6). The following is a brief description of these computers and their functions:

System Control Computer: The main task of this computer is to control and monitor the functions of the necessary accessories required for running the laser, chiller, ICP-AES, and ICP-MS units. The list of tasks which is performed by this computer during a sampling period is as follows:

- 1- Controlling and monitoring the focusing process.
- 2- Controlling and monitoring the motion of rastering unit.

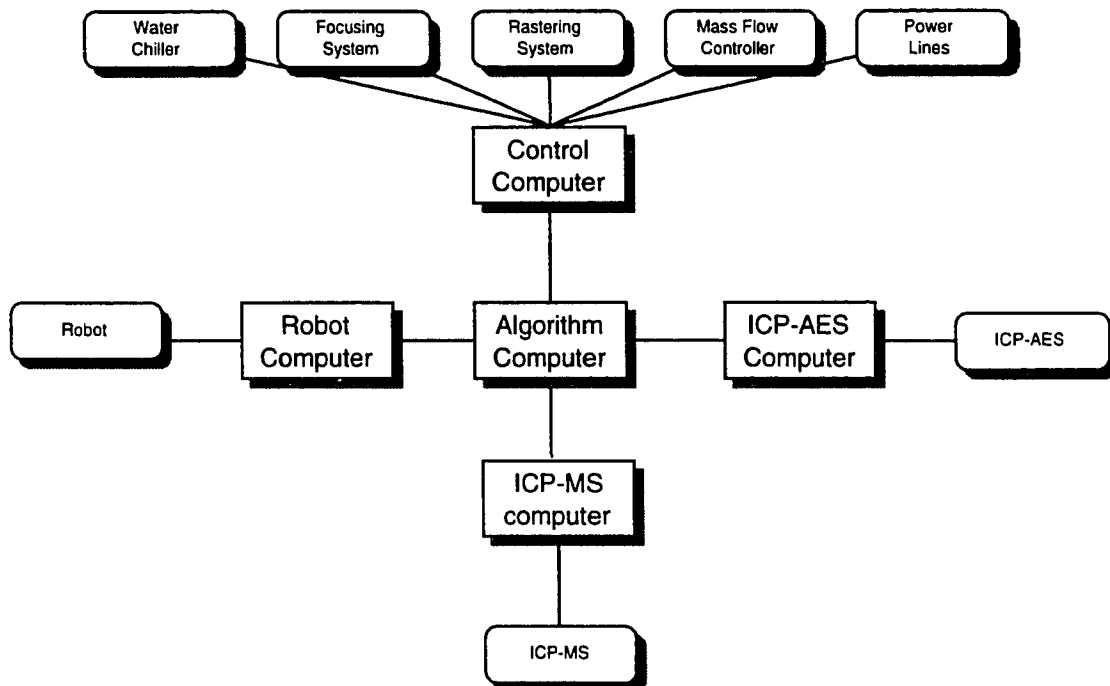


Figure 7. 6: The operational configuration of the MDLEST.

- 3- Monitoring the temperature of chiller, laser cooling system.
- 4- Controlling and monitoring the mass flow controllers.
- 5- Controlling and monitoring the power line to different units.

Algorithm Computer: This computer, which is the center of the MDLEST control system, is connected to other four computers as explained in the following sections. The data handling, data analysis, and data presentation is performed by this computer.

ICP-AES Computer: This computer controls the main functions of the ICP-AES. By collecting, sorting, and storing the generated data from each experiment, this computer also acts as a data acquisition unit for the ICP-AES.

ICP-MS Computer: This computer controls the main functions of the ICP-MS unit, and it also collects and stores the generated data from ICP-MS.

Robot Computer: The movements of the robotic arm on the trailer during the sampling process is controlled and monitored by an additional computer. This computer also specifies the sample site locations by moving the end effector to a preset sampling position.

7.3 Soil Samples

Two radio-nuclide reference materials (NRM5 and NRM6) were used for the signal intensity study of both surface and sub-surface ablation cells using ICP-AES, ICP-MS. These samples were also used for the particle size distribution analysis. These soil samples were prepared with varying concentrations of radio-nuclide using mill tailing materials, ores, and a river-bottom soil diluent [25]. The grain size of the sample was less than 0.6 mm in diameter. The specifications of these samples are as the following:

NRMS

U-238	22.6 ± 1.6 pCi/gram	$[67.12 \pm 4.75$ ppm]
U-234	22.2 ± 1.7 pCi/gram	$[3.56 \pm 0.27$ ppb]
Ra-226	22.7 ± 1.9 pCi/gram	$[22.97 \pm 1.92$ pptr]
Th-230	25.5 ± 1.8 pCi/gram	$[1.31 \pm 0.093$ ppb]
Th-232	18.0 ± 1.1 pci/gram	$[164.7 \pm 10.1$ ppm]
Pb-210	16.8 ± 1.7 pCi/gram	$[0.22 \pm 0.022$ pptr]

NRM6

U-238	42.9 ± 3.4 pCi/gram	$[127.4 \pm 10.1$ ppm]
U-234	42.4 ± 2.8 pCi/gram	$[6.80 \pm 0.45$ ppb]
Ra-226	44.6 ± 2.2 pCi/gram	$[45.14 \pm 2.23$ pptr]
Th-230	49.7 ± 2.9 pCi/gram	$[2.56 \pm 0.15$ ppb]
Th-232	34.4 ± 1.1 pci/gram	$[314.8 \pm 10.1$ ppm]
Pb-210	32.4 ± 3.3 pCi/gram	$[0.424 \pm 0.043$ pptr]

7.4 Particle Size Distribution

In this study, a particle size distribution analysis was performed in order to explain the effect of the flow deflector ring gap on the characteristics of the output signal from both ICP-AES and ICP-MS. Samples of entrained particles (aerosol) in the ablation cell were collected on special filters. Then, these filters were photographed by using a Scanning Electronic Microscope (SEM). Finally, the size and the number of the ablated particles were determined by using an image analyzer. This process is explained in the following sections:

7.4.1 Filters

Polycarbonate filters were used to collect the aerosol samples from the transfer line and have the following specifications:

Material:	Polycarbonate
Pore size:	0.4 μm & 0.1 μm
Thickness:	10 μm & 6 μm
Flow rates (air):	50 liter/min & 10 liter/min
Pore density:	1 x 10 ⁸ pores/cm ² & 4 x 10 ⁸ pores/cm ²

Gold Plating Filters: In order to obtain an adequate image from the SEM, these filters were gold plated prior to collecting any samples. Gold plating filters provide a grounding matrix for the collected soil particles to dissipate the charges they gained during the ablation process. This allows the electron beam of the SEM to scan the sample without being deflected and distorted by the charged particles.

7.4.2 Scanning Electronic Microscope

A Scanning Electronic Microscope (SEM) was used to study these samples and to take pictures for performing the image analysis. The SEM provided useful information about the shape, size, area, and the number of the ablated particles. A Cambridge 200 SEM was used to photograph the samples on the gold plated filters during this experiment.

7.4.3 Image Analysis

To determine the size and number of the ablated particles, pictures of the collected samples on the gold plated filters taken by the SEM were analyzed later by using an Image Analysis technique. Photos of the particles were placed on a copy stand. Images were captured, interactively discriminated, and edited if necessary. This method provides the required information about the number of ablated particles, their minimum and maximum diameters, the area of each particle, the aspect ratio of the particles, and the circularity shape factors of the particles. A Zeiss-IPS image analysis system (Zeiss-Kontron; IBAS version 2.00) and a Sony DXC-3000A 3 CCD color video camera were used in conducting this experiment.

CHAPTER 8. RESULTS

In this chapter the experimental test results from performance of both the surface and sub-surface ablation cells are explained. These results are presented in three main categories: 1- Ablation cells performance using the ICP-MS, 2- Ablation cell performance using the ICP-AES, and 3- Particle size distribution using the SEM and Image Analyzer.

8.1. Ablation Cells Performance Using the ICP-MS

This section focuses on the performance of both surface and sub-surface ablation cells using the ICP-MS. The effect of the flow deflector ring gap, cell volume, and flow rate of the inlet argon gas of both cells on the characteristics of the output signal from the ICP-MS are discussed. As explained in chapter 3, there are different factors involved with the laser ablation process and inductively coupled mass spectrometry process, which could effect the output signals. In order to eliminate some of these effects, laser power, laser wave length, laser frequency, laser pulse duration, laser spot size, rastering speed, and separation between rastering points were kept constant during the experiments.

The ICP-MS is a very sensitive instrument in which the vacuum pressure at the interface chamber has a very significant effect on the intensity of the output signal. The vacuum pressure inside the interface chamber mainly depends on the size of the hole on the sampler cone. Due to the deposition of partially disassociated ablated particles in the plasma around this hole during the testing period, its diameter gets smaller as testing proceeds. As the diameter gets smaller, the vacuum pressure drops and the intensity of the output signal decreases. This effect is more

pronounced when solid samples are introduced to the ICP torch. Therefore, in order to make a true comparison of the results obtained during this experiment, the signal intensities of these results are all normalized.

8.1.1 Surface Ablation Cell

In this experiment a 100-foot long fiber optic was used to deliver the laser energy to the prototype surface ablation cell. The delivered laser power density to the soil surface was kept constant at 10^8 w/cm². A radionuclide standard soil sample (NRM5) was used for solid sample introduction into the ICP torch.

8.1.1.1 Flow Deflector Ring Gap Effect

The effect of the flow deflector ring gap on the efficiency of the particle entrainment of the ablation cell and thus the signal intensity of the ICP-MS was investigated by running a series of tests. During these tests the gap was gradually decreased and the output signal was recorded. In the first test, deflector ring was not mounted in the ablation cell and the soil sample was not packed. The output signal profile for Si 29, Th 232, and U 238 are shown in Figure 8.1. The flow pattern inside the cell was very close to laminar flow, except at the regions where the laser was ablating the soil sample.

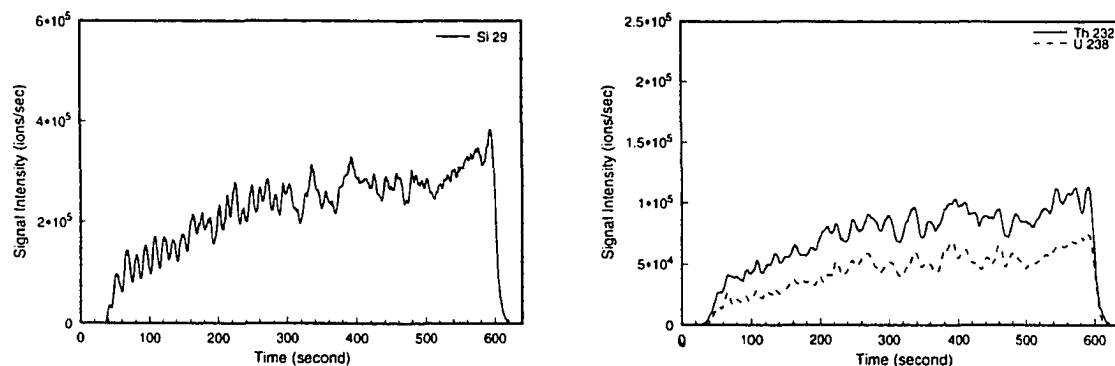


Figure 8.1: Signal intensity of the surface ablation cell without the flow deflector ring.

In the next run, the flow deflector ring was attached to the ablation cell with a 5.6 mm gap ($d = 5.6$ mm) between the ring and the end of the inner wall of the cell. The presence of this ring decreased the fluctuation of the output signal (Figure 8.2) by increasing the mixing efficiency of the gas flow inside the ablation cell and improving the homogeneity of the aerosol. But, the average signal intensity and the Relative Standard Deviation (RSD) were not affected. This ring also decreased the effective volume of the cell about 35 cm^3 . The average signal intensities and %STD for U238, Th23, and Si 29 are tabulated in Table 8.1.

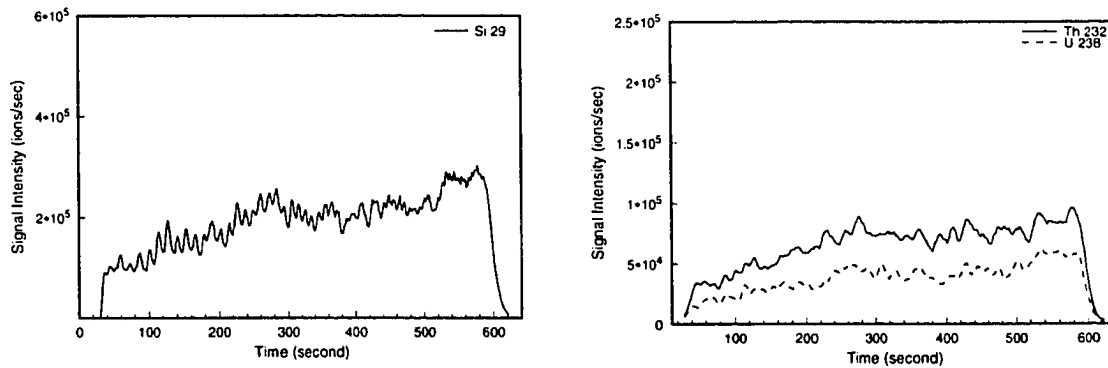


Figure 8.2: Signal intensity of the surface ablation cell with the flow deflector ring gap at 5.6 mm.

Table 8.1: The average signal intensity (counts/second)

Ring Gap (mm)		Unpacked Soil Sample			Packed Soil Sample		
		No Ring	5.6 mm Gap	1.2 mm Gap	No Ring	5.6 mm Gap	1.2 mm Gap
Si 29	Average	2.46×10^5	2.56×10^5	3.98×10^5	5.9×10^4	5.6×10^4	9.8×10^4
	RSD	35%	37%	30%	20%	25%	23%
Th 232	Average	7.3×10^4	7.9×10^4	1.50×10^5	6.2×10^3	5.3×10^3	8.8×10^3
	RSD	39%	42%	34%	28%	32%	28%
U 238	Average	4.5×10^4	5.1×10^4	1.07×10^5	3.4×10^3	3.2×10^3	5.6×10^3
	RSD	44%	45%	38%	33%	38%	33%

Finally, the ring gap was decreased to about 1.2 mm. This gap, which was the critical gap for this cell, significantly increased the mixing effect of the gas flow inside the cell. The magnitude of the output signal as shown in Figure 8.3, almost doubled without changing the laser power. This was a breakthrough in the surface ablation cell design. Because, without changing any other factors, the signal intensity of the ICP-MS was increased by a factor of two which improves the signal to noise ratio of the output signal.

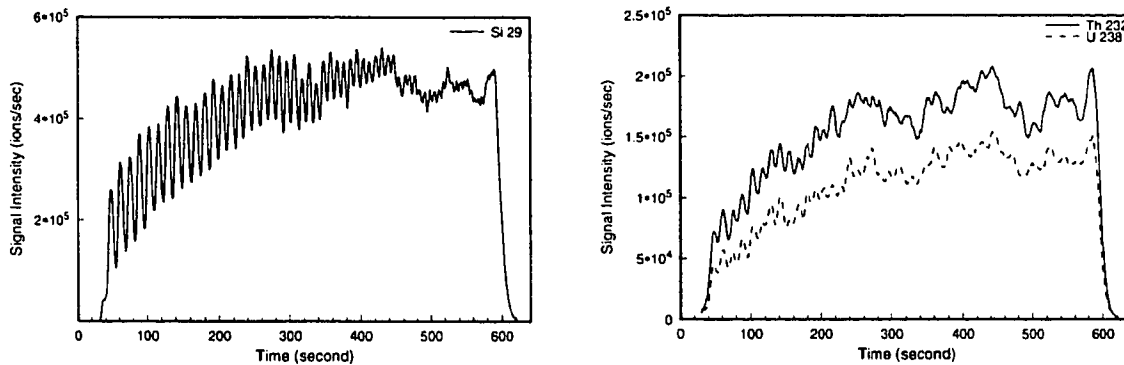


Figure 8.3: Signal intensity of the surface ablation cell with the flow deflector ring gap at 1.2 mm.

As explained in chapter 5, by increasing the gas velocity inside the ablation cell, the number of the very small particles ($< 1 \mu\text{m}$) entrained in the gas flow will increase. This increase in the number of small entrained particles in the aerosol, which is explained in section 8.3, was the main reason for this sharp increase in the output signal intensity.

In order to decrease the signal fluctuation due to the soil surface roughness, all the soil samples from this point on were packed prior to the ablation process. Figure 8.4 illustrates the effect of the flow deflector ring gaps on the signal intensities of Si 29, U 238, and Th 232 from the ICP-MS when the soil samples are packed. The average signal intensity and their relative standard deviation (RSD) are tabulated in Table 8.1. Packing the soil samples decreased the percentage of the Relative Standard Deviation (%RSD) of the output signal about 10% (see Table 8.1).

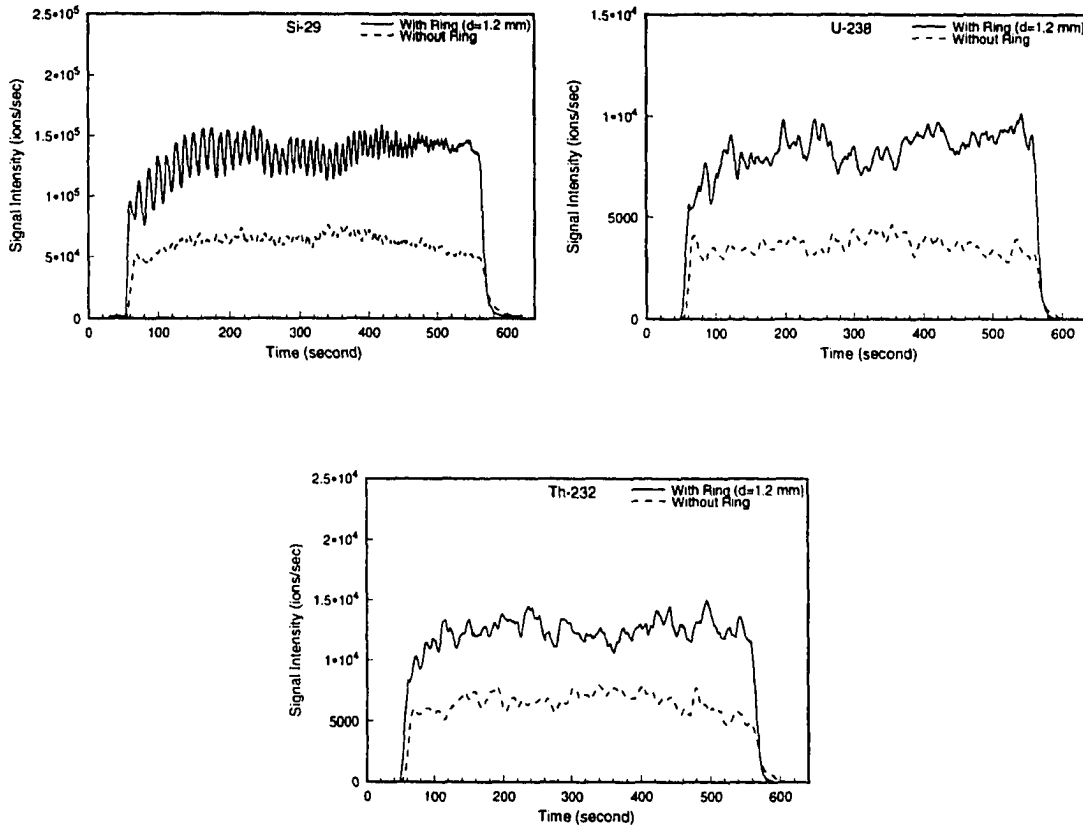


Figure 8.4: Signal intensities of the surface ablation cell for two different gap settings.

As shown in Figure 8.4, there is an oscillating signal with decreasing amplitude and increasing frequency superimposed on the output signal of Si 29 when the flow ring is used. The frequency of this oscillation is identical with the frequency of the rastering pattern. As the laser beam gets closer to the center of the spiral rastering pattern, the frequency of this oscillation increases and its amplitude decreases. The uneven flow of the aerosol through the two output ports was the main reason for such a behavior. In order to prove this, the oscillation of the output signal from an ablation cell (in which one of the two outlet ports was blocked) was compared to the output from the same cell with two outlet ports. This increased the amplitude of the oscillation by a factor of two while the frequency of the oscillation remained the same (Figure 8.5). Therefore, the main reason for this oscillation is the uneven flow through the

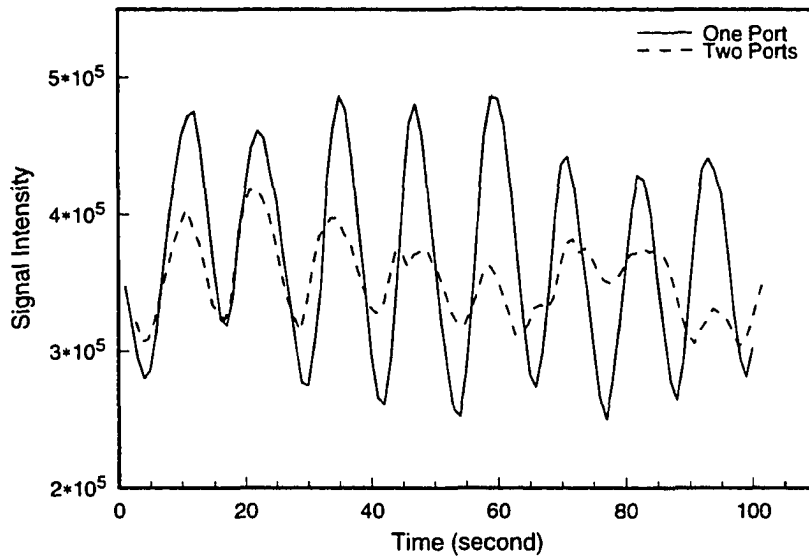


Figure 8.5: The output signal oscillation of the ablation cells with one and two output ports.

output ports. In an ideal situation (with equal flow), the amplitude of the oscillation would become zero. By increasing the number of the output ports from two to four or six, the amplitude of the oscillation decreases and this results in a lower STD.

8.1.1.2 Cell Volume Effect

The cell volume was increased by adding Plexiglas tubing of different heights to the bottom of the ablation cell. As shown in Figure 8.6, the increase in cell volume tends to dilute the aerosol, thus, decreasing the signal intensity. But this effect is not significant until the cell volume is nearly doubled. At this volume (268 cm^3), the signal intensity had decreased by about 20%.

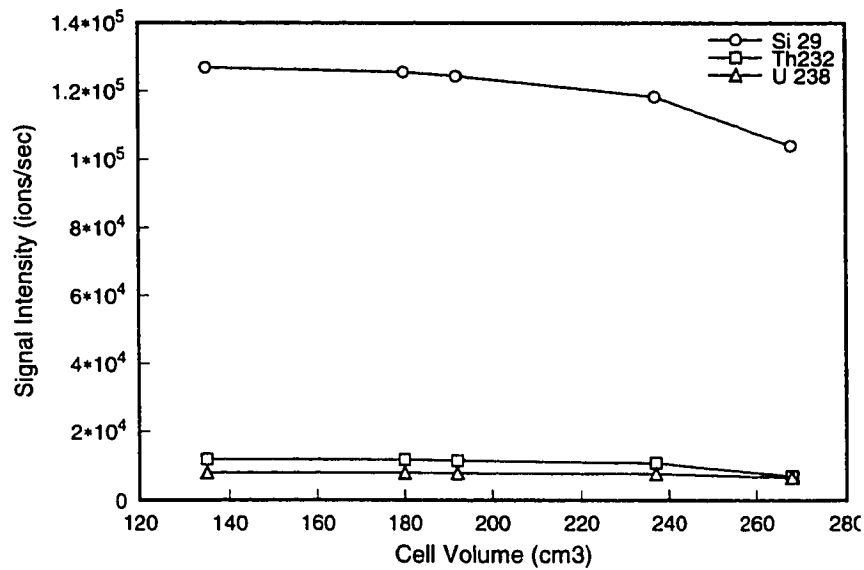


Figure 8.6: The effect of cell volume on the output signal intensity of the ICP-MS.

8.1.1.3 Flow Rate Effect

The effect of the inlet gas flow rate on the signal intensity of the ICP-MS was studied by incrementally increasing the gas flow rate to the ablation cell. To eliminate the effect of different factors such as laser power density and soil compaction that could affect the output signal from one run to another, the flow rate was increased from 0.9 to 1.3 l/min during an ablation process. As shown in Figure 8.7, the maximum signal intensity is achieved when the gas flow rate is 1.1 l/min. Although the change in the gas flow rate affects the gas velocity inside the cell and the transfer tube efficiency, it is not the main reason for changes in the signal intensity.

The residence time of the ablated particles in the plasma of the ICP torch is changed by adjusting the argon gas flow rate to the ICP-MS. High flow rate decreases the residence time of the particles, which could lower the efficiency of the ionization and disassociation of the particles in the plasma. On the other hand, lower flow rates could increase the residence time; therefore, increasing the efficiency of the ionization and disassociation of the ablated materials in the plasma. But, the ions may disperse away from the centerline of the sampler hole before

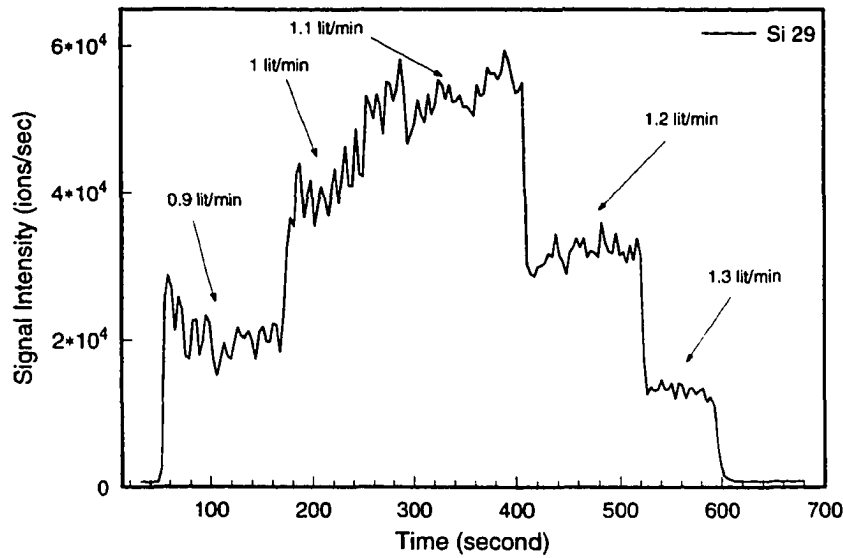


Figure 8.7: Effect of the argon gas flow rates on the output signal intensity of the ICP-MS.

reaching to the sampler. This could decrease the number of the ions passing through the sampler hole which results in low signal intensity. According to Horlick and Vaughan [27], the optimum flow rate for Ba⁺ ions using ICP-MS is about 1.2 liter/min. The optimum flow rate for the setup used in this study is 1.1 l/minute.

In order to study the effect of the flow deflector ring gap and gas flow rates effect at a different laser wavelength, a Nd-YAG laser beam with 1064 nm wavelength and 15 mj power was used to ablate the soil for a very short time. During these tests the laser beam was turned on for 2 seconds at different flow rates (0.8, 1.0, 1.2 l/min). As shown in Figure 8.8, the effect of the ring gap and flow rates on the signal intensities of the Si 29 are very similar to the previous experiments. The Si 29 signal intensity for this experiment increased by a factor of two and the optimum flow rate was 1.0 l/min.

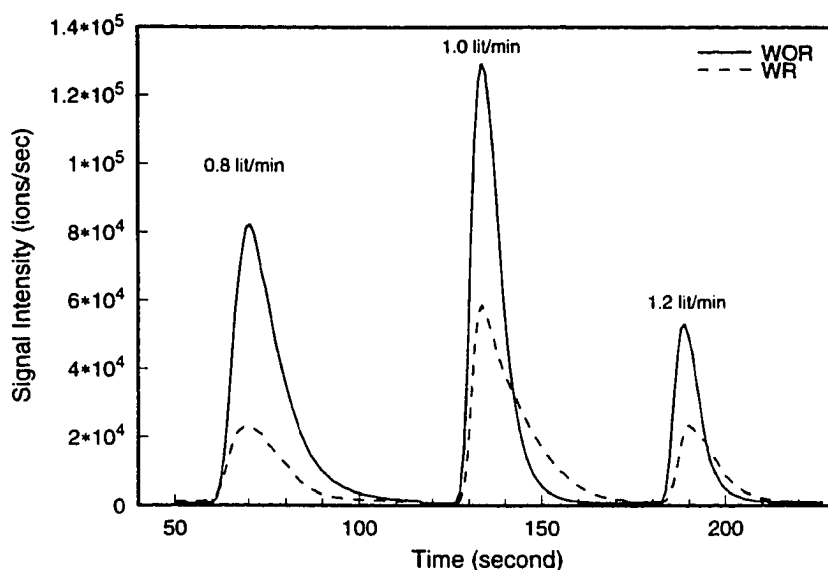


Figure 8.8: Effect of the deflector ring gap and argon gas flow rates on the output signal intensity of the ICP-MS with a different laser wavelength (1064 nm).

8.1.2 Sub-Surface Ablation Cell

In this experiment, a non-radioactive soil sample was used for laser ablation and the laser energy was delivered to the prototype sub-surface ablation cell by using a 100-foot long optic fiber optics. The soil sample was packed by using a small press to prevent soil collapse during the laser ablation process. A linear horizontal rastering pattern was selected for moving the laser beam across the soil surface.

8.1.2.1 Flow Deflector Channel Gap Effect

A typical signal profile of the sub-surface cell for different elements is shown in Figure 8.9. This signal is more uniform than the signal obtained from the surface ablation cell and its STD is less than the surface ablation cell. In this case, the soil was packed with a press and the surface of the soil sample was very smooth. Therefore, the signal profile did not have significant fluctuations due to the change in the topology of the soil surface. The linear rastering pattern was the second reason for a more stable output signal profile.

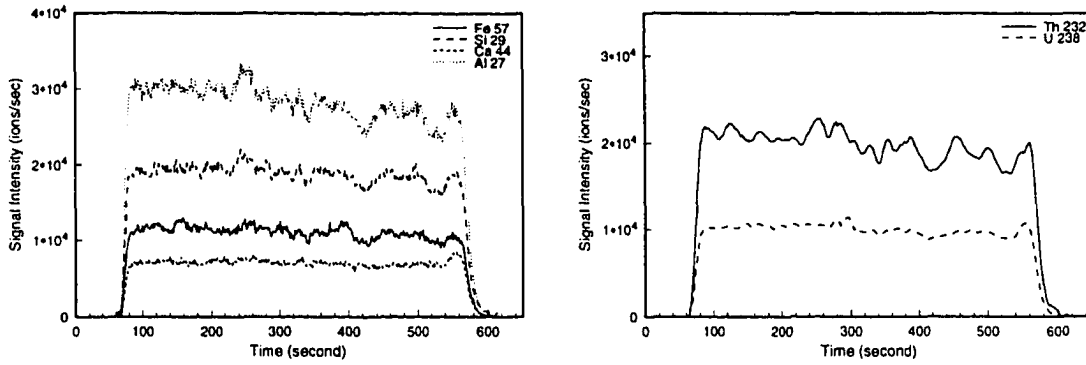


Figure 8.9: Signal intensity of the sub-surface ablation cell with the flow deflector channel opening of 3.2 mm.

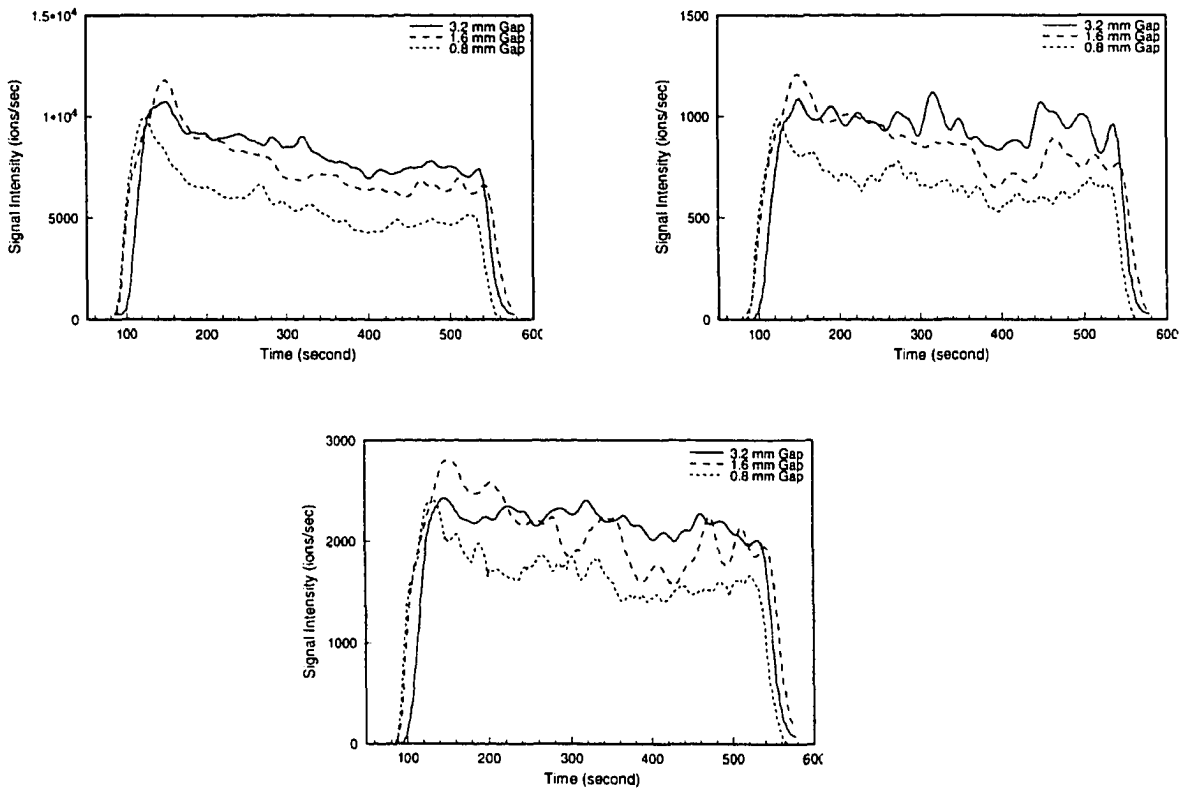


Figure 8.10: Signal intensity of the sub-surface ablation cell with the flow deflector channel opening heights of 3.2, 1.6, 0.8 mm: (a) Si 29, (b) U 238, (c) Th 232.

The effect of the flow deflector channel opening on the output signal intensity of the ICP-MS was studied by inserting two different size spacers in the channel opening and decreasing its height. The output signal from the ICP-MS for three different opening heights of 3.2, 1.6 and 0.8 millimeter were recorded. As shown in Figure 8.10, the overall signal intensity was decreased by changing the opening height. Of the sizes examined, the optimum flow channel height with 1 liter/minute gas flow rate was 3.2 mm.

8.1.2.2 Flow Rate Effect

In order to study the effect of the flow rate on the signal intensity of the sub-surface ablation cell, the flow of the inlet argon gas was increased gradually from 0.8 to 1.2 l/min during one ablation process. The delivered laser energy to the soil surface was 3.0 mj (refer to Figure 8.11). The optimum flow rate for the sub-surface ablation cell design was 0.8 l/min which is lower than the optimum flow rate for surface ablation cell.

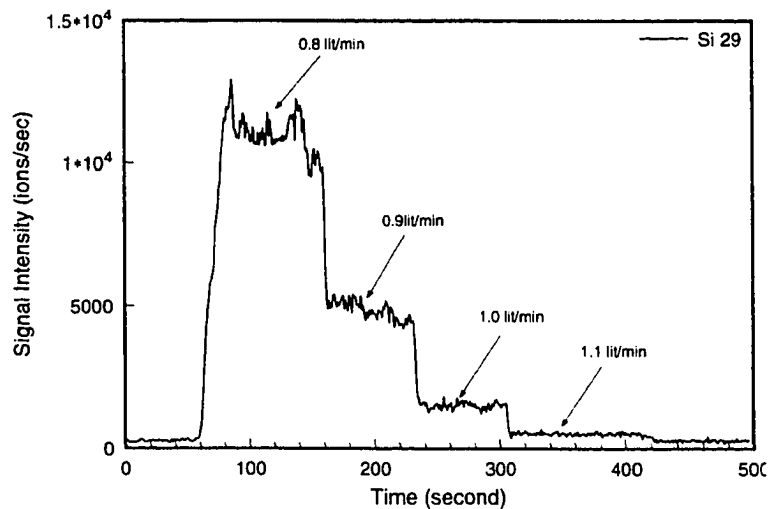


Figure 8.11: Effect of the argon gas flow rates in sub-surface ablation cell on the output signal intensity using the ICP-MS.

8.2. Ablation Cell Performance Using the ICP-AES

In this section, the performance of the surface ablation cell was studied using the ICP-AES setup in the MDLEST. The effect of the flow deflector ring gap, argon gas flow rate, and cell volume on the characteristics of the output signal from the ICP-AES are discussed. In order to increase the laser power delivered to the soil sample in the following experiments, a compact laser with the same wavelength, frequency, and pulse duration was mounted on the surface sampling probe. By using direct laser ablation (no fiber optics) and focusing the laser to a smaller spot size (100 μm), the laser power density on the surface of soil increased by a factor of 100. Two radionuclide standard soil samples (NRM5, NRM6) were used for laser ablation. The rastering pattern and speed was the same as when the ICP-MS was used. A typical profile of the output signal intensity for Si, U, and Th are shown in Figure 8.12. These signals are more stable and have less STD compared to the signals from the ICP-MS.

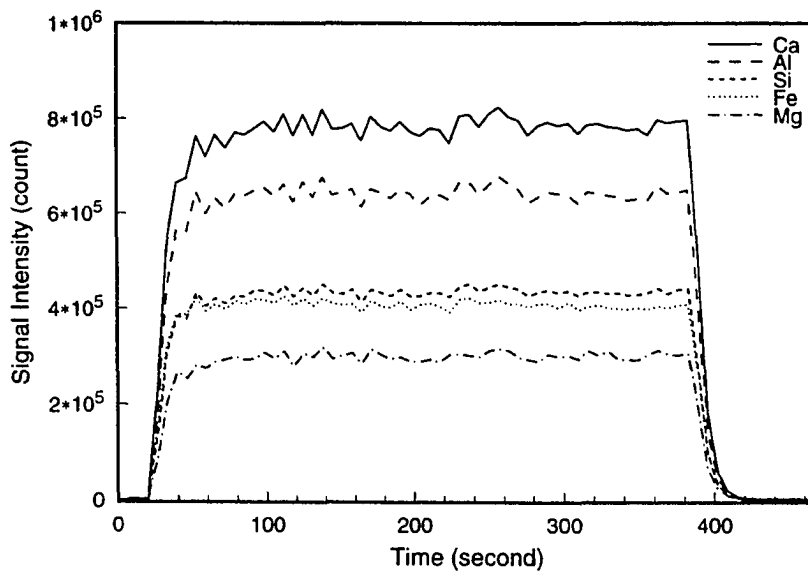


Figure 8.12: Typical output signal of the surface ablation cell using the ICP-AES.

8.2.1 Flow Deflector Ring Gap Effect

The effect of the flow deflector ring gap on the output signal intensity of the ICP-AES was investigated by adjusting the ring gap at six different settings. In the first series of tests, the laser power density on the surface of the soil samples was kept constant at 10^8 w/cm² by adjusting the focusing distance (Z axis). The effect of the flow deflector ring on the output signal intensity is depicted in Figure 8.13.

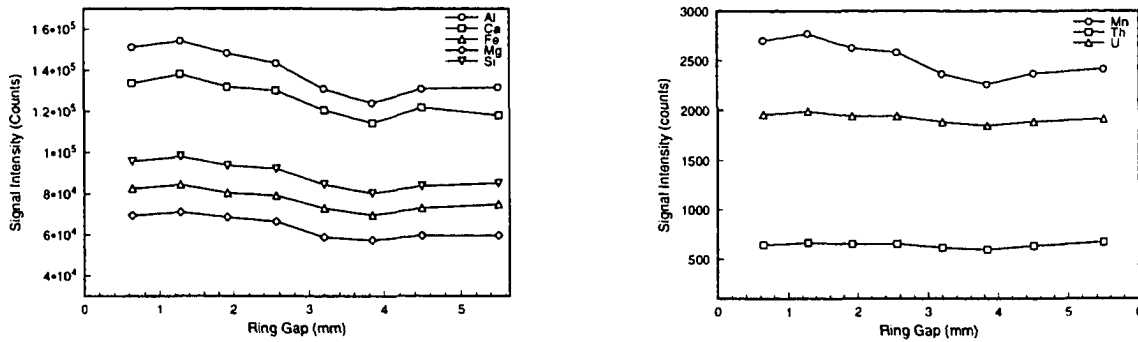


Figure 8.13: Signal intensity of the surface ablation cell with the flow deflector ring gap between 0.64 mm to 3.5 mm with 10^8 w/cm² laser power density.

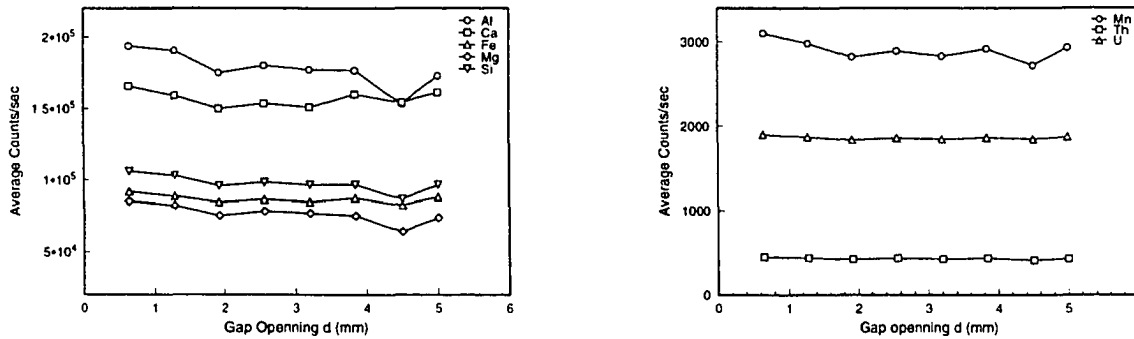


Figure 8.14: Signal intensity of the surface ablation cell with the flow deflector ring gap between 0.64 mm to 3.5 mm with 5×10^8 w/cm² laser power density.

In the second run, the laser power density was increased to $5 \times 10^8 \text{ w/cm}^2$ and results are shown in Figure 8.14.

By comparing Figures 8.13 and 8.14 with Figure 8.4, it is clear that the gain in the output signal intensity of ICP-AES is much less than the gain when the ICP-MS was used. The sensitivity of the output signal from the ICP-MS to the particle size is explained in section 8.3.

The effect of the flow deflector ring gap on the selectivity of the entrained ablated particles was investigated by calculating the ratio of the signal intensity of different elements (Al, Ca, Fe, Mg, Si, Th, and U) to Mn at different ring gap settings. Manganese (Mn) was selected as the reference element in calculating the signal intensity ratios, because it was used during the "Profiling" of the ICP-AES. The profiling is a procedure to optimize the performance of the polychromator in the AES.

The results are plotted as the signal intensity ratio of these elements versus the deflector ring gap opening (see Figure 8.15). The increase in the inlet gas flow velocity inside the ablation cell is a function of the deflector ring gap. As shown in Figure 8.15, the deflector ring did not had a significant effect on the selectivity of the entrained particles and the signal ratios of these elements remain constant at different ring gap settings.

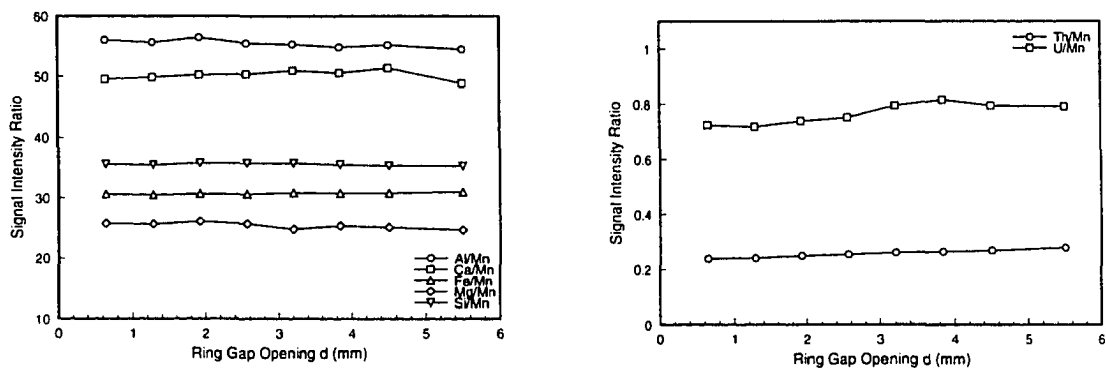


Figure 8.15: Effect of the deflector ring gap on the selectivity of the entrained ablated particles.

8.2.2 Cell Volume Effect

The cell volume effect on the output signal intensity of the ICP-AES was studied by adding Plexiglass tubes of different heights to the bottom of the ablation cell and keeping the laser power density constant. The laser power density was kept constant at about 2×10^8 w/cm² by adjusting the focusing distance (Z axis). Figure 8.16, shows the effect of cell volume change on the output signal intensity. Contrary to the common belief that increasing the cell volume would have strong effects on the signal intensity, the effect of aerosol dilution due to the cell volume was not significant until the cell volume was doubled. At this volume (268 cm³), the drop in the signal intensity for most elements was about 15%.

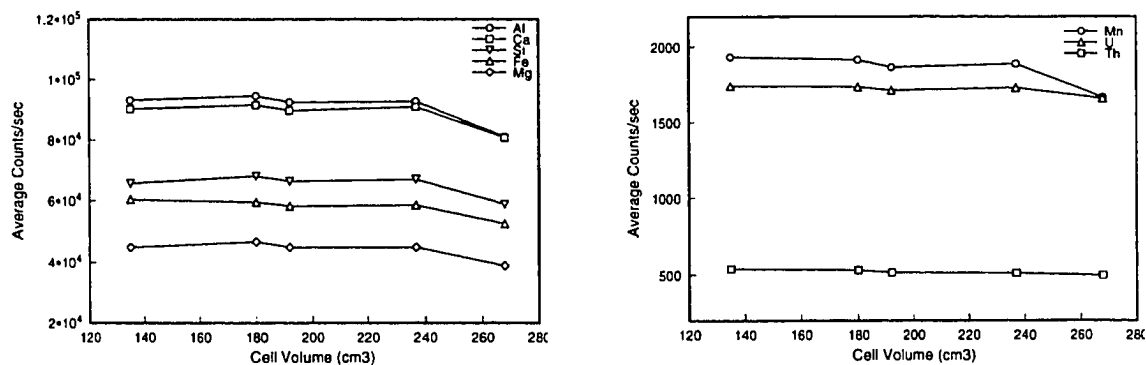


Figure 8.16: The effect of cell volume on the output signal intensity of the ICP-AES.

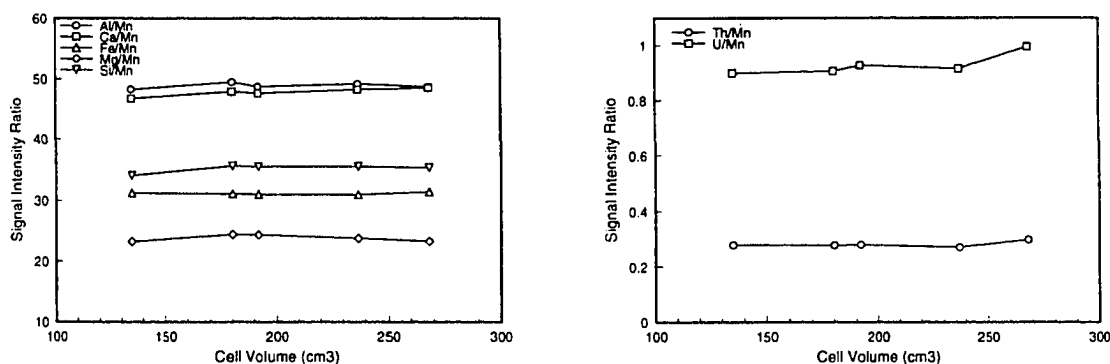


Figure 8.17: Effect of the cell volume on the selectivity of the entrained ablated particles.

The effect of the cell volume on the selectivity of the entrained ablated particles is illustrated in Figure 8.17. As shown in this figure, the signal intensity ratio does not depend on the cell volume.

8.2.3 Gas Flow Rate Effect

The inlet argon gas flow rate has a very significant effect on the signal intensity of the ICP-AES. This is shown in Figure 8.18, by increasing the inlet flow rate from 0.8 to 1.2 l/min during an ablation process. As explained in section 8.1.1.3, the main reason for this effect is the residence time of the ablated particles in the ICP plasma.

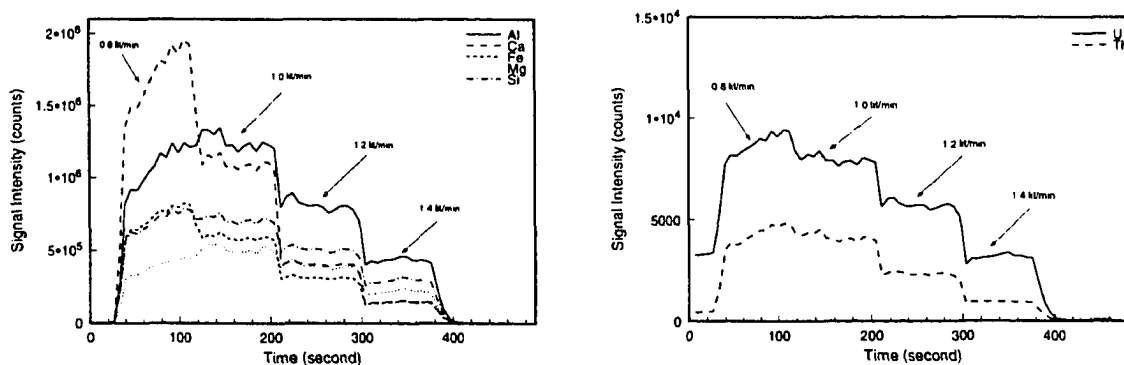


Figure 8.18: The gas flow rate effect on the output signal intensity of the ICP-AES.

8.3. Particle Size Distribution Study

To find the main cause of a very sharp increase in the signal intensity of the ICP-MS but moderate increase in the signal intensity of the ICP-AES, a particle size analysis was conducted using a Scanning Electronic Microscope (SEM) and Image Analyzer. In this experiment, when the laser ablation was in process, a small amount of the aerosol sample was collected on a gold plated polycarbonate filter for 5 seconds. Each sample was collected exactly 3 minutes after the beginning of the laser ablation. Two samples were collected for each deflector ring gap setting. These filters were then photographed by the SEM. Six photographs

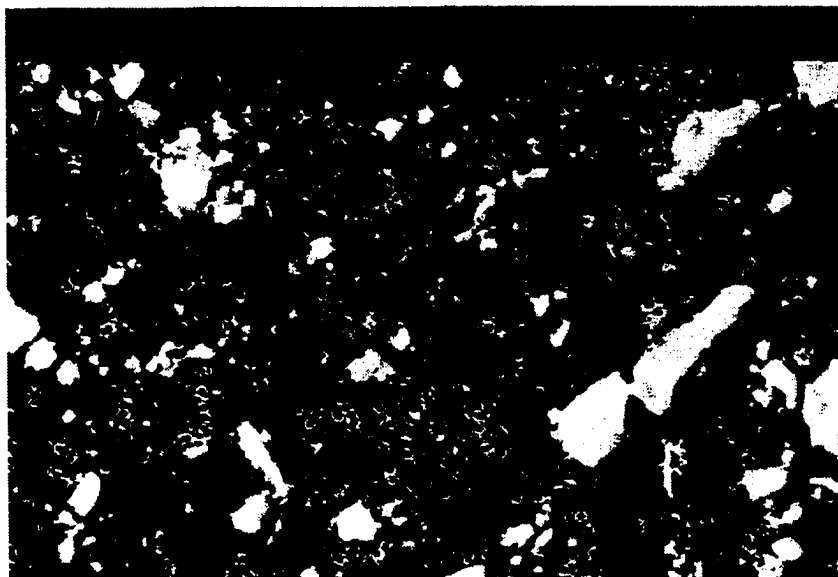


Figure 8.19: SEM photograph of aerosol sample on gold plated filter.

were taken from each sample at three different fixed positions (Figure 8.19).

The photographs taken by the SEM were later analyzed by an image analyzer. The information regarding each particle such as: minimum and maximum diameters, area, perimeter, and the equivalent diameter of the circle with the same area were all extracted from each picture. These data were analyzed by using a spreadsheet program to determine the particle size distribution of the ablated particles for each gap setting.

The summary of the results is tabulated in Table 8.2 and the particle size distribution for different deflector ring gap is shown in Figure 8.20. The number of total particles on the sample collected with deflector ring gap of 1.28 mm, is about 16% more than when the ring was not used. In this experiment, because of the size of the pores on the filter (0.1 μm) and resolution of the image analyzer, the minimum measurable particle size was 0.2 μm . Thus, by considering the results from the ICP-MS it is expected that the increase in the number of the particles smaller than 0.2 μm will be significantly more than 16%.

Table 8.2: Particle size distribution of the entrained particles in the aerosol

Particle Dia. (μm)	Without Deflector		With Deflector $d = 0.64 \text{ mm}$		With Deflector $d = 1.28 \text{ mm}$		With Deflector $d = 1.92 \text{ mm}$	
	Particle No.	%	Particle No.	%	Particle No.	%	Particle No.	%
0	0	0	0	0	0	0	0	0
0.1 - 0.5	296	46.3	352	53.3	399	54.1	297	52
0.6 - 1.0	179	28.0	169	25.6	191	25.9	161	28.1
1.1 - 1.5	81	12.7	72	10.8	71	9.7	53	9.3
1.6 - 2.0	33	5.1	30	4.5	33	4.5	28	4.8
2.1 - 2.5	17	2.7	15	2.2	18	2.4	15	2.7
2.6 - 3.0	13	2.0	10	1.5	8	1.1	7	1.2
3.1 - 3.5	8	1.2	6	1.0	8	1.1	7	1.2
3.6 - 4.0	5	0.8	2	0.3	6	0.8	3	0.5
4.1 - 4.5	5	0.8	1	0.2	4	0.5	2	0.4
4.6 - 5.0	0	0.0	3	0.5	1	0.1	0	0.0
5.1 - 5.5	0	0.0	1	0.2	0	0.0	0	0.0
5.6 - 6.0	2	0.3	0	0.0	0	0.0	1	0.2
6.1 - 6.5	1	0.2	0	0.0	0	0.0	0	0.0
6.6 - 7.0	0	0.0	0	0.0	0	0.0	0	0.0
Total No.	638	100	660	100	737	100	571	100

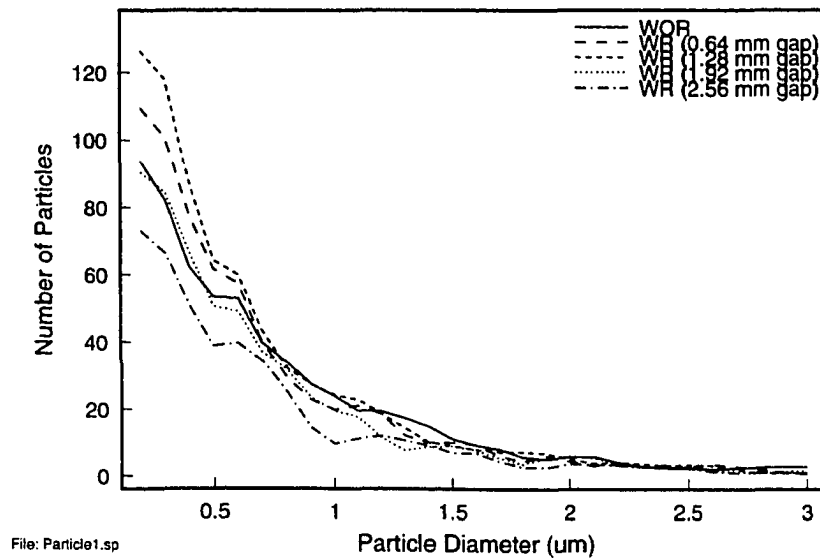


Figure 8.20: Particle size distribution of the generated aerosol inside the surface ablation with different gas flow deflector ring gap settings.

The average particle size and mass distributions of these sample are shown in Figures 8.21 and 8.22 respectively. According to these results main portions (%93) of the ablated particles leaving the ablation cell have diameters less than 2 μ m. This portion of the ablated particles represents only %22 of the total mass of the entrained particles.

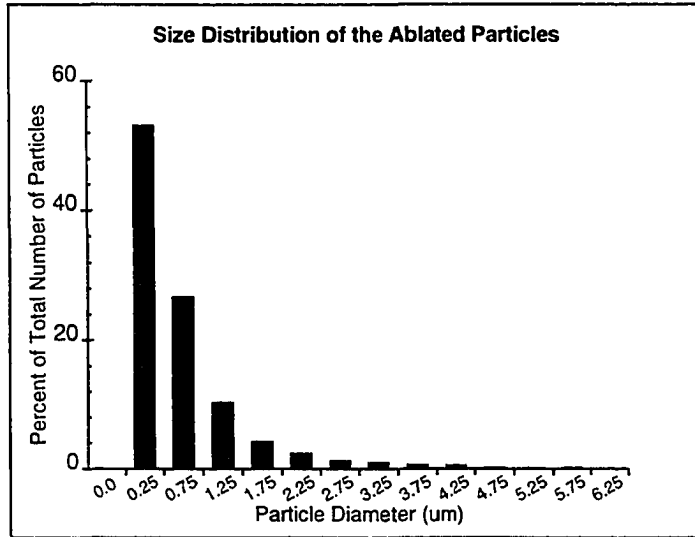


Figure 8.21: Percentage of the particle size distribution.

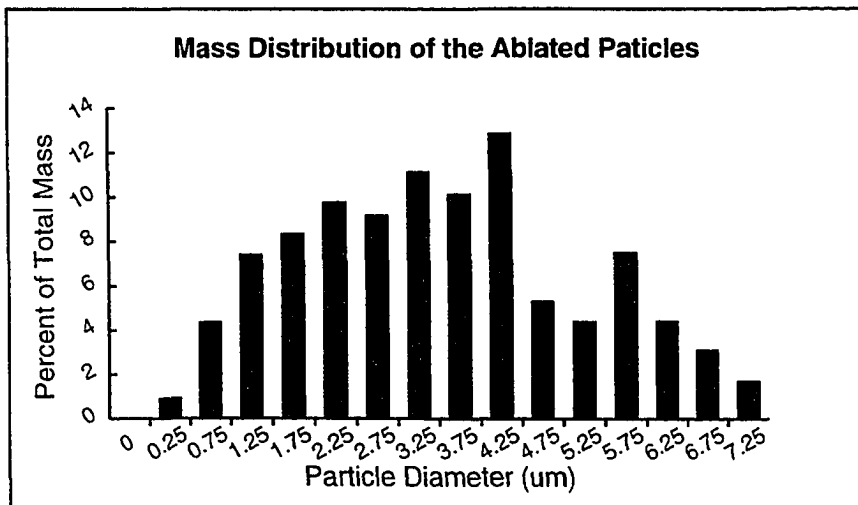


Figure 8.22: Percentage of the particle mass distribution

As shown in Figure 8.23, the main reason for the increase in the number of very small particles ($< 2 \mu\text{m}$) entrained by the ablation cell with deflector ring is the argon gas flow interaction with the particles generated during the ablation process. The flow of argon gas with velocity of V_e applies a secondary drag force (F_{D2}) on the ablated particles. Sum of this drag force with the drag force due to the initial ejection (F_{D1}) of the ablated particles applies a relatively large magnitude downward drag force on these particles. The resultant drag force prevents the upward motion of the ablated particles. Due to the mass of the big particles, this force will be higher for large particles and deposit them inside the cell by impacting them to the soil surface and preventing them from being entrained in the argon gas stream. On the other hand, since the small particles have very short stopping distance (see Appendix A), the flow of argon gas helps the small particles to be entrained and prevents them from depositing due to the gravity forces. Therefore, the net result of adding the deflector ring is an increase in the number of very small particles ($< 2 \mu\text{m}$) and a more homogeneous aerosol generation due to the mixing effect of the argon gas flow inside the cell.

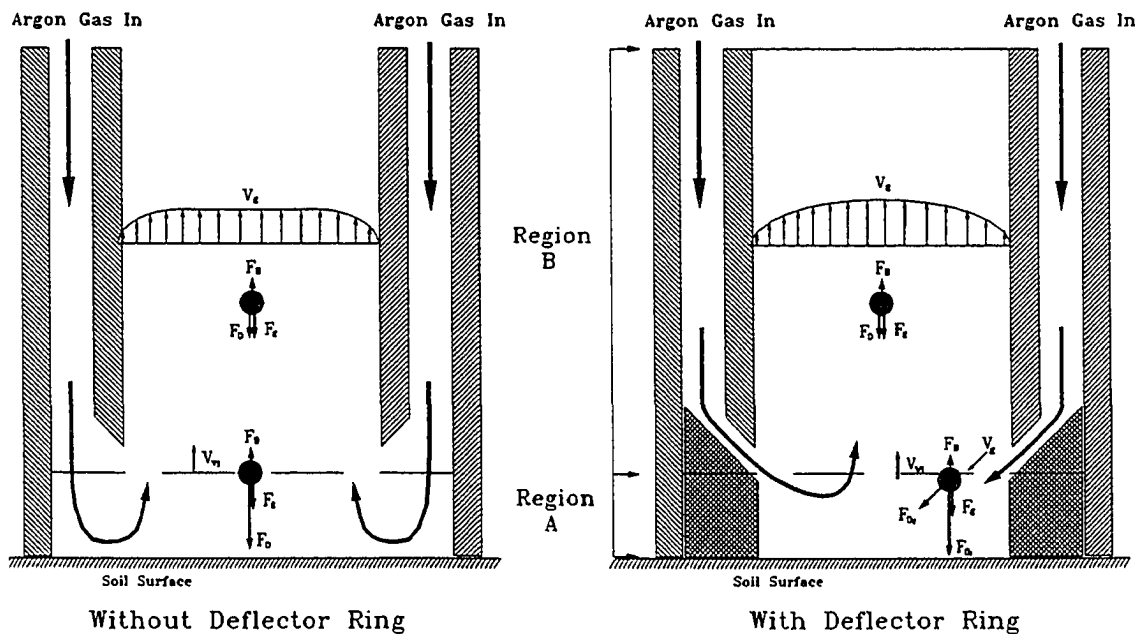


Figure 8.23: Particle entrainment inside the ablation cell

Most of the relatively large particle ($> 3 \mu\text{m}$ in diameter) were deposit inside the 100-foot long Tygon tubing before reaching to the ICP. Therefore, the increase in the number of a very small ablated particle in the aerosol reaching the ICP-MS could be the main reason for the sharp increase in the output intensity of this instrument. These small particles have a higher chance of complete disassociation and ionization when they are inside the ICP-MS torch. The increase in the number of ions passing through the sampler cone will increase the output signal intensity. Because of the geometry of the sampler cone in the ICP-MS, this instrument is more sensitive to the size of ablated particles reaching the torch. This explains the use of the cyclone particle separator for solid sample and the double pass spray chamber for the liquid sample (nebulizer) introduction into the ICP-MS [34].

In contrast to the ICP-MS, the ICP-AES is less sensitive to the particle size of the materials reaching the ICP torch. In the ICP-AES, the light emitted from the plasma is collected by a 6-10 mm long and 0.1 mm wide vertical entrance slit. This means that the emitted light from the plasma reaching the photomultiplier tube is the average over a 6-10 mm long vertical distance of the entrance slit. This increases the residence time of the particles in the plasma and their emission will be collected at the entrance slit. Therefore, a wider range of particles could be completely disassociated with this increased residence time and the instrument would be less sensitive to the particle size.

CHAPTER 9. CONCLUSION AND RECOMMENDATION

The increasing awareness and concern about our environment has created a tremendous pressure on different companies and organizations (which are responsible for contamination of the environment by storing their by product waste at different site) to clean up the contaminated sites. Site characterization of a contaminated site is the first and a very critical step in the clean up program. During this process, all the necessary information about location, level, and chemical composition of the contaminated sites are collected for the clean up planning. Thus, field-deployable analytical instruments to detect contaminants in a short period of time at different sites are the key elements in site characterization process.

The LA-ICP-AES/MS techniques were adopted and developed at Ames Laboratory, a DOE laboratory, to build a field-deployable analytical mobile lab (MDLEST) for site characterization of the radio-active contaminated sites. The robotic surface sampling accessory (RSA) with its sampling probe and the MDLEST are a practical setup for a safe, fast, and cheap soil analysis without exposing the operators to the hazardous radio-active wastes. The objectives of this work were to design, built, and test surface and subsurface ablation cells, as a part of the sampling probe, for soil sample collection using a laser ablation (LA) technique. The conclusion of this study and recommendations for future work are summarized in the following sections.

9.1 Conclusion

To accelerate the final design selection and minimize the design cost, five different Plexiglass model cells were designed and built to conduct the preliminary flow analysis inside the cell. The flow patterns inside these cells were recorded by a high-speed camcorder.

Considering the results obtained during the flow observation of the flow behavior in these cells, two optimum cell designs for surface and sub-surface ablation cell were selected. Based on these designs, the drawings for manufacturing the individual components of each cell were prepared and two prototype surface and sub-surface ablation cells were built.

The performance of the prototype cells were thoroughly investigated by running a series of tests using ICP-MS, ICP-AES, SEM, and image analysis. Both cells had a short flushing time (about 12 seconds) and good mixing characteristics. Thus, the signal fluctuation due to the change in the aerosol density was minimum. The quartz window in both cells remained clean up to 8 hours of operation. The laser power loss due to the scattering of the laser beam by ablated particles was minimum. The percent of relative standard deviations (RSD%) of the output signal intensities of the ICP-AES/MS for surface ablation cell were 14% and 30% respectively. The effect of the deflector ring, which is a unique and important part of the surface ablation cell, and different parameters such as inlet gas flow rate, cell volume, and transfer tube length are all summarized in the reminder of this section.

The mixing characteristics of the gas flow at the lower section of the cell was increased by adding a deflector ring to the ablation cell. This effect enhanced the aerosol quality by increasing its homogeneity and the number of the small particles entrained in the aerosol. This had a very significant effect on the output signal intensity of the ICP-MS. Depending on the deflector ring gap setting, the signal intensities of some of elements (U, Th) were increased by a factor of two. The main reason for this noticeable increase in the signal intensity, as explained in the image analysis section, was an increase (about 10%) in the number of the measurable small entrained particles ($0.2 < d_p < 0.5 \mu\text{m}$) in the aerosol. But, when the deflector ring was used during the ICP-AES analysis, the increase in the output signal intensity was moderate (10-20%). Because, the ICP-AES is less sensitive to the size of the particles transferred to the ICP.

The inlet argon gas flow rate, within the acceptable range (0.8 - 1.2 l/min) for the ICP-AES/MS, did not have a significant effect on the entrainment of the ablated particles in the cell or the transfer tube efficiency. The relation between the maximum size of the entrained ablated particles inside the ablation cell and the gas flow rate is given by the mathematical model developed for predicting entrainment efficiency of the ablation cell. According to this model, an increase in the inlet gas flow rate from 0.8 to 1.2 l/min, increases the maximum entrained

particle diameter from 9.8 to 12.2 μm . Also, the same variation in the flow rate could increase the maximum transferred particle diameter to the ICP from 1.4 to 1.8 μm using a 100-foot long tube. On the other hand, increasing the inlet gas flow rate had a significant effect on the output signal intensity of both ICP-MS and ICP-AES. Increasing the flow rate decreases the residence time of particles inside the ICP and this has a very important effect on the efficiency of the and dissociation, atomization, and ionization of the particles in the ICP.

The increase in the cell volume tends to decrease the signal intensity of the both ICP-AES and ICP-MS units. But this effect was not significant until the cell volume was nearly doubled. At this volume the signal intensity of both units had decreased by about 20%.

The amount of transferred particles to the ICP could be controlled by adjusting the gas flow rate, cell dimensions, and transfer tube length. The maximum particle size that could be entrained in the aerosol depends on the cell diameter, gas flow rate, gas viscosity, and particle density. Therefore, it is possible to set an upper limit for the maximum size of the entrained particle diameter by adjusting the gas flow velocity. The tube length and diameter are two important factors that influence the particle sizes transferred to the ICP. The longer the tube, the smaller the particle diameter transferred.

According to the results obtained from the SEM and image analysis, 93% of the number of the entrained particles from the laser ablation of the NRM5 and NRM6 samples have diameter less than 2 μm . The total mass of this portion of the ablated particles is only 22% of the total mass of the entrained particles.

9.2 Recommendations

As a result of this study, several issues have been encountered which are very important in improving the overall performance of the LA-ICP-AES/MS techniques used for elemental analysis. Following are recommendations for the further investigations:

- Soil is a non-homogeneous sample and this has a very important effect on the characteristic of the output signal. Design and fabrication of a device for in situ soil sample preparation prior to testing could have a significant effect on the quality and quantity of the signal.

- Understanding the laser interaction with soil and the parameters that can effect the laser ablation process is critical for solid-sample collection by the laser. Factors such as laser wavelength, laser frequency, laser power density, laser pulse duration, soil moisture content, soil compaction, and soil type are all detrimental in the ablation process. Thus, further research in this area is essential in order to characterize and optimize the effect of these parameters on the laser ablation process.

BIBLIOGRAPHY

- [1] Jenkins, T. "Hazardous Waste Cleanup: How Much and Who will Pay?" *Walker's Estimating and Construction Journal*, pp. 6-7, Fall 1989.
- [2] Pasternok, D. "The \$200 Billion Scandal at the Bomb Factories." *U.S. News & World Report*, pp. 34-37, December 14, 1992.
- [3] Huie, C. W.; Yeung, E. S. "Spatial and Temporal Distributions of Particulates Formed from Metallic Surfaces by Laser Vaporization." *Anal. Chem.*, 58, pp. 1989-1993, 1986.
- [4] D'Silva, A. P.; Zamzow, D.; Jaselskis, E. J.; Weeks, S. "Remote, Real-Time Analysis of Hazardous Waste Through Laser Ablation-Inductively Coupled Plasma-Atomic Emission Spectrometry." *Pro. Spectrum*, 1, pp. 409-413, 1992.
- [5] Arrowsmith, P. "Laser ablation of Solids for Elemental Analysis by Inductively Coupled Plasma Mass Spectrometry." *Anal. Chem.*, 59, pp. 1437-1443, 1987.
- [6] Arrowsmith, P.; Hughes, S. K. "Entrainment and Transport of Laser Ablated Plumes for Subsequent Elemental analysis." *Applied Spectroscopy*, 42, pp. 1231-1239, 1988.
- [7] Fassel, V. A. "Quantitative Elemental Analysis by Plasma Emission Spectroscopy." *Science*, 202, pp. 183, 1978.
- [8] Arrowsmith, P. "Application of Laser Ablation: Elemental Analysis of Solids by Secondary Plasma Source Mass Spectrometry." In *Laser and Mass Spectrometry*, ed. David M. Lubman, pp. 180-204, Oxford University Press, New York, NY, 1990.
- [9] Dickinson, G. W.; Fassel, V. A. "Optimization of Argon Flow in the ICP-AES." *Anal. Chem.*, 41, pp.1021. 1969.
- [10] Beuermann, T.; Brinkmann, H. J.; Damm, T.; Stuke, M. "Picosecond UV Excimer Laser Ablation of LiNbO₃." *Mat. Res. Soc. Symp. Proc.*, 191, pp. 37-42, 1990.

- [11] Dreyfus, R. W. "Comparison of the Ablation of Dielectrics and Metals at High and Low Laser Powers." In Laser Ablation Of Electronic Materials Basic Mechanisms and Applications, ed. Fogarassy, E.; Lazare, S., Elsevier Science Publishers B. V., New York, NY, 1992.
- [12] Eloy, J. F. "5th Intern. Symp. High Purity Material in Science and Technology", Dresden, Proc. II, 96, 1980.
- [13] Buringham, R. A.; Salter, P. L. "Analysis of Solid Materials by Laser Probe Mass Spectrometry." *Anal. Chem.*, 48, p. 1735, 1976.
- [14] Chun, M. K.; Rose, K. "Interaction of High-Intensity Laser Beam with Metals." *J. Appl. Phys.*, 41, pp. 614, 1970.
- [15] Pang, H. M.; Wiederin, D. R.; Houk, R. S.; Yeung, E. S. "High-Repetition-Rate Laser Ablation for Elemental Analysis in an Inductively Coupled Plasma with Acoustic Wave Normalization." *Anal. Chem.*, 63, pp. 390-394, 1991.
- [16] Gray, A. L. "Solid Sample Introduction by Laser Ablation for Inductively Coupled Plasma Source Mass Spectrometry." *Analyst*, 110, pp.551-556, 1985.
- [17] Scott, R. H.; Fassel, V. A.; Kniseley, R. N.; Nixon, D. E. "Analysis of Solid Materials by ICP-AES." *Anal. Chem.*, 46, pp. 75, 1974.
- [18] Skogerboe, R. K.; Coleman, G. N. "Microwave Plasma Emission Spectrometry." *Anal. Chem.*, 48, pp. 611A-22A, 1976.
- [19] Ishizuka, T.; Uwamino, Y. "Inductively Coupled Plasma Emission Spectrometry of Solid Samples by Laser Ablation." *Spectrochimica Acta*, 38B, pp. 519-527, 1983.
- [20] Broek, W. M.; Galan, L. "Supply and Removal of Sample Vapor in Graphite Thermal Atomizers." *Anal. Chem.*, 49, pp. 2176, 1977.
- [21] Thompson, M.; Barnes, R.M. "Analytical Performance of Inductively Coupled Plasma-Atomic Emission Spectrometry." In Inductively Coupled Plasmas in Analytical Atomic Spectrometry 2nd ed., Montaser, A.; Golightly, D. W., pp. 249-298, VCH Publishers Inc., New York, NY, 1992.
- [22] Cameron, W. M.; Routh, M. W.; Tikkanen, M. W. "Introduction of Solids into Plasmas." In Inductively Coupled Plasmas in Analytical Atomic Spectrometry 2nd ed., Montaser, A.; Golightly, D. W., pp. 721-780, VCH Publishers Inc., New York, NY, 1992.

- [23] Chenry, S.; Hunt, A.; Thompson, M. "laser Ablation of Minerals and Chemical Differentiation of the Ejecta." *Journal of Analytical Atomic Spectrometry*, 7, pp. 647-652, 1992.
- [24] Thompson, M.; Goulter, J. E.; Sieper, F. "Laser Ablation for the Introduction of Solid Samples into an Inductively Coupled Plasma for Atomic-Emission Spectrometry." *Analyst*, 106, pp.32-39, 1981.
- [25] Ishizuka, T.; Uwamino, Y. "Atomic Emission Spectrometry of Solid Samples with Laser Vaporization-Microwave Induced Plasma System" *Anal.Chem.*, 52, pp.125-129, 1980.
- [26] Mitchell, P. G.; Sneddon, J.; Radziemski, L. J. "Direct Determination of Copper in Solids by Direct Current Argon Plasma Emission Spectrometry with sample Introduction Using Laser Ablation." *Applied Spectroscopy*, 41, pp. 141-148, 1987.
- [27] Reist, P. C. Aerosol Science And Technology 2nd ed., McGraw-Hill Inc., New York, NY, 1993.
- [28] Hesketh, H. E. Fine Particles In Gaseous Media 2nd ed., Lewis Publisher Inc, Chelsea, MI, 1986.
- [29] Waldmann, L. *Naturforsch*, 14A, pp. 589, 1960.
- [30] Millikan, P., *Phys. Rev.*, 21, pp. 217, 1923.
- [31] Cunningham, E., *Proc. Roy. Soc.*, 83 A, pp. 357, 1910.
- [32] Fuchs, N. A. "The Mechanics Of Aerosols" Pergamon Press, Oxford, 1964.
- [33] Thomas, J. E. "Gravity Settling of Particles in a Horizontal Tube," *J. Air Poll. Control Assoc.*, 8(1), pp. 32-34, 1958.

APPENDIX A. THEORETICAL RESULTS OF THE PARTICLE MOTION IN THE ABLATION CELL

The theoretical values (at standard conditions) for the particle Cunningham correction factor (C_C), coefficient of drag (C_D), and relaxation time (τ) for the particle diameter (D_P) range between 0.01 - 30 μm at different particle size regions are calculated. The particle Reynolds numbers (Re_P) for different particle diameters with initial velocities of 1000 and 10,000 cm/sec are calculated. Then by using these values and based on the nature of the particle motion (laminar or turbulent), the terminal settling velocity (V_S), and stop distance (X_S) for each particle size are given. The results for the particle motion inside the surface ablation cell and the transfer line are as follow:

D_P (μm)	C_C	C_D		τ (sec)	Re_P	
		$V_i=1000$ cm/s	$V_i=10000$ cm/s		$V_i=1000$ cm/s	$V_i=10000$ cm/s
0.01	33.31	2985	298	2.2e-08	0.01	0.0804
0.02	16.95	1490	149	4.5e-08	0.02	0.161
0.03	11.51	995	99.52	6.9e-08	0.02	0.241
0.04	8.79	747	74.7	9.3e-08	0.03	0.321
0.05	7.16	597	59.7	1.2e-07	0.04	0.402
0.06	6.08	497	49.7	1.5e-07	0.05	0.482
0.07	5.31	426	42.6	1.7e-07	0.06	0.563
0.08	4.74	373	37.3	2e-07	0.06	0.643
0.09	4.29	331	33.1	2.3e-07	0.07	0.723
0.1	3.94	298	29.8	2.6e-07	0.08	0.804
0.2	2.37	149	14.9	6.3e-07	0.16	1.61
0.3	1.88	99	9.95	1.1e-06	0.24	2.41
0.4	1.64	74	7.47	1.7e-06	0.32	3.21
0.5	1.51	59	5.97	2.5e-06	0.4	4.02
0.6	1.42	49	4.97	3.4e-06	0.48	4.82

0.7	1.36	42	4.26	4.4e-06	0.56	5.63
0.8	1.31	37.3Z	3.73	5.6e-06	0.64	6.43
0.9	1.28	33.2	3.31	6.9e-06	0.72	7.23
1	1.25	29.8	2.98	8.3e-06	0.8	8.04
1.1	1.23	27.1	2.71	9.8e-06	0.88	8.84
1.2	1.21	24.9	2.48	1.2e-05	0.96	9.64
1.3	1.19	23.1	2.30	1.3e-05	1	10.4
1.4	1.18	21.2	2.12	1.5e-05	1.1	11.3
1.5	1.17	19.8	1.98	1.7e-05	1.2	12.1
1.6	1.16	18.6	1.86	2e-05	1.3	12.9
1.7	1.15	17.5	1.75	2.2e-05	1.4	13.7
1.8	1.14	16.5	1.65	2.4e-05	1.4	14.5
1.9	1.13	15.7	1.56	2.7e-05	1.5	15.3
2	1.12	14.9	1.49	3e-05	1.6	16.1
3	1.08	9.95	0.99	6.5e-05	2.4	24.1
4	1.06	7.47	0.74	0.00011	3.2	32.1
5	1.05	5.97	0.59	0.00017	4	40.2
6	1.04	4.98	0.49	0.00025	4.8	48.2
7	1.04	4.26	0.42	0.00034	5.6	56.3
8	1.03	3.73	0.37	0.00044	6.4	64.3
9	1.03	3.31	0.33	0.00055	7.2	72.3
10	1.02	2.98	0.29	0.00068	8	80.4
11	1.02	2.71	0.27	0.00082	8.8	88.4
12	1.02	2.45	0.24	0.00097	9.6	96.4
13	1.02	231	0.23	0.0011	10.4	104
14	1.02	2.12	0.21	0.0013	11.3	113
15	1.02	1.98	0.19	0.0015	12.1	121
16	1.02	1.86	0.18	0.0017	12.9	129
17	1.01	1.75	0.17	0.0019	13.7	137
18	1.01	1.65	0.16	0.0022	14.5	145
19	1.01	1.56	0.15	0.0024	15.3	153
20	1.01	1.49	0.14	0.0027	16.1	161
22	1.01	1.35	0.13	0.0032	17.7	177
24	1.01	1.24	0.12	0.0039	19.3	193
26	1.01	1.15	0.11	0.0045	20.9	209
28	1.01	1.07	0.10	0.0052	22.5	225
30	1.01	0.99	0.09	0.006	24.1	241

D _p (μm)	V _s (cm/sec)	X _s (cm)	
		V _i =1000 cm/s	V _i =10000 cm/s
0.01	0.000721	2.21e-05	0.000221
0.02	0.000747	4.5e-05	0.00045
0.03	0.000775	6.87e-05	0.000687
0.04	0.000804	9.33e-05	0.000933
0.05	0.000834	0.000119	0.00119
0.06	0.000866	0.000145	0.00145
0.07	0.000899	0.000173	0.00173
0.08	0.000934	0.000201	0.00201
0.09	0.00097	0.000231	0.00231
0.1	0.00101	0.000261	0.00261
0.2	0.00146	0.000629	0.00629
0.3	0.00206	0.00112	0.0112
0.4	0.0028	0.00174	0.0174
0.5	0.00369	0.0025	0.025
0.6	0.00471	0.00339	0.0339
0.7	0.00587	0.00441	0.0441
0.8	0.00716	0.00557	0.0557
0.9	0.00858	0.00686	0.0686
1	0.0101	0.00828	0.0828
1.1	0.0118	0.00984	0.0984
1.2	0.0136	0.0115	0.115
1.3	0.0156	0.0133	0.133
1.4	0.0177	0.0153	0.153
1.5	0.0199	0.0174	0.174
1.6	0.0222	0.0196	0.196
1.7	0.0247	0.022	0.22
1.8	0.0273	0.0245	0.245
1.9	0.03	0.0271	0.271
2	0.0329	0.0298	0.298
3	0.0686	0.0646	0.646
4	0.117	0.113	1.13
5	0.179	0.174	1.74
6	0.254	0.249	2.49
7	0.341	0.336	3.36
8	0.442	0.438	4.38
9	0.556	0.552	5.52
10	0.683	0.68	6.8
11	0.822	0.821	8.21
12	0.975	0.975	9.75
13	1.14	1.14	11.4

14	1.32	1.32	13.2
15	1.51	1.52	15.2
16	1.72	1.72	17.2
17	1.93	1.94	19.4
18	2.16	2.18	21.8
19	2.41	2.43	24.3
20	2.66	2.69	26.9
22	3.22	3.25	32.5
24	3.82	3.86	38.6
26	4.48	4.53	45.3
28	5.19	5.25	52.5
30	5.95	6.02	60.2

APPENDIX B. THEORETICAL RESULTS OF THE PARTICLE MOTION IN THE TRANSFER TUBE

The ratio of the number of the particles at the end of the 100-foot long transfer tube to the number of input particles (C_{OUT}/C_{IN}), due to the diffusion deposition inside the tube, at three different aerosol flow rates are calculated. Also, the critical tube length for the gravity deposition (L_{CR}) is calculated.

D_p (μm)	$\%C_{OUT}/C_{IN}$ (0.8 l/min)	$\%C_{OUT}/C_{IN}$ (1.0 l/min)	$\%C_{OUT}/C_{IN}$ (1.2 l/min)
0.01	-53.5	-37.3	-25.3
0.02	22.6	30.8	36.8
0.03	47.9	53.4	57.5
0.04	60.6	64.7	67.8
0.05	68.2	71.5	74
0.06	73.2	76.1	78.1
0.07	76.8	79.3	81.1
0.08	79.5	81.7	83.3
0.09	81.6	83.6	85
0.1	83.3	85.1	86.4
0.2	90.8	91.8	92.5
0.3	93.3	94.1	94.6
0.4	94.6	95.2	95.6
0.5	95.4	95.9	96.2
0.6	95.9	96.3	96.7
0.7	96.3	96.7	97
0.8	96.6	97	97.2
0.9	96.8	97.2	97.4
1	97	97.3	97.6
1.1	97.2	97.5	97.7

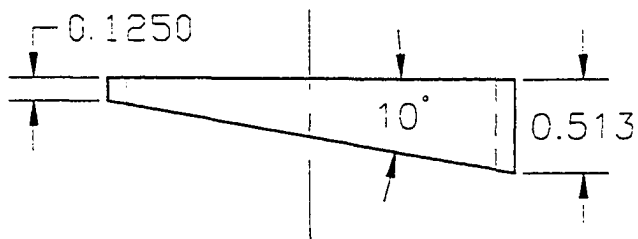
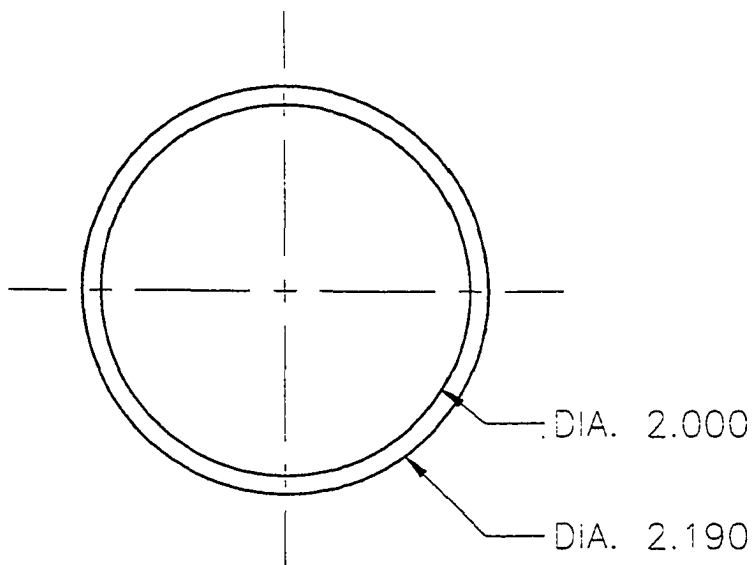
1.2	97.3	97.6	97.8
1.3	97.5	97.7	97.9
1.4	97.6	97.8	98
1.5	97.7	97.9	98.1
1.6	97.7	98	98.2
1.7	97.8	98	98.2
1.8	97.9	98.1	98.3
1.9	97.9	98.2	98.3
2	98	98.2	98.4
3	98.4	98.6	98.7
4	98.6	98.8	98.9
5	98.8	98.9	99
6	98.9	99	99.1
7	99	99.1	99.2
8	99	99.1	99.2
9	99.1	99.2	99.3
10	99.1	99.2	99.3
11	99.2	99.3	99.3
12	99.2	99.3	99.4
13	99.3	99.3	99.4
14	99.3	99.4	99.4
15	99.3	99.4	99.4
16	99.3	99.4	99.5
17	99.4	99.4	99.5
18	99.4	99.4	99.5
19	99.4	99.5	99.5
20	99.4	99.5	99.5
22	99.4	99.5	99.5
24	99.5	99.5	99.6
26	99.5	99.5	99.6
28	99.5	99.5	99.6
30	99.5	99.5	99.6

Gravity Deposit Inside the Tube

D_p (μm)	L_{CR} (ft) (0.8 l/min)	L_{CR} (ft) (1.0 l/min)	L_{CR} (ft) (1.2 l/min)
0.01	2170	2710	3230
0.02	2090	2620	3120
0.03	2020	2530	3010
0.04	1940	2440	2900
0.05	1870	2350	2800
0.06	1800	2260	2690
0.07	1740	2180	2590
0.08	1670	2100	2500
0.09	1610	2020	2400
0.1	1550	1940	2320
0.2	1070	1340	1590
0.3	757	949	1130
0.4	557	698	832
0.5	423	531	632
0.6	332	416	495
0.7	266	334	398
0.8	218	274	326
0.9	182	228	272
1	154	193	230
1.1	132	166	197
1.2	115	144	171
1.3	100	126	150
1.4	88.4	111	132
1.5	78.6	98.5	117
1.6	70.3	88.2	105
1.7	63.3	79.3	94.5
1.8	57.3	71.8	85.5
1.9	52.1	65.3	77.7
2	47.5	59.6	71
3	22.8	28.5	34
4	13.3	16.7	19.9
5	8.72	10.9	13
6	6.15	7.71	9.19
7	4.57	5.73	6.83
8	3.53	4.43	5.27
9	2.81	3.52	4.2
10	2.29	2.87	3.42
11	1.9	2.38	2.84
12	1.6	2.01	2.39

13	1.37	1.72	2.04
14	1.18	1.48	1.77
15	1.03	1.3	1.54
16	0.91	1.14	1.36
17	0.808	1.01	1.21
18	0.722	0.904	1.08
19	0.649	0.813	0.969
20	0.586	0.735	0.875
22	0.485	0.608	0.725
24	0.409	0.512	0.61
26	0.349	0.437	0.521
28	0.301	0.377	0.45
30	0.26	0.329	0.392

**APPENDIX C. DRAWINGS FOR SURFACE AND SUB-SURFACE
ABLATION CELLS**



TOLERANCES:
 (UNLESS OTHERWISE SPECIFIED)
 MACHINE TOL. = ± 0.005
 ANGULAR = ± 1°

TECHNOLOGY INTEGRATION
 PROGRAM
TIP
 AMES LABORATORY
 DEPARTMENT OF ENERGY (DOE)

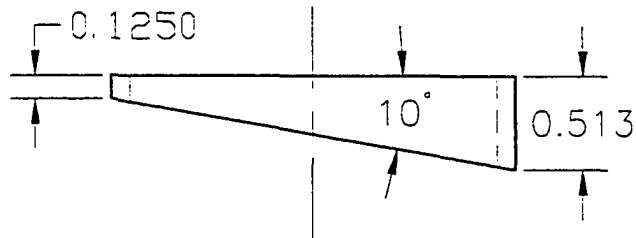
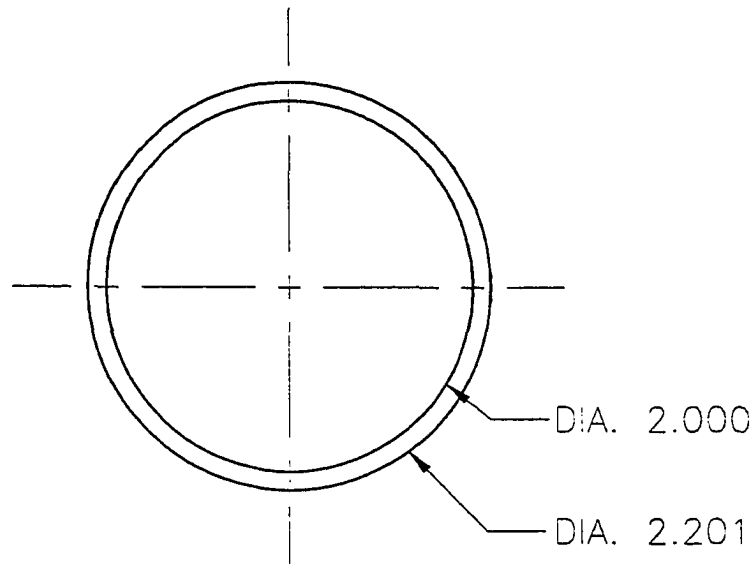
SURFACE ABLATION CELL
 QUARTZ WINDOW SUPPORT

MATERIAL:
 BRASS

DRAWING:
 ABC01A

DRAWN BY:
 REZA BASHIRZADEH

SCALE:
 NONE



TOLERANCES:
 (UNLESS OTHERWISE SPECIFIED)
 MACHINE TOL. = ± 0.005
 ANGULAR = ± 1°

TECHNOLOGY INTEGRATION PROGRAM
 AMES LABORATORY
 DEPARTMENT OF ENERGY (DOE)

TIP

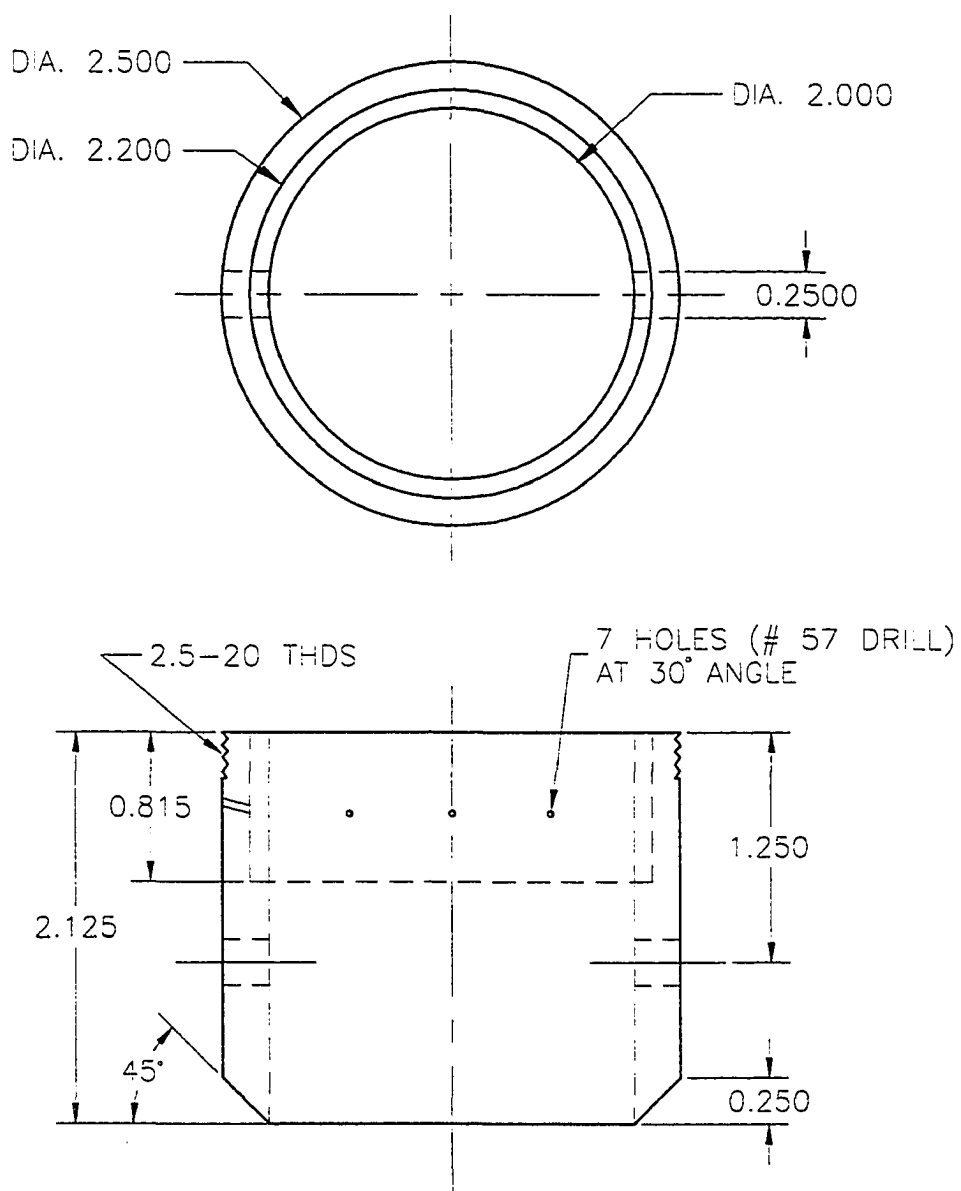
SURFACE ABLATION CELL
 QUARTZ WINDOW SUPPORT

MATERIAL: BRASS

DRAWING: ABC01B

DRAWN BY: REZA BASHIRZADEH

SCALE: NONE



TOLERANCES.
(UNLESS OTHERWISE SPECIFIED)
MACHINE TOL. = ± 0.005
ANGULAR = ± "

TECHNOLOGY INTEGRATION
PROGRAM
AMES LABORATORY
DEPARTMENT OF ENERGY (DOE)

TIP

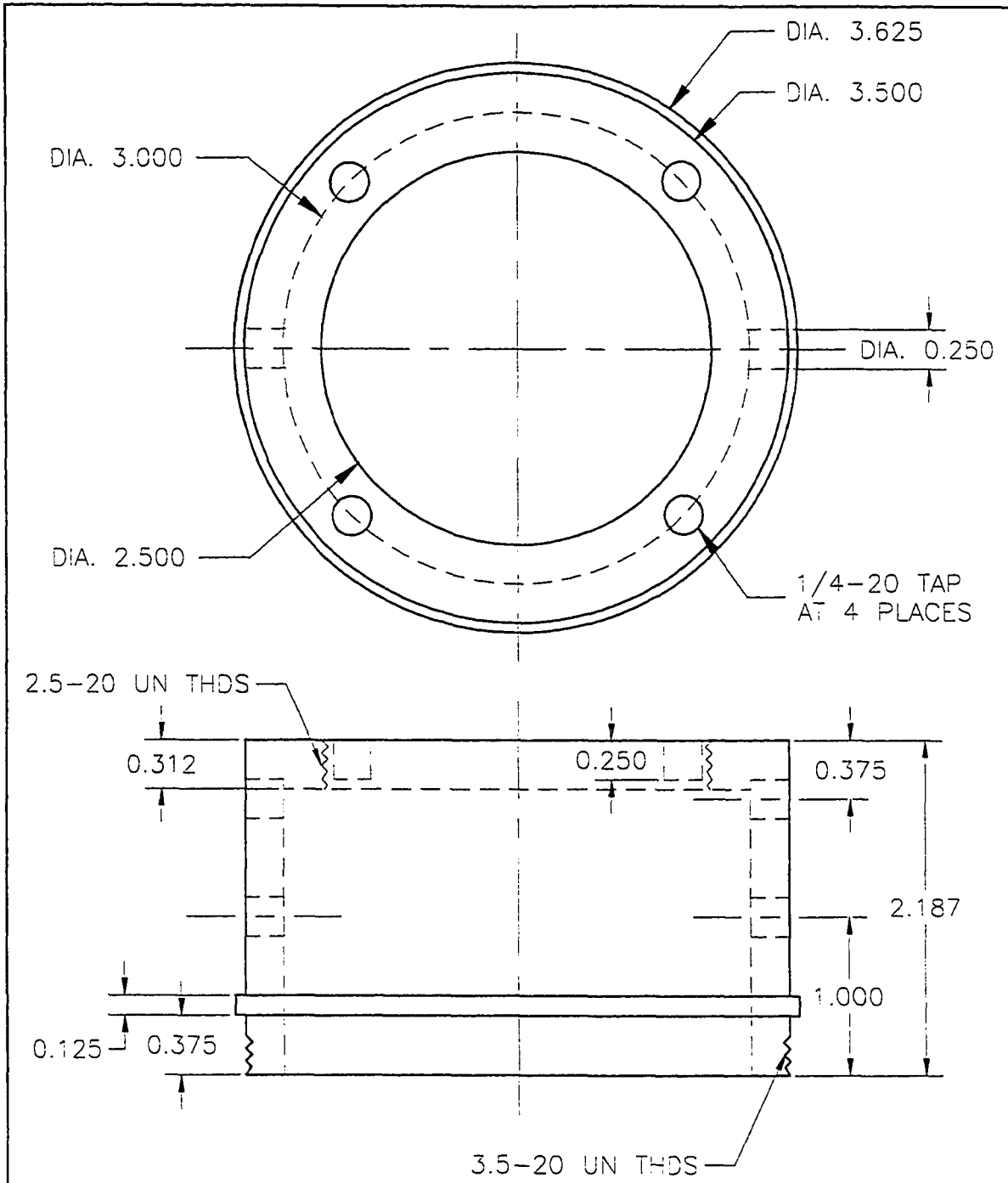
SURFACE ABLATION CELL
INNER WALL

MATERIAL:
BRASS

DRAWING:
ABC02

DRAWN BY:
REZA BASHIRZADEH

SCALE:
NONE



TOLERANCES:
 (UNLESS OTHERWISE SPECIFIED)
 MACHINE TOL. = ± 0.005
 ANGULAR = ± 1°

TECHNOLOGY INTEGRATION PROGRAM
TIP
 AMES LABORATORY
 DEPARTMENT OF ENERGY (DOE)

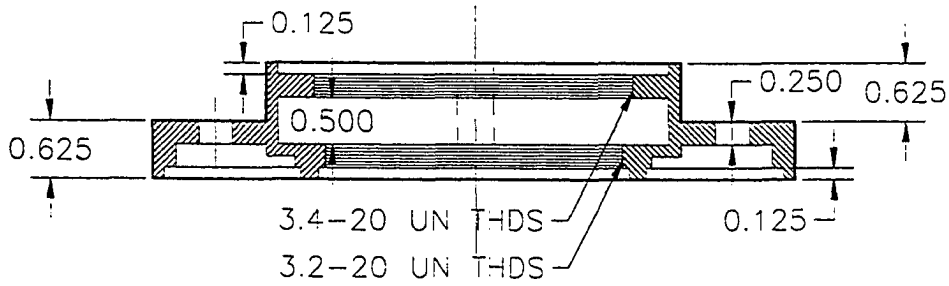
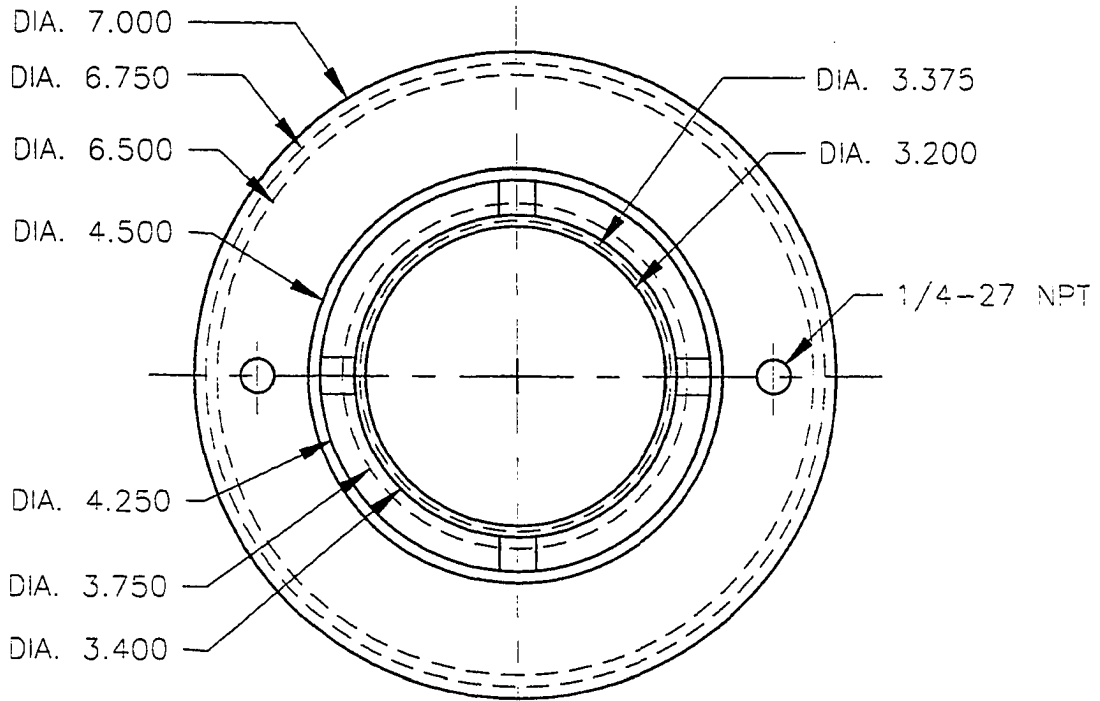
SURFACE ABLATION CELL
 OUTSIDE WALL

MATERIAL: S.S. 304

DRAWING: ABC03

DRAWN BY: REZA BASHIRZADEH

SCALE: NONE



TOLERANCES:
 (UNLESS OTHERWISE SPECIFIED)
 MACHINE TOL. = ± 0.005
 ANGULAR = ± 1°

TECHNOLOGY INTEGRATION
 PROGRAM
 AMES LABORATORY
 DEPARTMENT OF ENERGY (DOE)

TIP

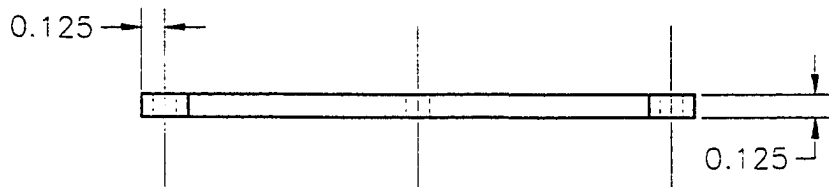
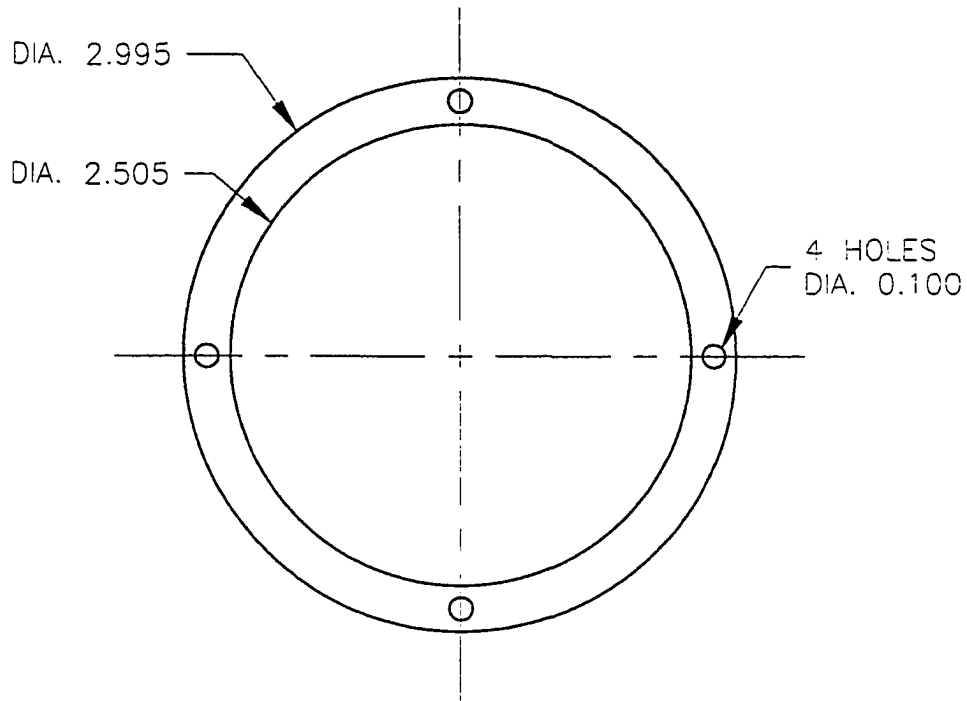
SURFACE ABLATION CELL
 KNIFE EDGE SUPPORT

MATERIAL:
 BRASS

DRAWING:
 ABC04

DRAWN BY:
 REZA BASHIRZADEH

SCALE:
 NONE



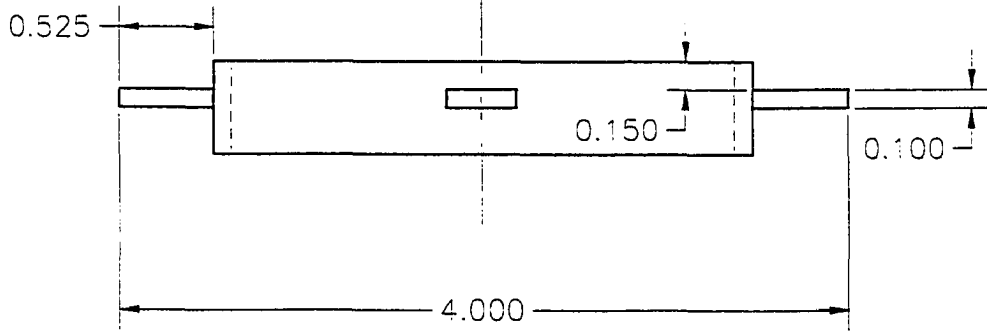
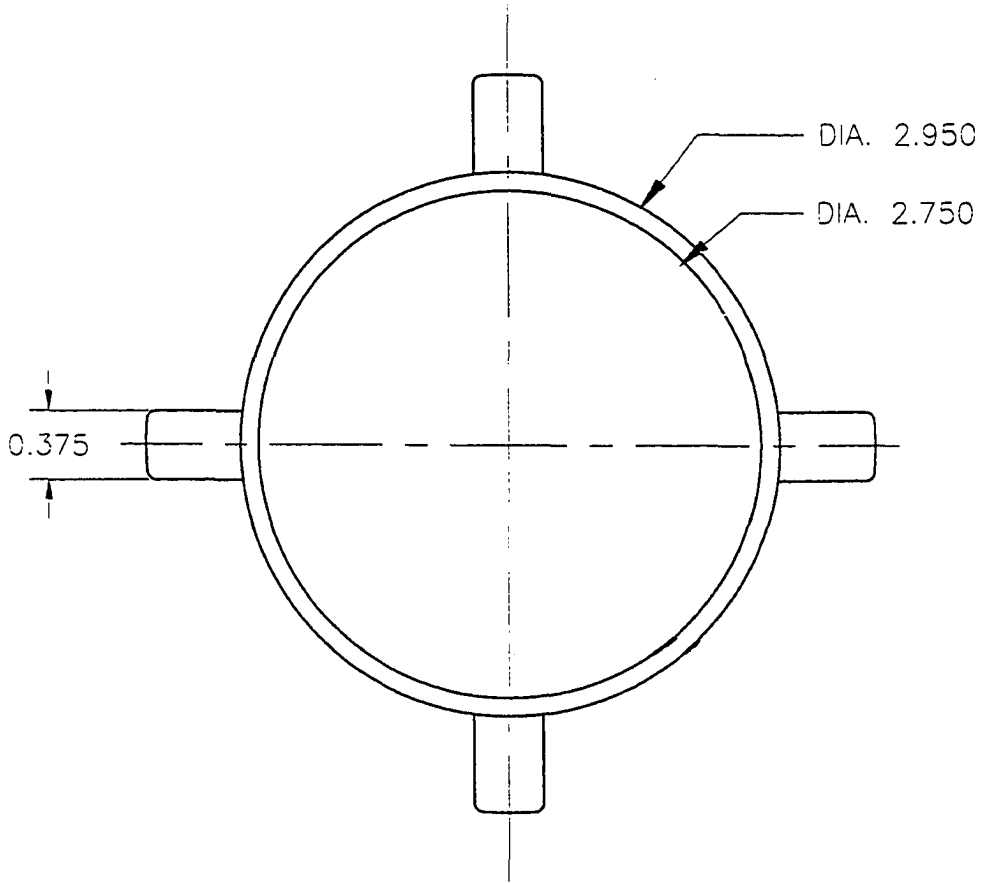
TOLERANCES:
(UNLESS OTHERWISE SPECIFIED)
MACHINE TOL. = ± 0.005
ANGULAR = ± 1°

TECHNOLOGY INTEGRATION PROGRAM
TIP
AMES LABORATORY
DEPARTMENT OF ENERGY (DOE)

SURFACE ABLATION CELL
SPACER

MATERIAL: BRASS
DRAWN BY: REZA BASHIRZADEH

DRAWING: ABC05
SCALE: NONE



TOLERANCES:
(UNLESS OTHERWISE SPECIFIED)
MACHINE TOL. = ± 0.005
ANGULAR = ± 1°

TECHNOLOGY INTEGRATION PROGRAM
TIP
AMES LABORATORY
DEPARTMENT OF ENERGY (DOE)

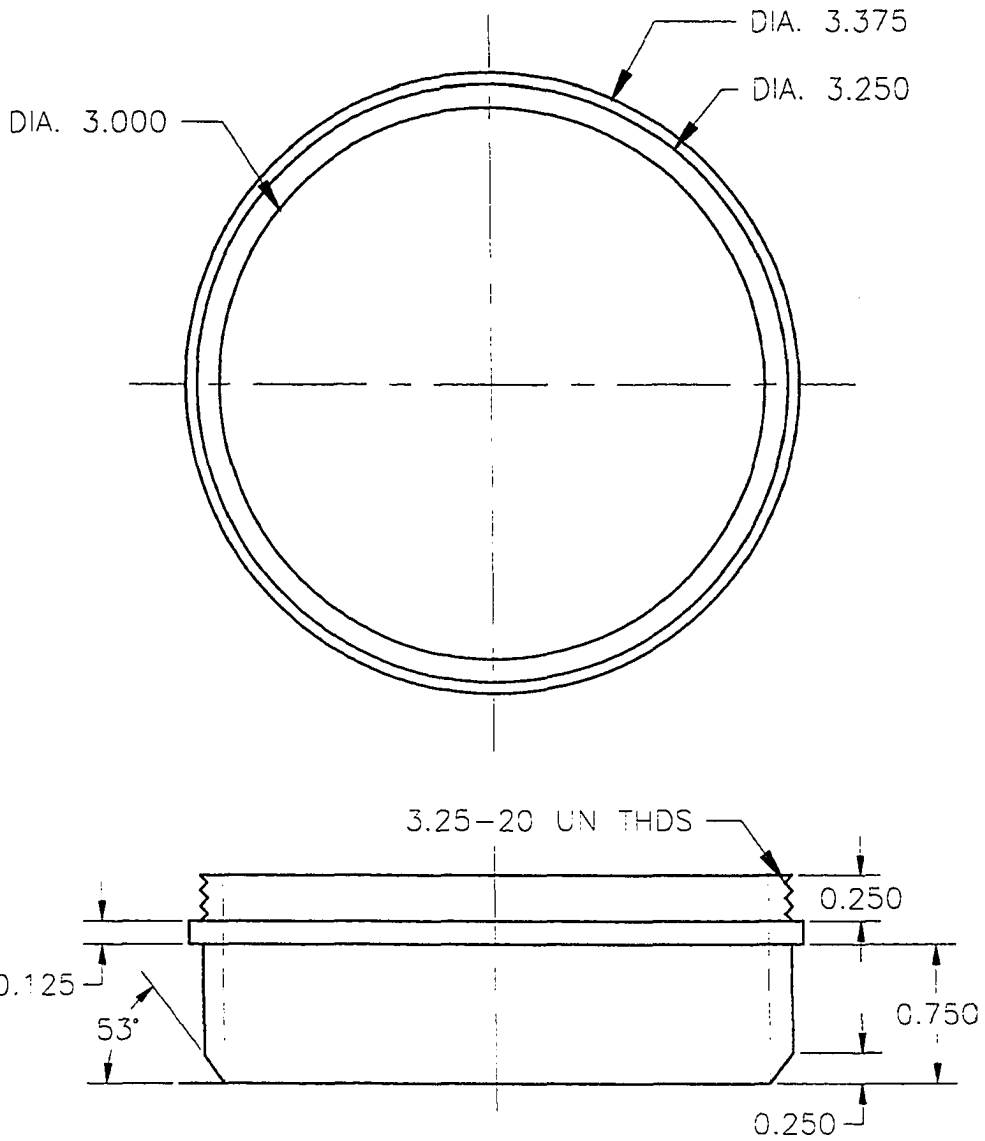
SURFACE ABLATION CELL
SEALING RING HOLDER

MATERIAL: BRASS

DRAWING: ABC06

DRAWN BY: REZA BASHIRZADEH

SCALE: NONE



TOLERANCES:
 (UNLESS OTHERWISE SPECIFIED)
 MACHINE TOOL = ± 0.005
 ANGULAR = ± 1°

TECHNOLOGY INTEGRATION PROGRAM
TIP
 AMES LABORATORY
 DEPARTMENT OF ENERGY (DOE)

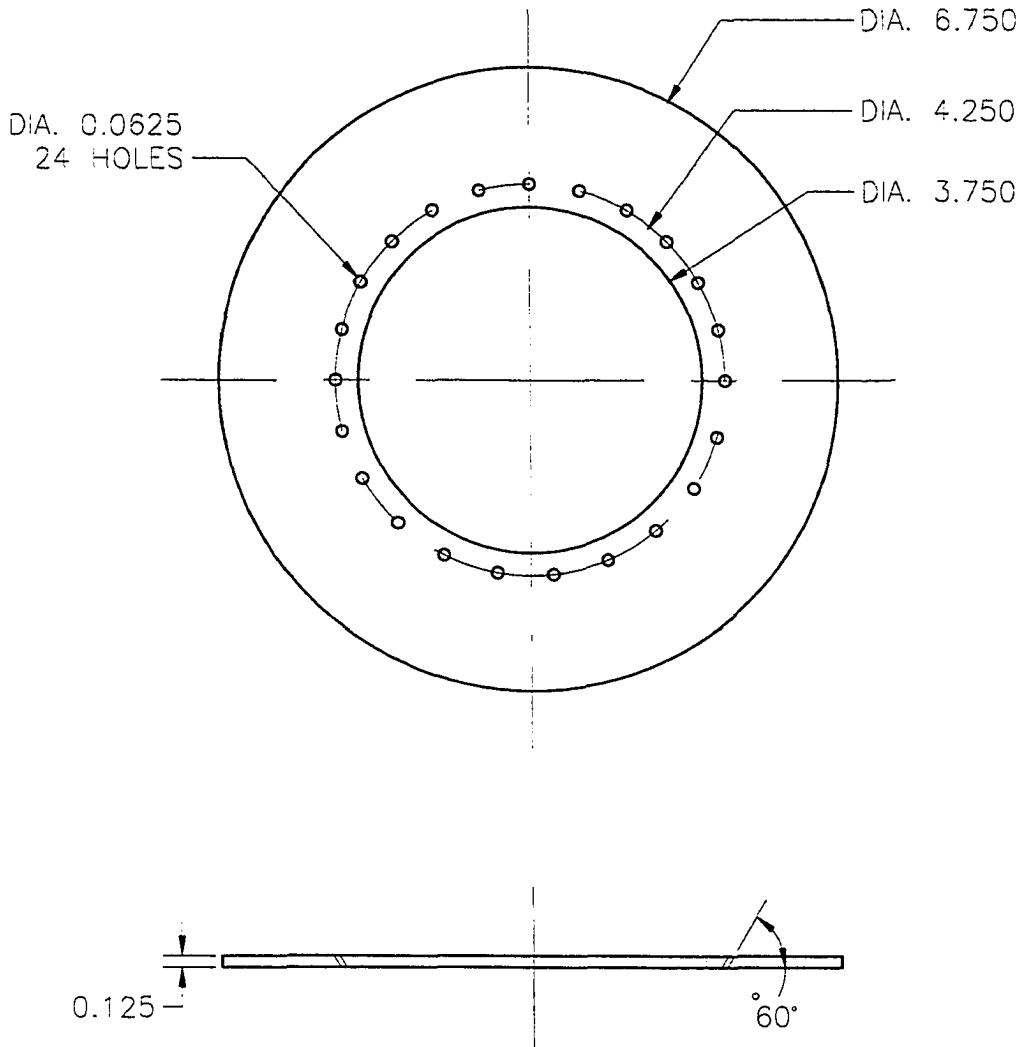
SURFACE ABLATION CELL
 KNIFE EDGE

MATERIAL: S.S. 304

DRAWING: ABC07

DRAWN BY: REZA BASHIRZADEH

SCALE: NONE



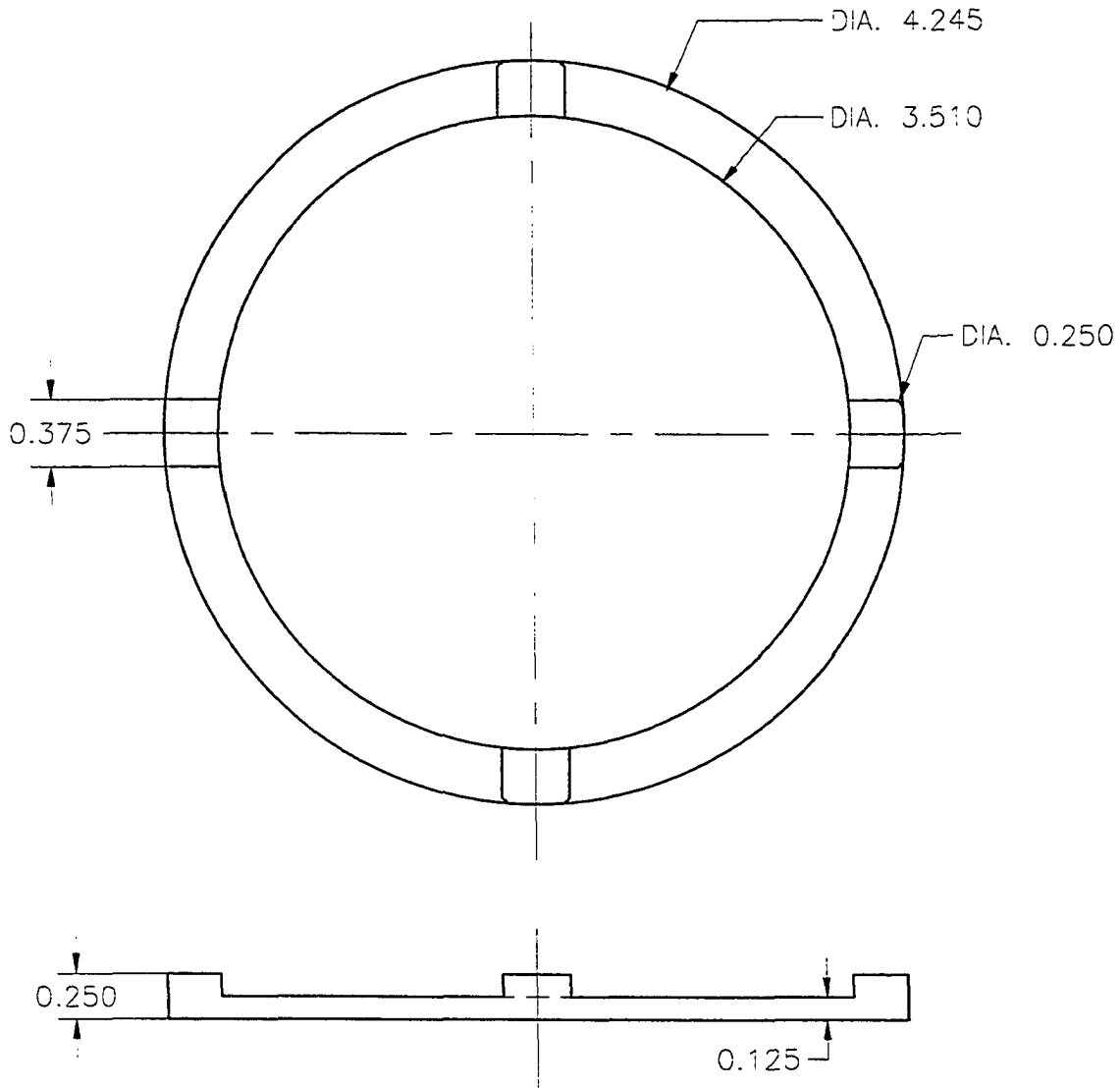
TOLERANCES:
 (UNLESS OTHERWISE SPECIFIED)
 MACHINE TO... = ± 0.005
 ANGULAR = ± 1°

TECHNOLOGY INTEGRATION PROGRAM
TIP
 AMES LABORATORY
 DEPARTMENT OF ENERGY (DOE)

SURFACE ABLATION CELL
 SPRAY RING

MATERIAL: BRASS
 DRAWN BY: REZA BASHIRZADEH

DRAWING: ABC08
 SCALE: NONE

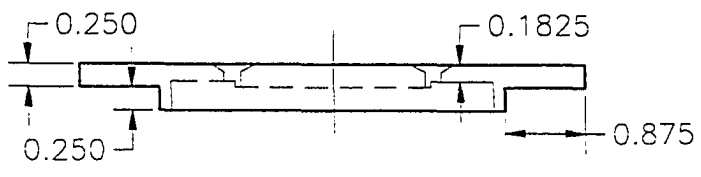
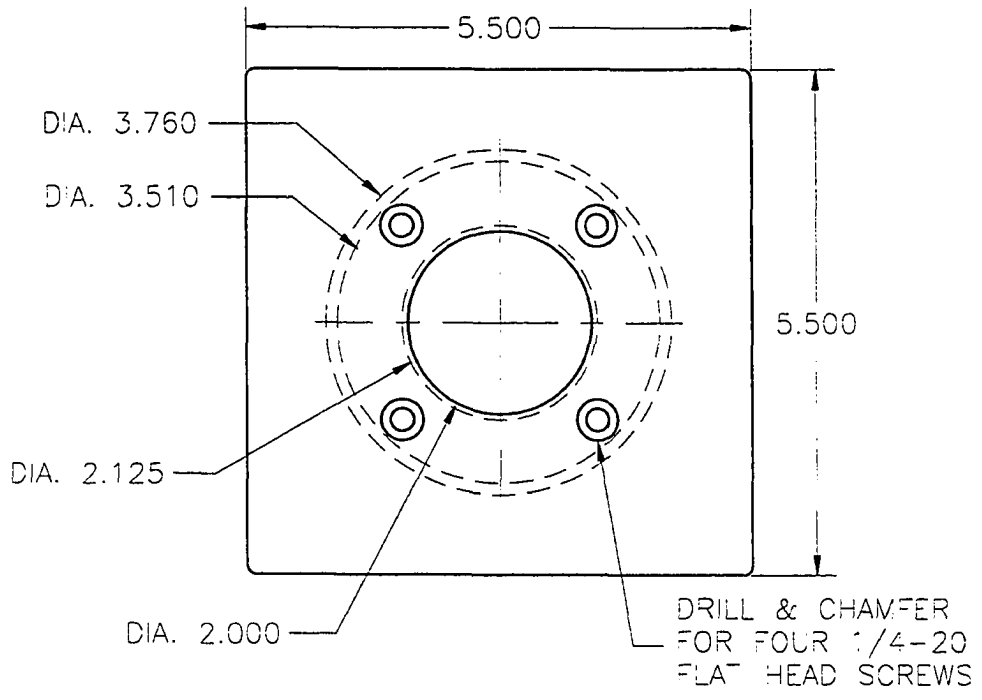


TOLERANCES:
 (UNLESS OTHERWISE SPECIFIED)
 MACHINE TO. ± 0.005
 ANGULAR ± 1°

TECHNOLOGY INTEGRATION PROGRAM
TIP
 AMES LABORATORY
 DEPARTMENT OF ENERGY (DOE)

SURFACE ABLATION CELL
 SPRING HOLDER

MATERIAL: BRASS	DRAWING: ABC09
DRAWN BY: REZA BASHIRZADEH	SCALE: NONE



TOLERANCES:
 (UNLESS OTHERWISE SPECIFIED)
 MACHINE TOL. = ± 0.005
 ANGULAR = ± 1°

TECHNOLOGY INTEGRATION PROGRAM
TIP
 AMES LABORATORY
 DEPARTMENT OF ENERGY (DOE)

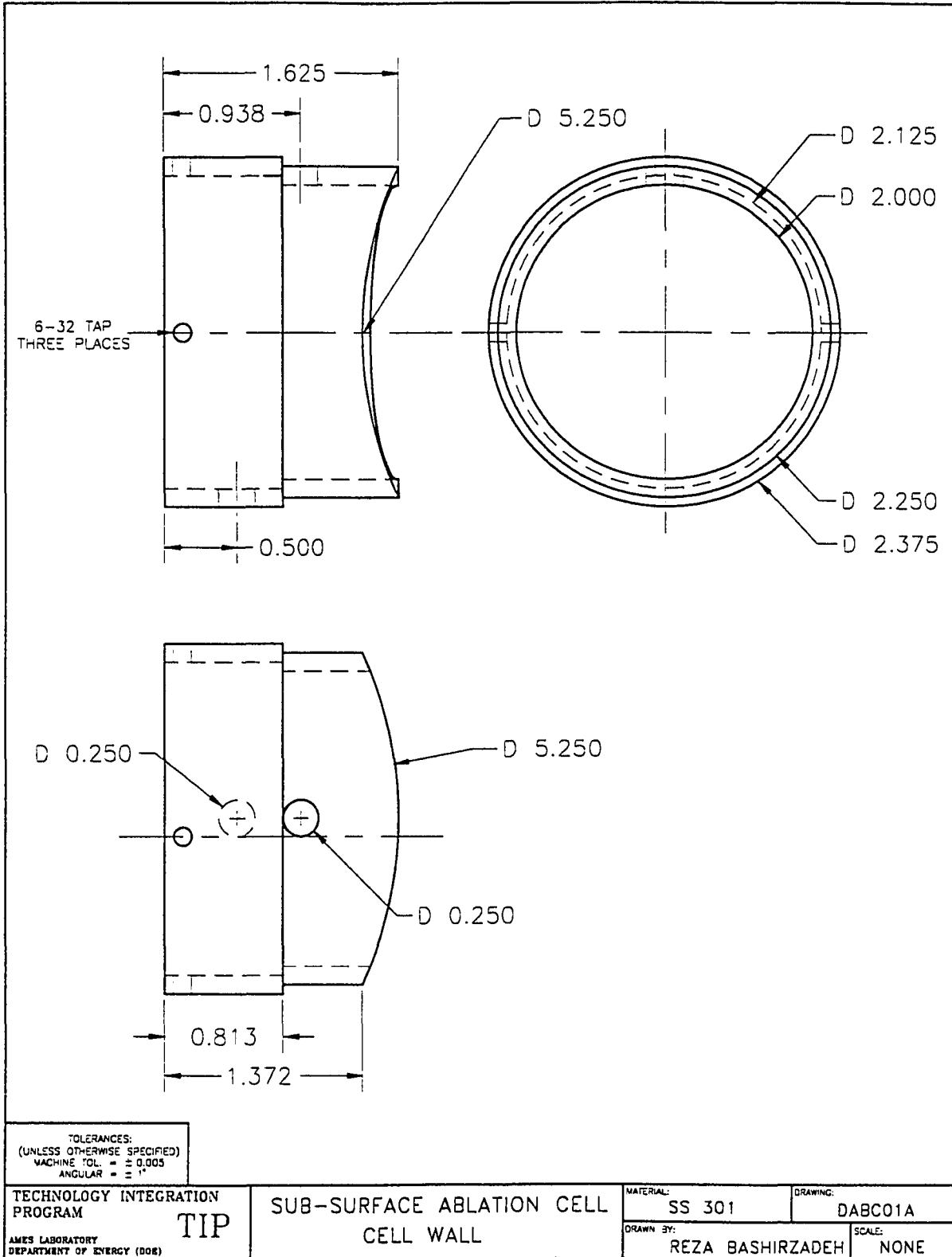
SURFACE ABLATION CELL
 CELL HOLDER

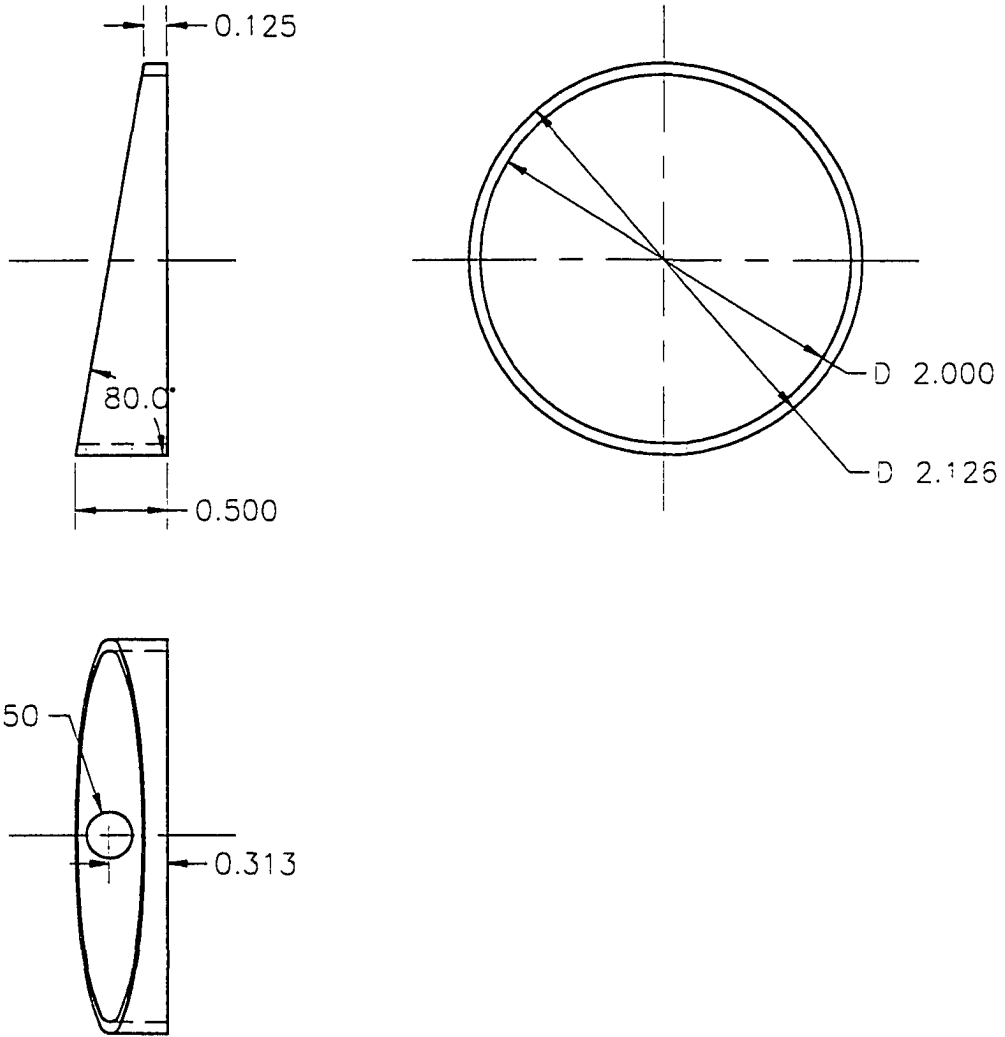
MATERIAL: S.S. 304

DRAWING: ABC10

DRAWN BY: REZA BASHIRZADEH

SCALE: NONE





TOLERANCES:
 (UNLESS OTHERWISE SPECIFIED)
 MACHINE TOL. = ± 0.005
 ANGULAR = ± 1°

TECHNOLOGY INTEGRATION
 PROGRAM
TIP
 AMES LABORATORY
 DEPARTMENT OF ENERGY (DOE)

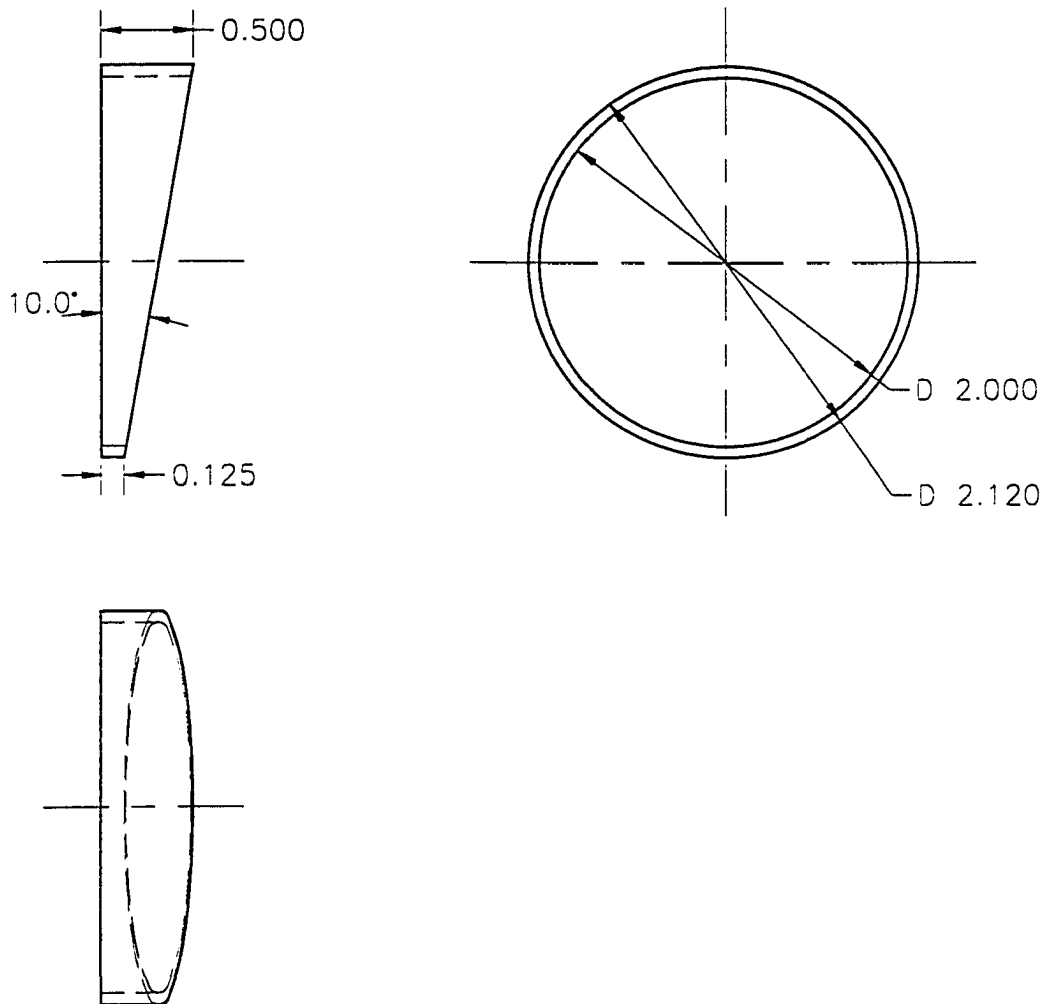
SUB-SURFACE ABLATION CELL
 WINDOW SUPPORT (FRONT)

MATERIAL: SS 301

DRAWING: DABC02

DRAWN BY: REZA BASHIRZADEH

SCALE: NONE



TOLERANCES:
 (UNLESS OTHERWISE SPECIFIED)
 MACHINE TOL. = ± 0.005
 ANGULAR = ± .1°

TECHNOLOGY INTEGRATION
 PROGRAM

TIP

SUB-SURFACE ABLATION CELL
 WINDOW SUPPORT (BACK)

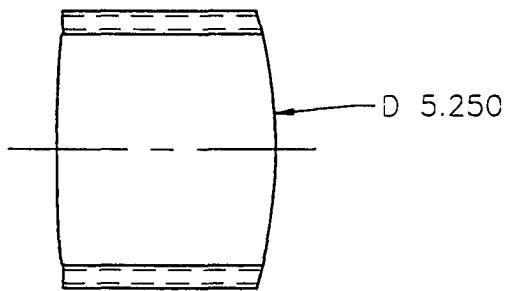
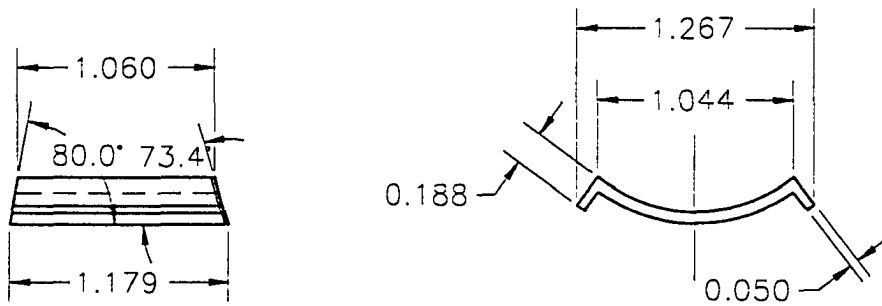
MATERIAL:
 SS 301

DRAWING:
 DABC03

AMES LABORATORY
 DEPARTMENT OF ENERGY (DOE)

DRAWN BY:
 REZA BASHIRZADEH

SCALE:
 NONE



TOLERANCES:
 (UNLESS OTHERWISE SPECIFIED)
 MACHINE TOL = ± 0.005
 ANGULAR = ± 1°

TECHNOLOGY INTEGRATION PROGRAM

TIP

SUB-SURFACE ABLATION CELL
 FLOW DEFLECTOR CHANNEL

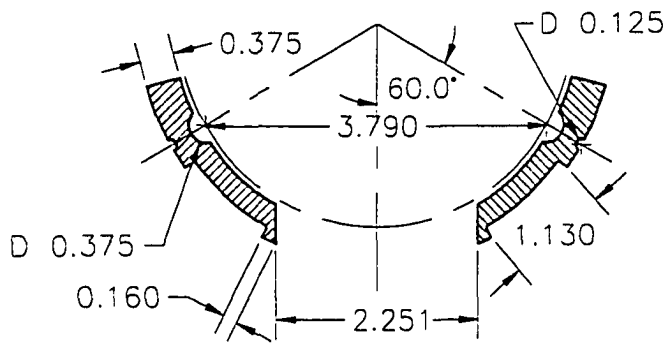
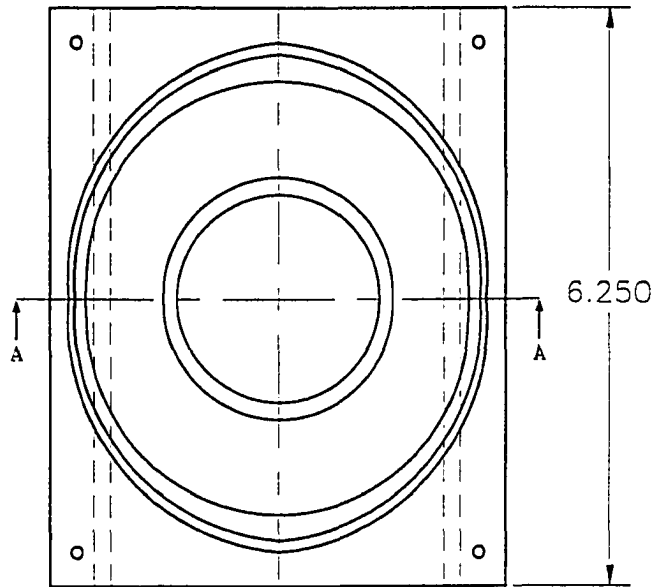
MATERIAL: SS 301

DRAWING: DABC04

DRAWN BY: REZA BASHIRZADEH

SCALE: NONE

AMES LABORATORY
 DEPARTMENT OF ENERGY (DOE)



SECTION AA

TOLERANCES:
(UNLESS OTHERWISE SPECIFIED)
MACHINE TOL. = ± 0.005
ANGULAR = ± 1°

TECHNOLOGY INTEGRATION PROGRAM

AMES LABORATORY
DEPARTMENT OF ENERGY (DOE)

TIP

SUB-SURFACE ABLATION CELL
CELL SUPPORTING PLATE

MATERIAL: BRASS 306

DRAWING: DABC05

DRAWN BY: REZA BASHIRZADEH

SCALE: NONE

